Nanoscale 3D structures towards improved cell-chip coupling on microelectrode arrays

Sabrina Deniese Weidlich

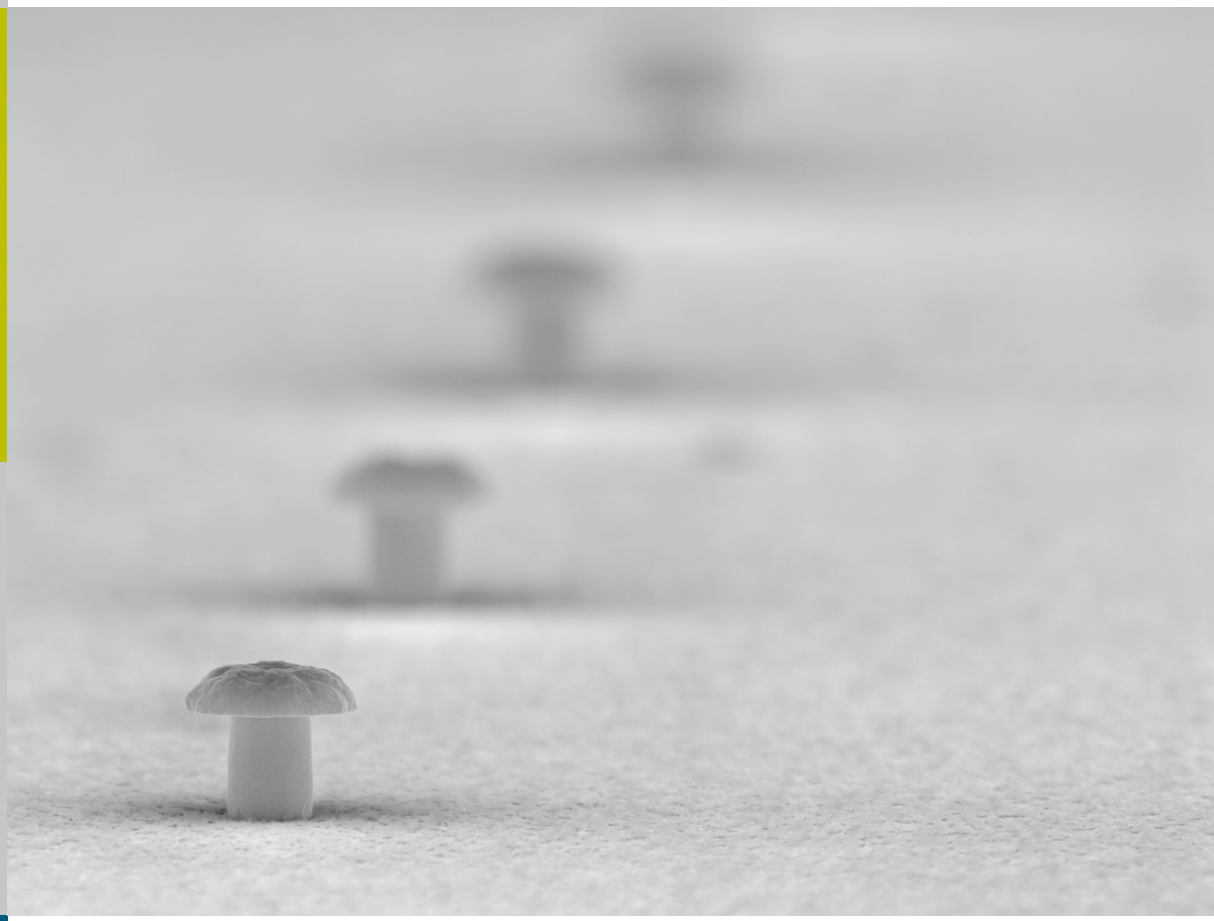

Member of the Helmholtz Association

Schlüsseltechnologien / Key Technologies
Band / Volume 156
ISBN 978-3-95806-278-8

JÜLICH
FORSCHUNGSZENTRUM

Schriften des Forschungszentrums Jülich
Reihe Schlüsseltechnologien / Key Technologies Band / Volume 156

Forschungszentrum Jülich GmbH
Institute of Complex Systems
Bioelectronics (ICS-8)

Nanoscale 3D structures towards improved cell-chip coupling on microelectrode arrays

Sabrina Deniese Weidlich

Schriften des Forschungszentrums Jülich
Reihe Schlüsseltechnologien / Key Technologies Band / Volume 156

ISSN 1866-1807 ISBN 978-3-95806-278-8

Bibliographic information published by the Deutsche Nationalbibliothek.
The Deutsche Nationalbibliothek lists this publication in the Deutsche
Nationalbibliografie; detailed bibliographic data are available in the
Internet at http://dnb.d-nb.de.

Publisher and Distributor:	Forschungszentrum Jülich GmbH Zentralbibliothek 52425 Jülich Tel: +49 2461 61-5368 Fax: +49 2461 61-6103 Email: zb-publikation@fz-juelich.de www.fz-juelich.de/zb
Cover Design:	Grafische Medien, Forschungszentrum Jülich GmbH
Printer:	Grafische Medien, Forschungszentrum Jülich GmbH
Copyright:	Forschungszentrum Jülich 2017

Schriften des Forschungszentrums Jülich
Reihe Schlüsseltechnologien / Key Technologies, Band / Volume 156

D 82 (Diss. RWTH Aachen University, 2017)

ISSN 1866-1807
ISBN 978-3-95806-278-8

The complete volume is freely available on the Internet on the Jülicher Open Access Server (JuSER)
at www.fz-juelich.de/zb/openaccess.

Listen to the **MUSTN'TS**, child,
Listen to the **DON'TS**
Listen to the **SHOULDN'TS**
The **IMPOSSIBLES**, the **WONT'S**
Listen to the **NEVER HAVES**
Then listen close to me
Anything can happen, child,
ANYTHING can be

Shel Silverstein, American poet
1930-1999

Abstract

The human brain is a highly interconnected system, consisting of about 86 billion neurons,[1] each forming on average 7,000 connections to neighboring cells.[2] While neuroscientists have achieved various breakthroughs elucidating the underlying principles of neuronal communication in the past decades, the goal of an in-depth understanding of the complex events involved in network communication and processes such as learning remains unattained. One approach often employed to reduce the complexity and thereby facilitate high-resolution studies of the cellular interaction is the application of microelectrode arrays (MEAs). They enable the *in vitro* investigation of small neuronal networks, yielding correlated data of the cellular activity with high temporal resolution. However, MEAs suffer from inherently low signal amplitudes due to a loose cell-chip contact and thus insufficient coupling between the cellular signals and the electrode. In the past decade, three-dimensional electrode designs have been extensively studied as possible solution for the problem of low signal amplitudes during MEA-based investigations of electrogenic cells. They improve the cell-chip coupling through the establishment of a tighter interface between biology and electronics. However, while many different 3D designs have been suggested in the literature, the requirements for a direct comparison of the recording capabilities yielded by the different structures have so far not been met.

The aim of this body of work therefore is the development of an approach allowing for the parallel fabrication of multiple different 3D designs on a single chip and thus parallel testing on the biological system. In the first part of this thesis, electron-beam lithography is employed in conjunction with electrodeposition for a parallelized preparation of thousands of 3D structures on gold-on-silicon substrates. In this manner, the common 3D geometries as reported in the literature - pillars, hollow pillars, and mushroom-shaped structures - are produced. Furthermore, hollow mushrooms are developed as novel 3D design. The interaction of the structures with both cardiomyocyte-like HL-1 cells as well as rat cortical neurons is investigated. In the second part of this thesis, the developed 3D structures are transferred onto MEAs. A thorough investigation of the galvanization procedure yields parameters that enable the real-time control of the nanoscale structure size during the electrodeposition process. In this way, 3D electrodes of different shape and size can be prepared on a single MEA and thus be investigated simultaneously with respect to their interaction with electrogenic cells. Electrophysiological studies are performed employing cardiomyocyte-like HL-1 cells as model system. Furthermore, various modifications of the 3D structures are discussed, aiming at improved electrical characteristics for future investigations. In conclusion, this body of work presents a well-controlled process for the preparation of 3D structures on MEAs, thereby facilitating the preparation of multiple different three-dimensional designs on a single chip. This forms the basis for an in-depth characterization of the improvement of the cell-chip coupling yielded by the different 3D designs.

Zusammenfassung

Das menschliche Gehirn besteht aus ca. 86 Milliarden Nervenzellen,[1] welche jeweils rund 7.000 Verbindungen zu benachbarten Neuronen bilden.[2] Während die Neurowissenschaften in den letzten Jahrzehnten bedeutende Fortschritte im Bereich der Grundlagen neuronaler Kommunikation erzielt haben, bleibt das detaillierte Verständnis der Aktivität und Interaktion dieses komplexen Systems ein unerreichtes Ziel. Ein häufig verwendeter Ansatz zur Reduktion der Komplexität und somit der Untersuchung grundsätzlicher Mechanismen, ist die Verwendung von Mikroelektrodenarrays (MEAs), welche es ermöglichen, kleinere neuronale Netzwerke *in vitro* zu untersuchen und korrelierte Daten bezüglich der zellulären Aktivität zu erhalten. Ein inhärentes Problem dieses Ansatzes ist jedoch die geringe Effizienz der Signaltransduktion aufgrund des schlechten Kontaktes zwischen Zelle und Elektrode und der daraus folgenden schlechten Zell-Chip Kopplung. Als mögliche Lösung dieses Problems wurden dreidimensionale Elektrodenstrukturen im letzten Jahrzehnt intensiv erforscht, da sie aufgrund eines engen Kontaktes zur Zelle das biologische Signal besser erfassen. Während die Zahl der wissenschaftlichen Studien in diesem Bereich stetig wächst, fehlt jedoch bislang eine Methodik, welche die Voraussetzungen für einen direkten Vergleich der verschiedenen Strukturen schafft.

Ziel dieser Dissertation ist somit die Entwicklung eines Fabrikationsweges, der eine gut kontrollierbare Herstellung verschiedenster 3D Strukturen auf MEAs ermöglicht. Dazu werden mittels Elektrodeposition zunächst tausende Strukturen in einem parallelisierten Ansatz hergestellt und somit die nötigen Parameter für die Fabrikation ermittelt. Neben den in der Literatur bekannten pilz-, zylinder- und hohlzylinder-förmigen 3D Designs werden hohle Pilze als neuartige 3D Elektrode entwickelt. Ferner wird die Interaktion einer kardiomyozytenartigen Zelllinie sowie kortikaler Neuronen mit den entwickelten Strukturen untersucht. Im Folgenden werden die Strukturen auf MEAs übertragen. Eine genaue Charakterisierung der Strukturherstellung ermöglicht die Etablierung eines gut kontrollierbaren Prozesses, durch den die Größe der Nanostrukturen während der Fabrikation in Echtzeit angepasst werden kann. Auf diese Weise ist es möglich, Strukturen verschiedenster Form und Größe auf einem einzelnen MEA darzustellen und somit simultan am biologischen System zu untersuchen. Anschließend wird die Verbesserung der Signaltransduktion zwischen Elektronik und elektrisch erregbaren Herzmuskelzellen aufgrund der entwickelten 3D Strukturen erforscht. Abschließend werden diverse Modifikationen thematisiert, welche zur Verbesserung der elektrischen Eigenschaften der 3D Strukturen herangezogen werden können. Zusammenfassend ermöglicht die hier entwickelte, gut kontrollierbare Darstellung verschiedenster 3D Strukturen auf einem einzelnen MEA eine parallelisierte Untersuchung der Strukturen. Damit legt diese Arbeit den Grundstein für eine bessere Untersuchung des Einflusses dreidimensionaler Elektrodenstrukturen auf die Signaltransduktion von Mikroelektrodenarrays.

Contents

Chapter 1

Introduction

The human brain is a vastly complex system, consisting of approximately 86 billion neurons,[1] each forming on average 7,000 connections to neighboring cells.[2] Despite intense efforts, scientists are still far from understanding how this vast network accomplishes functional interaction to perform the complex processes that constitute the human condition. Due to the intricacy at hand, *in vivo* studies are mostly limited to coarse-grained, macroscale methods that enable the investigation of brain area function and localization of functional failures such as electroencephalography (EEG), magnetic resonance imaging (MRI), and positron emission tomography (PET). However, even if the resolution of these methods would permit the investigation of single-cell activity, the contemporary computational power would be profoundly inadequate for the correlation and analysis of the resulting data. Considerable efforts towards closing this gap are made in large, (multi)national initiatives like the Human Brain Project or the BRAIN Initiative, though, aiming to make better approaches available within the next decade. Nevertheless, for the investigation of the underlying principles of brain function, *in vitro* investigations of small neuronal networks, the establishment of connectivity within these networks, and their communication and plasticity currently provide a more feasible approach. Since the mode of communication between neurons is twofold - via chemical cues from one cell to another and via electrical impulses traveling along the membrane within each single cell - the neuronal signaling can be detected through external electronics by recording the changes in membrane potential. While probe-based approaches such as patch-clamp recordings[3] are the gold standard for the investigation of ion channels and the activity of single neurons, the need for multiple interaction sites that can produce correlated signals with high spatiotemporal resolution necessitates a different approach for the investigation of neuronal

networks. Here, the field of neuroelectronics is concerned with the development of adequate transducers that enable the recording of high amplitude, high signal-to-noise (S/N) ratio data. Two different substrate-integrated approaches have received considerable attention in the past decades: Microelectrode arrays (MEAs) and field-effect transistors (FETs). MEAs were first introduced by Thomas *et al.*[4] in 1972 and have been the focus of numerous studies since. They are *passive*, bidirectional transducers that facilitate both, the recording of activity from neurons and other electrically active (electrogenic) cells, as well as the stimulation of electrogenic activity. MEAs provide multiple interaction sites, thereby enabling the investigation of network activity, and are non-invasive,[5] thus paving the way for long-term studies such as are needed for the study of processes like learning. Furthermore, they exhibit excellent temporal resolution and can easily be produced to cover large areas. In contrast, FETs are *active* devices that can result in a large device-based amplification of the cellular signal. Since FETs are not impedance limited,[5] it is possible to fabricate very small probes of sizes below 100 nm.[6] However, the challenging fabrication of FETs and limited stimulation capability present some disadvantages as compared to passive solid-state electrodes. Many reports on the application of FETs for neuroelectronic questions are reported in the literature[7,8] but are beyond the scope of this introduction.

In the past decades, MEAs have been employed to study a variety of cell types such as chick embryonic myocytes,[4,9,10] dissociated invertebrate neurons,[11,12] and mammalian neurons.[13,14] However, despite continued research, two limiting factors for the efficiency of MEA-based systems remain: The *spatial resolution* and the *coupling efficiency*. The spatial resolution of MEAs is limited by the size, arrangement, and number of electrodes on the device. While the ideal MEA exhibits a high electrode density, this poses several problems. On the one hand, a higher density necessitates the fabrication of smaller electrodes, which results in an increase in device impedance and thus thermal noise. On the other hand, reducing the electrode pitch to achieve a higher electrode density increases the crosstalk[15] during electrical stimulation and is further limited by the capabilities of later connecting the large number of electrodes to external electronics. This problem can be circumvented through the usage of complementary metal oxide semiconductor (CMOS) based circuitry, where each electrode is equipped with its own on-chip amplifier and multiplexing enables the mapping of several electrodes onto a single read-out channel.[16,17] Nevertheless, while this enables the fabrication of high electrode densities, the problem of high electrode impedance remains.

Many approaches towards solving this problem have been reported in the literature,[18,19] ranging from attempts at increasing the surface area with rough or porous metal surfaces,[4,20–28] carbon nanotubes,[29–32] to the application of conducting polymers.[33–36] While many promising results have been reported, none of the investigated concepts have provided the necessary decrease in impedance coupled with sufficient long-term stability.

While the cell-electrode contact area and thus electrode size also influences the coupling efficiency of MEA-based recordings, the coupling is primarily limited by the tightness of the cell-electrode contact, also termed sealing. Due to their extracellular position and limited sealing, MEAs usually record distinctly attenuated cellular signals with amplitudes of only around 1%[5] of the cellular action potential. This results in the inability to detect subthreshold activity with these devices, a considerable disadvantage due to the fact that a significant amount of neuronal communication is thought to proceed via subthreshold activity.[5] While some publications focus on improving the cell-electrode contact via biochemical cues[37,38] or through the application of mechanical pressure,[39,40] significant efforts have been devoted to engineering the electrode geometry in order to facilitate optimal sealing. Promising results have been achieved through the introduction of nano-edge microelectrodes[41] and particularly via the introduction of recessed nanocavities,[42–45] which enable a significant reduction in impedance while maintaining a high spatial resolution and increased sealing. Another approach that has attracted extensive attention in the past decade are three-dimensional electrode designs, aiming to improve the cell-electrode coupling either through an enhanced contact via engulfment-like processes,[46–49] cellular protrusion into hollow structures,[50] or cellular impalement[51–53] similar to the effect of sharp electrodes. Pioneer work in the field of 3D electrodes was conducted by Spira *et al.* in 2007,[46] where they showed that both *Aplysia californica* neurons and human cardiomyocytes[46] as well as various cell lines[47] engulf mushroom-shaped gold spines. They reported the formation of a very tight cell-electrode interface, which led to the recording of unprecedented signal amplitudes both for invertebrate and vertebrate neurons in the years following their discovery, with signal amplitudes of up to 5 mV peak-to-peak (p2p) reported for embryonic rat hippocampal neurons.[54] The mechanism according to which 3D mushroom-shaped electrodes improve the cell-electrode coupling is believed to be a conjunction of different effects; The induction of a phagocytotic engulfment of the structures leads to a better contact and reduced cell-electrode gap distance, which re-

sults in an increase in the sealing resistance R_{seal}.[47] At the same time, the interaction with the 3D structure is thought to increase the conductance of the membrane patch in contact with the structure,[48,55] thereby increasing the coupling efficiency. However, the overall geometry of the structures was found to greatly influence the engulfment,[49,56] with the coupling efficiency being dependent on the shape, size, and aspect ratio of the structure, as well as the position of the cell on top of the 3D structure and resulting coverage.[56] Another approach is the use of very high aspect ratio nanostructures, aiming to produce an impalement-like interaction with the cell.[51–53,57] To date, reports on the feasibility of this concept for electrophysiological studies, however, have been scarce. Recently, Liu *et al.*[58] reported unprecedented recording quality of up to 99 mV_{p2p} for mouse hippocampal neurons on high aspect ratio vertical nanowires, which is comparable to the signal amplitudes achieved with patch-clamp recordings. However, the range of potentials recorded as part of this study was reported as 0.1 to 99 mV_{p2p}, highlighting the large variability of signal amplitudes obtained with this method. Overall, the efficiency of the impalement approach as well as the criteria facilitating spontaneous penetration remain a topic of controversial debate. An alternative approach is the formation of hollow structures. In 2014, Lin *et al.*[50] reported significantly higher action potential recordings for hollow iridium oxide (IrOx) structures as compared to solid gold pillars. They attributed the differences in recording capability not only to differences in material, but also to the tendency of cells to protrude into openings as small as 100 nm in diameter, generating a positive curvature that could be advantageous for the coupling efficiency.[50]

As has been stated before, the coupling efficiency strongly depends on the sealing resistance. Furthermore, the coupling efficiency can also be increased by decreasing the junctional membrane resistance. While geometrical aspects of the 3D structures influence both parameters, the junctional membrane resistance can further be modified by application of short electrical pulses, which result in dielectric breakdown of the membrane.[59] This process, called electroporation, decreases the membrane resistance via the introduction of transient pores of 10-20 nm in size, which can result in an increase in signal amplitude of up to two orders of magnitude.[6] However, due to the transient characteristics of this approach, it cannot be the method of choice for long-term investigations into the behavior of neuronal networks.[5] Melosh *et al.* report a different approach, aiming to mimic the structure of transmembrane proteins by introducing hydrophobic bands of 3-5 nm to their 3D pillars,[60,61] which facilitates the insertion of the structure into the double layer structure

of the cell membrane. They reported up to GΩ sealing to red blood cells using this approach,[62] which is the benchmark for high quality sealing as achieved with patch-clamp pipettes.[59] However, reports on electrophysiological recordings using these devices are still missing. A recent example employing a variation of this concept is the publication by VanDersarl *et al.*,[59] employing 5 µm planar MEA electrodes encircled by a 5 nm gold ring which is functionalized with different alkanethiol self-assembled monolayers (SAMs). In this manner, they were able to establish a planar patch clamp-like configuration with 5 GΩ sealing resistance.[59] The usage of hydrophobic moieties for the interaction with cellular membranes is thus highly promising.

The aim of this body of work is to expand the toolbox of 3D electrodes by introduction of new geometries and development of well-controlled fabrication schemes. While Chapter 2 provides an overview over the theoretical background relevant to this field, Chapter 3 describes the development and fabrication of different 3D gold structures as well as their interaction with cardiomyocyte-like HL-1 cells and embryonic rat cortical neurons. Chapter 4 is concerned with the transfer of said structures to microelectrode arrays, the development of a controlled fabrication scheme for the preparation of different 3D designs on a single chip for a parallel evaluation of the influence of different 3D structures during electrophysiological investigations, as well as the recording of electrogenic activity from HL-1 cells employing the developed devices. In Chapter 5, various approaches for the modification of 3D structures towards more efficient coupling and better electrical characteristics are reported. Chapter 6 summarizes the obtained results and provides impulses for further investigations.

Chapter 2

Theoretical background

2.1 Electrodeposition

Electrodeposition is the process of an interfacial reduction of a metal ion M^{z+} to its elemental state M under application of a reducing potential.

$$M^{z+} + ze^- \overset{\text{reducing potential}}{\curvearrowleft} M \tag{2.1}$$

Apart from the nature of the metal ion M^{z+}, the metal-solution interface as locus of the reaction, the general thermodynamics and kinetics of the process, and the nucleation and growth mechanisms play a crucial role for this process.[63]

2.1.1 Electrochemical double layer

The interface between metal electrode and electrolyte is the locus of electrodeposition reactions and the characteristics of said interface are thus highly important for the overall process. When brought into contact with an electrolyte, metal surfaces form an **electrochemical double layer**. This is due to the establishment of an equilibrium between lattice bound metal atoms and hydrated metal ions in the interphase. Metal atoms leaving the lattice to go into solution as positively charged cations leave electrons behind and the metal surface thus acquires a negative charge. This charge is compensated by positive ions on the solution side. At equilibrium, the interphase is thus neutral, however, the ion distribution in the interphase is different from that of the bulk solution. Due to the accumulation of different charges on both sides of the interface, the electrochemical double layer exhibits capacitive characteristics. This plays a crucial role for electrochemical reactions

taking place at the interface since the 'capacitor' will get charged at the beginning of the reaction and will influence the electron transfer rate.[64] Several models have tried to provide a theoretical representation of the metal-electrolyte interface, the most basic being the **Helmholtz compact double layer model**, developed in 1879.[63] According to the Helmholtz model, the charges counterbalancing the charge of the metal are tightly bound to the surface and the interphase can be described as a parallel-plate capacitor. However, this model does not account for a dependence of the double-layer capacitance on the applied potential or any effect of thermal motion.[63,65] **Gouy and Chapman** proposed a different model, suggesting a diffuse double layer, with both negatively and positively charged ions distributed according to the Maxwell-Boltzmann statistic in an extended layer near the metal surface. While this model describes the experimentally observed behavior better than the Helmholtz model does, it fails in concentrated solutions.[63] **Stern** later combined both the Helmholtz and Gouy-Chapman model into one paradigm, consisting of a tightly bound, compact layer of fully hydrated ions at the electrode surface, and an extended diffuse layer beyond.[63] **Grahame** then extended the model to include partially hydrated, specifically adsorbed ions, which are in direct contact with the solid surface and form the **inner Helmholtz plane (IHP)**.[63] The center of fully hydrated ions defines the next layer, the **outer Helmholtz plane (OHP)**. Since the Helmholtz layer is analogous to a parallel plate capacitor, the potential between metal Φ_M and solution Φ_S decays linearly within the compact double layer. Beyond the OHP, the potential decays exponentially. Figure 2.1 shows a schematic representation of the electrode-electrolyte interface according to Grahame. The thickness of the double layer is usually taken as 1.5 λ_D, with λ_D being the **Debye length**,[64] the distance from the charged surface at which the potential has decayed by a factor of 1/*e*.[65] Here, *e* is Euler's number. λ_D is defined as

$$\lambda_D = \left(\frac{\varepsilon \varepsilon_0 k_B T}{e^2 \sum_i c_i z_i^2} \right)^{1/2} \tag{2.2}$$

where ε and ε_0 are the dielectric constant of the electrolyte and vacuum, respectively, k_B is the Boltzmann constant (k_B = 1.381·10^{-23} JK^{-1}), T the temperature, e = 1.602·10^{-19} C the elementary charge, c_i the bulk concentration of electrolyte i, and z_i its valency.[66] The thickness of the double layer is thus inversely proportional to the concentration of the electrolyte.

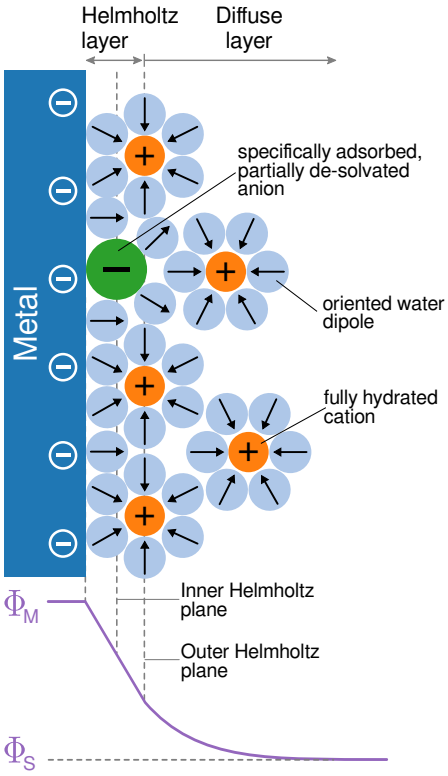

Figure 2.1: Electrochemical double layer according to Grahame. A negatively charged metal surface is in contact with a fixed layer of ions in the Helmholtz layer, with partially de-solvated, specifically adsorbed ions forming the inner Helmholtz plane (IHP), while fully hydrated ions form the outer Helmholtz plane (OHP). At larger distances, the ions form a diffuse layer according to Gouy-Chapman. The decay of the electrical potential between the metal electrode Φ_M and the bulk electrolyte Φ_S is linear in the Helmholtz layer due to the approximation as parallel plate capacitor, and exponential in the diffuse layer. Figure adapted from [63,65]

2.1.2 THE STANDARD ELECTRODE POTENTIAL

When coming into contact with a solution, different metals exhibit a different inclination to form ions going into solution, with base metals such as zinc (Zn) more readily releasing their valence electrons to form solvated ions than noble metals do.

$$\mathrm{Zn} \leftrightarrows \mathrm{Zn}^{2+} + 2\,\mathrm{e}^{-} \tag{2.3}$$

Hence, different metals differ in the double layer potential they establish when in contact with electrolyte. Since it is impossible to determine the potential of a single interface without a second reference point, the potential of different metal surfaces in solutions containing their cation at a concentration of 1 mol/L (standard conditions) have been tabulated against the potential of the **standard hydrogen electrode (SHE)**.[67] The SHE consists of a platinum electrode that is bathed in

hydrogen gas at a pressure of 101.3 kPa and submerged in a solution with an H^+ activity $a(H^+) = 1$. The potential of the SHE has been defined as 0 and all **standard potentials** are reported with respect to the reduction reaction in relation to the SHE.[67] Each metal plus its ion-containing solution form a half-cell with its own, characteristic potential, with each pair of reduced and the corresponding oxidized species being called a redox pair. Table 2.1 lists the electrochemical standard potential for different compounds. Redox pairs with lower standard potential act as reducing agents for redox pairs with higher standard potential.

Table 2.1: Electrochemical standard potential for exemplary materials.[67] Each pair of oxidized and reduced species *e.g.* $Cu^{2+}|Cu$ is called a redox pair. A higher standard potential signifies a higher tendency to occur in the reduced form, with potentials beyond the standard potential needed to oxidize the substance. Vice versa, a lower reduction potential represents a higher tendency to occur in the oxidized form, with potentials below the standard potential needed to shift the equilibrium to the reduced state.

Oxidized form	$+ ze^-$	**Reduced form**	E_0 **[V]**
Au^+	$+ e^-$	$\leftrightarrows Au$	+1.71[68,69]
$O_2 + 4\,H^+$	$+ 4\,e^-$	$\leftrightarrows 2\,H_2O$	+1.229
Cu^{2+}	$+ 2\,e^-$	$\leftrightarrows Cu$	+0.337
$2\,H^+$	$+ 2\,e^-$	$\leftrightarrows H_2$	0
$[Au(CN)_2]^-$	$+ e^-$	$\leftrightarrows Au + 2\,CN^-$	-0.61[69]
Zn^{2+}	$+ 2\,e^-$	$\leftrightarrows Zn$	-0.763
$2\,H_2O$	$+ 2\,e^-$	$\leftrightarrows H_2 + 2\,OH^-$	-0.828
Li^+	$+ e^-$	$\leftrightarrows Li$	-3.045

For the electrochemistry of substances in aqueous solution, the potential region between -0.828 V and +1.229 V against SHE is particularly important. This region is called the **water window**, the potential window within which water is stable both against reduction and oxidation. For potentials above +1.229 V, water is oxidized to oxygen and hydrogen ions, for potentials below -0.828 V, water is reduced to hydrogen and hydroxide ions. For any electrochemical reaction occurring outside this potential window, the oxidation or reduction of water is thus a competing reaction.

Connecting two redox pairs from Table 2.1 like demonstrated in Figure 2.2 can result in the reduction of one of the metals to its elemental state while the other metal is oxidized to form metal ions. The setup depicted in Figure 2.2 is called a **galvanic cell**, each redox pair constitutes a half cell. In a galvanic cell, the electrochemical reaction occurs spontaneously once both cells are connected by a conducting material. Cells where the reaction occurs due to the application of an external voltage are termed **electrolytic cells**.[70] Electrolytic cells can be used for the deposition of materials

such as during electrodepositions or for the electrolytic synthesis of elements from compounds or synthesis of chemicals from redox-active building blocks.

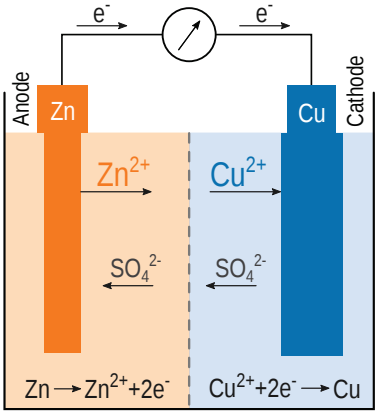

Figure 2.2: Schematic representation of a galvanic cell. A zinc electrode is submerged in a zinc sulfate solution and a copper electrode is submerged in copper sulfate solution. The solutions are separated by a semi-permeable membrane and the electrodes are electrically connected. Zinc, having the more negative standard potential, is the stronger reducing agent. Therefore, zinc atoms go into solution, degrading the zinc electrode and providing electrons for the reduction of copper, which is deposited on the copper electrode. The potential generated by this cell is ΔE_0 = 1.10 V. Figure adapted from [67]

If both redox pairs of a galvanic cell are present at standard conditions, the potential generated between the two cells can be calculated from the difference of their standard potentials [67]

$$\Delta E = E_0^{\text{Reduction}} \quad E_0^{\text{Oxidation}} \tag{2.4}$$

and thus for the given galvanic cell [67]

$$\begin{aligned} \Delta E &= E_0(Cu^{2+}|\,Cu) \quad E_0(Zn^{2+}|\,Zn) \\ &= 0.337\,\text{V}\text{-}(\text{-}0.763\,\text{V}) \\ &= 1.10\,\text{V} \end{aligned} \tag{2.5}$$

However, the different reactants of an electrochemical reaction are not always present at standard conditions. For an exemplary reaction of reactant B and G to products X and Y [67]

$$bB + gG \leftrightarrows xX + yY \tag{2.6}$$

the **Nernst Equation** enables the calculation of the potential of the reaction based on the difference in standard potential ΔE_0 and the activity a of the reactants. [67]

$$\Delta E = \Delta E_0 \quad \frac{RT}{zF} \pm\ln\frac{a^x(X) \pm a^y(Y)}{a^b(B) \pm a^g(G)} \tag{2.7}$$

where R = 8.314 J mol^{-1} K^{-1} is the ideal gas constant, z is the number of transferred electrons, and F = 96485.33 C mol^{-1} is Faraday's constant. The chemical activity a of species m depends on the product of its activity coefficient γ_m and concentration c_m, thus $a_m = \gamma_m \pm c_m$. In dilute solutions, the difference between a_m and c_m is generally small and the activity can be exchanged for the concentration. Per definition, the activity of solids and electrons is a = 1.[63]

While all standard potentials are tabulated against the SHE, for practical applications, other, more convenient reference electrodes are employed. Most commonly, these electrodes follow the concept of being a metal M with its insoluble salt MA in electrolyte containing A^{z-}. The metal M then is in equilibrium with its oxidized form M^{z+} inside the salt MA, while the anions A^{z-} are in equilibrium between electrolyte and salt.[63]

$$\begin{aligned} M^{z+} + ze^- &\leftrightarrows M \\ MA &\leftrightarrows M^{z+} + A^{z-} \\ \hline MA + ze^- &\leftrightarrows M + A^{z-} \end{aligned} \tag{2.8}$$

Since both M and MA are solids with activity a = 1, the Nernst equation for this system yields[63]

$$E = E_0 \pm \frac{RT}{zF} \ln[A^{z-}] \tag{2.9}$$

The potential of the overall reaction is thus solely dependent on the activity of the anion A^{z-} in the electrolyte.[63] A common example for such an electrode is the **silver/silver chloride (Ag/AgCl)** system, where Ag is covered with a layer of insoluble AgCl and immersed in a Cl^- containing solution. If the chloride containing solution is saturated KCl, the silver/silver chloride electrode has a potential of 0.197 V vs. SHE.[63]

It has to be noted, however, that the Nernst equation is only valid if the reaction is at equilibrium. During electrolytic reactions, when a potential is applied to facilitate an electrochemical reaction that does not proceed spontaneously, the metal-electrolyte interface is not at equilibrium and the potential cannot be determined using the Nernst equation. This is particularly problematic for experiments aiming to investigate the electrochemical properties of a redox system for example via cyclic voltammetry, where the potential is linearly varied between two points and the resulting

peaks in the current are employed to investigate the kinetics and thermodynamics of electrochemical reactions.[64] Without a stable reference potential, the applied potential cannot be determined since the acting electrochemical driving force will influence the potential of the electrodes employed. Therefore, it is neither possible to warrant that the applied potential is varied linearly, nor can the potential at which the reaction occurs be determined accurately. Therefore, electrochemical reactions that are conducted while applying a potential are commonly set up employing a **three-electrode setup**, with the reference electrode in parallel to the working electrode, away from the flow of current and thus at a stable reference potential, while the current flows between working and an auxiliary or counter electrode (Figure 2.3).

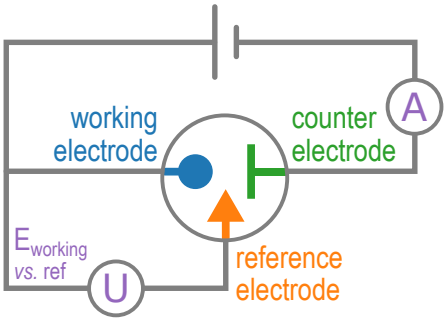

Figure 2.3: Schematic representation of the three-electrode setup. The potential is measured between the working electrode and the reference electrode while the current runs between working and counter electrode. Since the reference electrode is outside of the way of current, it exhibits a stable potential in accordance with the Nernst equation. Figure adapted from[70]

2.1.3 Kinetics

While the Nernst equation enables the calculation of the electrode potential at thermodynamic equilibrium, an electrode in contact with electrolyte that is connected to an electrical circuit and experiences the flow of current will exhibit a potential E that is different from the equilibrium potential E_0. The difference between these two potentials is the **overpotential** η.[70]

$$\eta = E \quad E_0 \tag{2.10}$$

In contrast to homogeneous reactions, where the kinetics of the reaction depend solely on the temperature,[70] heterogeneous reactions - reactions occurring at the interface between electrode and electrolyte - show a dependency of their reaction rate on the applied potential.[70] The **Tafel**

equation describes the empirical relationship between overpotential η and current density j [63]

$$\eta = a + b \pm \log j \tag{2.11}$$

where a and b are constants. The reaction rate v can also be described as a function of the current density j [70]

$$v = \frac{j}{zF} \tag{2.12}$$

where z is the number of transferred electrons and F is Faraday's constant. The reaction rate is thus linearly dependent on the current density and exponentially dependent on the overpotential. A more detailed relationship between the current density j and overpotential η is provided by the **Butler-Volmer equation** [63,71]

$$j = j_0 \pm \left(\exp\left[\frac{(1 \quad \alpha) zF}{RT} \eta \right] \quad \exp\left[\quad \frac{\alpha zF}{RT} \eta \right] \right) \tag{2.13}$$

where R is the ideal gas constant, T the temperature in Kelvin, j_0 is the exchange current density, so the current density at equilibrium, where $E = E_0$, and α the transfer coefficient. [63] α is a measure for the symmetry of the thermodynamic energy barrier [70] and is most often taken as α = 0.5. [63] It has to be noted, however, that the Butler-Volmer equation is only valid for reactions that are limited due to their charge transfer step. If the reaction is limited by mass transport, the Butler-Volmer equation does not apply.

2.1.4 Nucleation and growth

Several steps and energetic criteria are involved in the nucleation of seeds and the growth of material during electrodeposition. Metal ions from solution first need to approach the surface either via electrostatic attraction or diffusion, and then need to adsorb to the surface before charge transfer and lattice incorporation can occur.

$$\begin{aligned} M^{z+}_{solution} &\propto M^{z+}_{adsorbed} \\ M^{z+}_{adsorbed} + ze^- &\propto M_{lattice} \end{aligned} \tag{2.14}$$

Figure 2.4[72] depicts the mechanism for a ligand coordinated metal ion. In the easiest case, the ligands are water molecules.

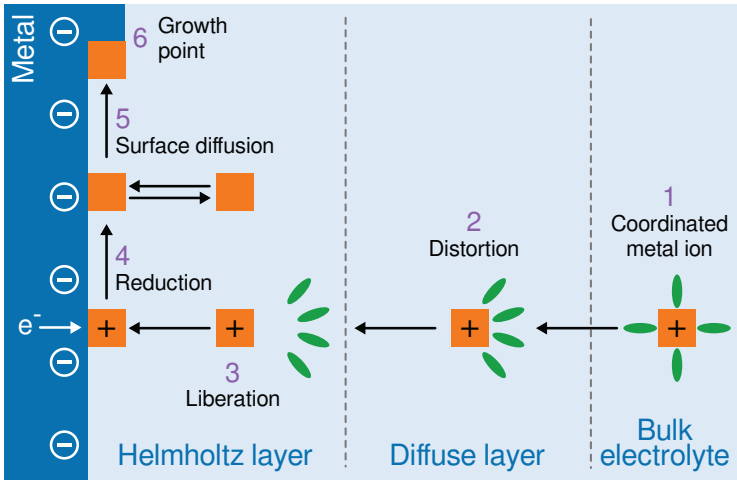

Figure 2.4: Schematic representation of the steps occurring for the nucleation of seeds during electrodeposition. A fully coordinated metal ion (1) diffusing from the bulk solution into the diffuse layer experiences a distortion of its ligand shell (2) and finally liberation from its ligands inside the Helmholtz layer (3). The ion adsorbs to the surface where it can be reduced (4). The resulting adatom has a low surface binding energy and can easily desorb. Surface diffusion (5) occurs until a stable lattice position is found, which is usually at crystal defects such as kinks, which serve as growth points (6). Figure adapted from[72]

They can, however, be bigger and more complex moieties, potentially even resulting in a negatively charged complex that results in an approach that is electrostatically unfavored and occurs merely diffusively. Upon approach of the surface, the metal ion experiences a distortion of the ligand field (2) and, upon closer approach, liberation from the coordinated ligands inside the Helmholtz layer (3). It can then adsorb to the surface, where reduction occurs (4), followed by surface diffusion to a suitable growth point that facilitates a higher binding energy and thus incorporation into the lattice. However, the adatom does not necessarily become incorporated into the lattice. Since the binding energy of an adatom is much lower than for a bulk atom due to the much lower number of neighbors, adatoms can easily desorb from the surface. Therefore, crystal growth occurs primarily at growth points such as lattice defects and kink sites, where the adatom finds a larger number of binding partners.

Whether a growing seed is stable or not depends on the free energy of the formation of the cluster $\Delta G(N)$ [73]

$$\Delta G(N) = \quad Nze\,\eta \; + \phi(N) \tag{2.15}$$

where N is the number of atoms, e is the elementary charge, and $\phi(N)$ is an energy term related to the increase in surface energy resulting from the formation of the cluster. Since the geometry of the cluster has a great influence on the surface-to-volume ratio and thus surface energy term, $\phi(N)$, $\Delta G(N)$ is geometry dependent. While the first term of the free energy is proportional to N, the second term is proportional to $N^{2/3}$ since the surface-to-volume ratio decreases with increasing number of seed atoms, resulting in a negative $\Delta G(N)$ only for larger N [74] (Figure 2.5). Depending

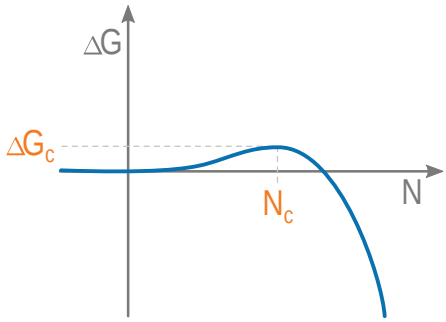

Figure 2.5: Free energy $\Delta G(N)$ of the formation of a cluster in dependence on the number of atoms N. Clusters are stable if $\Delta G(N) < 0$. For small clusters, $\Delta G(N)$ is positive due to the dominance of the increase in surface energy over bulk effects. Small clusters are thus unstable. Clusters of the critical size N_c have equal probability of growth and dissolution. Figure adapted from [63]

on the cluster size and thus free energy, adatoms will either remain on the surface and become incorporated into the lattice, or will desorb and return into solution. At the critical cluster size N_c, the growing cluster has an equal probability for growth and dissolution. The 3D growth of crystals depends on a myriad of parameters, such as the overpotential, the concentration of adatoms, the relationship between the rate of nucleation and propagation, and the differences between substrate material and deposit, as well as the kind and number of defects on the substrate. If, for example, the nucleation rate is significantly slower than the growth rate, one nucleus will cover the entire surface before a new nucleus is formed, resulting in mononuclear layer-by-layer growth, which usually occurs at low overpotentials. [63] If, however, the nucleation rate is much faster than the propagation rate, each monolayer is formed by coalescence of multiple nuclei. If substrate and deposit consist of different materials, the growth mode depends on the interaction between the materials. [74] If the binding energy Ψ between the adsorbed metal M_{ads} and substrate S is lower than the binding energy between M and its native substrate, growth occurs according the

Volmer-Weber mechanism, with the formation and coalescence on 3D islands (Figure 2.6 a).[74]

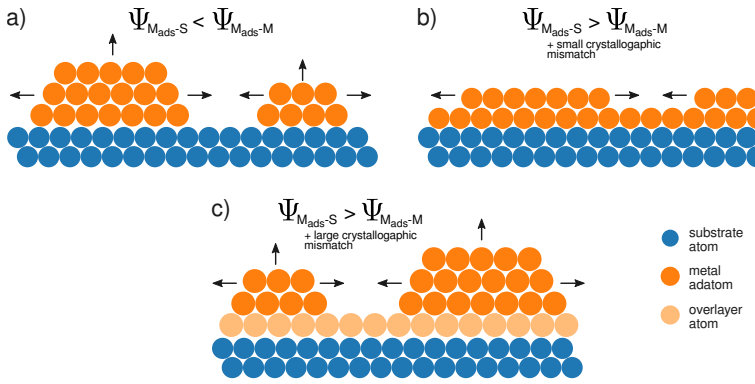

Figure 2.6: Different mechanisms for crystal growth. (a) Volmer-Weber: A higher binding energy Ψ between the metal atoms M_{ads} and M than between the adsorbed metal M_{ads} and substrate S results in the formation of three-dimensional islands. Layer growth occurs through coalescence of islands. (b) Frank-van der Merwe: $\Psi(M_{ads}\text{-}S) > \Psi(M_{ads}\text{-}M)$ and negligible crystallographic mismatch between metal and substrate results in a layer-by-layer growth of the crystal. (c) Stranski-Krastanov: $\Psi(M_{ads}\text{-}S) > \Psi(M_{ads}\text{-}M)$ but significant lattice mismatch results in the formation of a metal overlayer followed by Volmer-Weber-like growth. Figure adapted from[74]

If the binding energy Ψ between the adsorbed metal M_{ads} and substrate S is higher than the binding energy between M and its native substrate and the crystallographic mismatch is negligible, the growth occurs according to a layer-by-layer mechanism or **Frank-van der Merwe** growth (Figure 2.6 b), which is also the characteristic growth mode for the deposition of M on a substrate of the same material.[74,75] In cases where there is a significant crystallographic mismatch, M atoms form an overlayer on S, followed by 3D island formation (**Stranski-Krastanov** mechanism, Figure 2.6 c).[63,74] Furthermore, the adsorption of additives can greatly influence the crystal growth by influencing the concentration of growth sites and thus frequency of nucleation, changing the concentration of adions and their diffusion, and by preferential adsorption either at peaks or on flat surfaces.[63]

2.1.5 Electrodeposition of gold

The physical and chemical characteristics of gold such as high electrical and thermal conductivity, corrosion resistance, and inertness[69] make it an important material for microelectronic applications.[76] While gold can be processed via a variety of methods such as physical vapor deposition (PVD), chemical vapor deposition (CVD), or atomic layer deposition (ALD), the electrodeposition

of gold facilitates an easy access to thicker layers with or without templating, as well as a uniform coating of three-dimensional surfaces. For industrial applications, gold is most often deposited from the gold(I)cyanide complex since Au^+ is highly unstable in aqueous solution, with a theoretically determined standard potential of approximately 1.71 V vs. SHE.[68,69] While other complexes such as gold(I)sulfite and gold(I)thiosulfate have been gaining more industrial utilization due to the inherent health risks of employing cyanide-containing plating solutions, the $[Au(CN)_2]^-$ complex remains the material of choice due to its superior stability. In aqueous solution, $[Au(CN)_2]^-$ is at equilibrium with its dissociated ions Au^+ and CN^-[72]

$$[Au(CN)_2]^- \leftrightarrows Au^+ + 2\,CN^- \tag{2.16}$$

The stability constant β for the reaction is defined as

$$\beta = \frac{[Au(CN)_2]^-}{[Au^+] \pm [CN^-]^2} \tag{2.17}$$

with β being 10^{38}.[72] The considerable stability is also reflected in the shift to a significantly lower standard potential of -0.61 V vs. SHE as compared to that of uncomplexed Au^+.[69] Due to the high stability of the complex and low concentration of free Au^+, the mechanism for the deposition remains a matter of debate. Several theories have been established, either based on a full stripping of the cyanide ligands according to Equation 2.16 and Figure 2.4 inside the Helmholtz layer,[72] a direct reduction[77]

$$[Au(CN)_2]^- + e^- \leftrightarrows Au + 2\,CN^- \tag{2.18}$$

or a two step process via an intermediate adsorbed species[77]

$$\begin{aligned} [Au(CN)_2]^- &\propto AuCN_{adsorbed} + CN^- \\ AuCN_{adsorbed} + e^- &\propto Au + CN^- \end{aligned} \tag{2.19}$$

Bozzini *et al.*[77] determined that the mechanism in Equation 2.18 occurs at high cathodic overpotentials, while the mechanism in Equation 2.19 occurs at low overpotentials. However, it is challenging to formulate generalized theories since the behavior of the plating bath is highly dependent on the nature and concentration of additives, as well as the pH of the solution. Equation 2.20

depicts the reactions occurring at the cathode and anode for the electrodeposition of gold from $K[Au(CN)_2]$, the most commonly used salt of the gold(I)cyanide complex due to its good solubility.[69]

$$\begin{aligned} &\text{Cathode: } 4\ K[Au(CN)_2] + 4e^- \propto 4\ Au + 4\ KCN + 4\ CN^- \\ &\text{Anode: } 2\ H_2O \propto 4\ H^+ + O_2 + 4\ e^- \\ \hline &\text{Full cell: } 4\ K[Au(CN)_2] + 2\ H_2O \propto 4\ Au + 4\ HCN + 4\ KCN + O_2 \end{aligned} \tag{2.20}$$

The literature reports a multitude of different gold bath formulations based on $K[Au(CN)_2]$. They differ in the concentration of the gold salt itself, the supporting electrolyte, pH, and nature of additives, all of which are influential parameters with respect to the characteristics of the deposit. While gold deposition is performed over a wide range of pH values, a lower pH, for example, and the resulting higher concentration of H^+ ions, favor the formation of hydrogen as competing reaction to gold deposition.[69] Changes in the temperature of the deposition change the amount of carbon incorporation, with temperatures of around 25°C promoting higher carbon contamination and harder, more brittle deposits, than depositions at 65°C.[69] In general, gold deposited from gold(I)cyanide tends to exhibit carbon, nitrogen, and potassium impurities.[68] The presence of additives also has a strong influence on the mechanical properties of the deposits. Metal co-deposits tend to adsorb to the cathode and facilitate an even nucleation and thus smoother deposits due to a larger number of nucleation sites as compared to the unaided nucleation at growth points,[72] and co-deposition of transition metals such as cobalt, nickel, or iron can harden the deposited gold.[69] Organic moieties such as polyethyleneimines tend to adsorb at growth points and thus result in a smoothing of the surface due to the masking of said growth points.[72] However, a complete description of the influence of different additives is highly complicated due to the complex interaction of the different effects, making an accurate prediction of the morphology of the resulting deposit challenging. Another important parameter is the interplay between the overpotential and resulting kinetics and the concentration and resulting tendency towards diffusion limitation, which is particularly important for gold(I)cyanide, since the $[Au(CN)_2]^-$ anion is not electrostatically attracted to the cathode and the supply is thus entirely diffusion controlled.[72] For depositions at a constant current density, decreasing the salt concentration results in the formation of sharp, pointy crystals since the fast depletion of $[Au(CN)_2]^-$ near the cathode results in the immediate reduction at growth points reaching further into the solution (spikes).[78] For the deposition from a solution

of a constant concentration, the application of low current densities and thus low overpotential results in a preferential growth at existing seeds and thus sharp, spiky deposits, while a higher current density results in the formation of more seeds and thus smoother surfaces.[78] For very high overpotentials, however, the depletion of $[Au(CN)_2]^-$ in the vicinity of the cathode and resulting diffusion limitation again forms spiky deposits,[79] comparable to the mechanism observed for low salt concentrations. Additionally, higher overpotentials will also result in the formation of hydrogen at the cathode due to the deposition outside the water window and resulting reduction of water. Overall, the effects of plating bath composition and deposition parameters on the resulting deposits are multifaceted and complex, making a direct prediction challenging.

2.2 Electrophysiology

The cell is the smallest unit of life and while there are many organisms consisting of just a single cell such as *e.g.* bacteria, multicellular organisms consist of a variety of different, highly specialized cells. Their interplay of function and communication enables the complex processes that make up human life and interaction. In many cases, the function and communication of cells is based on chemical agents such as proteins or transmitters. However, some cells additionally exhibit electrical activity. The field of electrophysiology is concerned with the study of these **electrogenic cells**. One highly important member of this group are neurons, the building blocks of our nervous system. As the functions of our nervous system are diverse - from the detection of odors, sounds, or pain, to the processing of information and coordination of muscle movement - so are the neurons that constitute our nervous system. However, many types of neurons follow the general structure depicted in Figure 2.7. They consist of a soma or cell body hosting the cell nucleus, and two

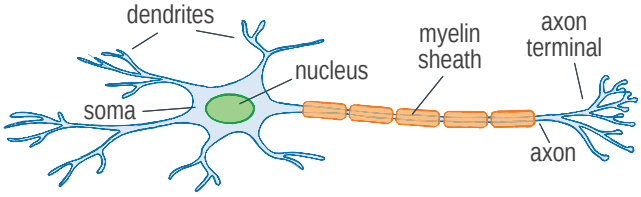

Figure 2.7: Schematic structure of a neuron: The soma or cell body contains the cell nucleus. From there, two types of processes extend towards neighboring cells. While dendrites are responsible for the receipt of information, one long process called axon transmits information to downstream neurons via connections between the axon terminal of cell A and the dendrites of cell B. To decrease the signal attenuation, axons are often encased in a shielding substance, the myelin sheath.

types of processes: **dendrites** for the receipt of information from neighboring cells and an **axon** for the transmission of information to other cells via contacts between the axon terminal of cell A with dendrites of cell B. Within the cell, neurons transmit information via electrical impulses traveling along the cell membrane, with ion channels enabling the transport of charges across the membrane and thus the establishment of a potential difference. While Galvani proposed the idea of bioelectricity as early as 1780, it took until the investigations of Hodgkin and Huxley, published in 1952,[80] to explain the phenomenon of animal electricity.

2.2.1 Resting potential

Animal cells are enclosed by a six to eight nanometer thick phospholipid bilayer,[81] also called **cell membrane**. The cell membrane is highly functionalized, containing a large variety of transmembrane proteins facilitating interaction with the environment as well as transport between the intracellular and extracellular regime. Furthermore, the membrane plays an important role for the electrical properties of the cell through the establishment of a potential difference between the intra- and extracellular side. For the generation of the membrane potential, ion channels are the most important of the aforementioned transmembrane proteins. Ion channels can either be **passive**, allowing ion passage by mere diffusion, **gated**, therefore allowing diffusion only if a stimulus is applied, or **active transporters**, moving ions across the cell membrane against their concentration gradient under usage of adenosine triphosphate (ATP) (Figure 2.8).

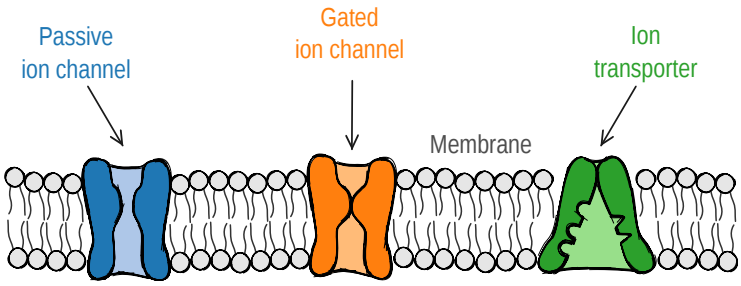

Figure 2.8: The cell membrane consists of a phospholipid bilayer with integrated transmembrane proteins. For the establishment of the resting potential, the cell relies on passive and gated ion channels as well as ion transporters to control the necessary concentration differences.

At rest, the cell primarily allows the diffusion of potassium along its concentration gradient due to the presence of passive potassium channels. The diffusion of potassium from the intracellular

Table 2.2: Intra- and extracellular concentrations of common ions in vertebrate neurons.[82] At rest, potassium has the highest influence on the membrane potential, the neuronal resting potential is thus close to the equilibrium potential of K^+.

Ion species	Intracellular concentration (mM)	Extracellular concentration (mM)	Equilibrium potential [mV]
K^+	96	4	-85
Na^+	10	145	+71
Ca^{2+}	$7 \cdot 10^{-5}$	2	+137
Cl^-	7	145	-80

to extracellular side results in an extracellular excess of positive charges. An equilibrium is established once the driving force of the concentration gradient equals that of the electrostatic repulsion caused by the build-up of positive charges. The exterior is now slightly positively charged, the interior slightly negatively (Figure 2.9). The difference between intra- and extracellular potential yields the membrane potential E_m. If only one species of ions were involved, exhibiting different concentrations on both sides of a semi-permeable membrane as schematically depicted for potassium in

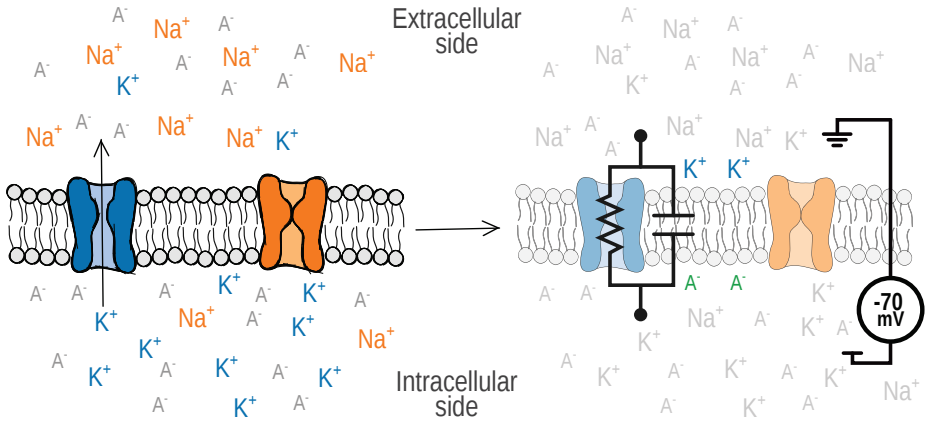

Figure 2.9: Establishment of the resting potential: Potassium travels along its concentration gradient from the intracellular to the extracellular side, resulting in an extracellular built-up of an excess positive charge. The resulting electrostatic repulsion acts as counterforce to the concentration gradient-driven diffusion. The small imbalance between positive and negative charge on the extra- and intracellular side yields a potential difference, the resting potential. In neurons, the resting potential is at around -70 mV. In an electrical circuit analogue, the ion channels are equivalent to resistors, while the phospholipid bilayer exhibits capacitive characteristics.

Figure 2.9, the potential could be described according to the Nernst equation:[81]

$$E_m = \frac{RT}{zF} \cdot \ln \frac{[X]_e}{[X]_i} \tag{2.21}$$

where R = 8.314 J mol^{-1}K^{-1} is the universal gas constant, T the temperature in Kelvin, z the valency of the ion, F = 96485.33 C mol^{-1} is Faraday's constant, and $[X]_e$ and $[X]_i$ the extra- and intracellular concentration of the ion X, respectively. Due to the large influence of potassium, the resting potential of neurons is usually close to the equilibrium potential of potassium, which is approximately -85 mV at 37°C (310.15 K) as calculated from the intra- and extracellular concentrations for K^+ listed in Table 2.2 by application of the Nernst equation

$$E_m = \frac{8.314\,\text{J mol}^{-1}\text{K}^{-1} \cdot 310.15\,\text{K}}{96485.33\,\text{C mol}^{-1}} \cdot \ln \frac{4\,\text{mM}}{96\,\text{mM}} \tag{2.22}$$

$$= \quad 0.085\,\text{V} \tag{2.23}$$

However, for a more exact calculation of the resting potential, all involved ion species have to be considered. This can be done employing the **Goldman-Hodgkin-Katz (GHK) equation**, an extended Nernst equation, which also includes the sodium and chloride concentration.[81]

$$E_m = \frac{RT}{F} \cdot \ln \frac{P_K[K]_e + P_{Na}[Na]_e + P_{Cl}[Cl]_i}{P_K[K]_i + P_{Na}[Na]_i + P_{Cl}[Cl]_e} \tag{2.24}$$

In addition to the consideration of all relevant ions, the GHK equation also includes the ease with which ion X travels across the membrane, the permeability P_X. Therefore, ions for which the membrane exhibits a larger permeability will have a stronger influence on the resting potential. While the Nernst equation is only valid at equilibrium, the GHK equation is valid at steady state, where the net ion current across the membrane is equal to zero and the membrane potential is thus not changing.[83]

2.2.2 The action potential

If a stimulus raises the membrane potential above the **threshold potential**, an electrogenic cell fires an **action potential (AP)**. An action potential is an all-or-none event, reaching the threshold potential induces a cascade of cell-specific ion channel activity that quickly changes the membrane

potential by several tens of millivolts.[81] In neuronal cells, the increase of the membrane potential from rest at around -70 mV to approximately -50 mV will open voltage-gated sodium channels, resulting in rapid sodium influx. During this phase, also called depolarization (Figure 2.10 B), the membrane potential increases up to +30 mV. With a slight delay, voltage-gated potassium channels open, resulting in an outflux of K^+ and resulting decrease in the membrane potential (Figure 2.10 C). At the same time, the voltage-gated sodium channels become inactivated, stopping the

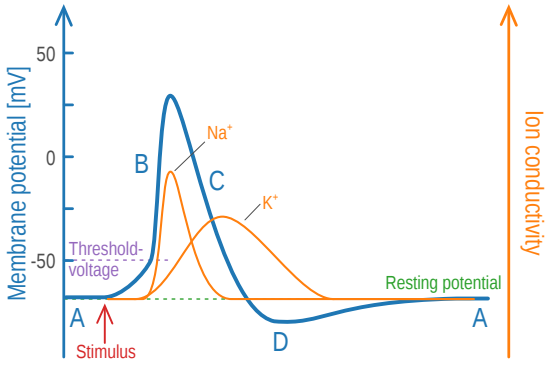

Figure 2.10: The neuronal action potential: An increase of the membrane potential from its resting value (A) to the threshold voltage results in the opening of voltage-gated sodium channels and rapid increase in membrane potential (B). While the sodium channels quickly become inactivated after this depolarization phase, voltage-gated potassium channels open and potassium outflux results in a decrease in membrane potential or repolarization (C). During this phase, the membrane potential actually drops below its resting value, resulting in hyperpolarization (D), at which point the voltage-gated potassium channels are deactivated. Figure adapted from[81,84]

sodium influx and therefore enabling the repolarization of the cell. During this phase, the membrane potential eventually drops below the resting potential (hyperpolarization, Figure 2.10 D), at which point the voltage-gated potassium channels close. This sequence occurs for each point x on the membrane, which then results in the activation of neighboring point y due to the increase in membrane potential beyond threshold and subsequent firing of an action potential in point y, which triggers the cascade for neighboring point z. In this manner, the action potential can quickly travel along a membrane, propagating similar to a wave on water.

As already noted above, the cascade triggered by reaching the threshold potential is highly cell dependent, contingent on the variety of ion channels present in the cell membrane and their behavior with respect to gating and inactivation. Therefore, the action potential in *e.g.* cardiac cells looks significantly different, even within different regions of the heart. Here, two distinct behaviors can be distinguished - that of the **cardiac myocyte** and that of the **pacemaker**. Since the heart needs to perform rhythmic contractions, pacemaker cells exhibit autorhythmicity: They do not show a stable resting potential but continuously depolarize due to special sodium channels

(funny channels) (Figure 2.11 a, phase 4).[85] Once the threshold potential is reached, pacemaker cells fire an action potential due to an influx of calcium and resulting increase in membrane potential (Figure 2.11 a, phase 0). The opening of potassium channels then repolarizes the cell (Figure 2.11 a, phase 3). Afterwards, the funny current slowly raises the membrane potential to threshold again. In contrast, cardiac myocytes cannot depolarize autonomously but need an external

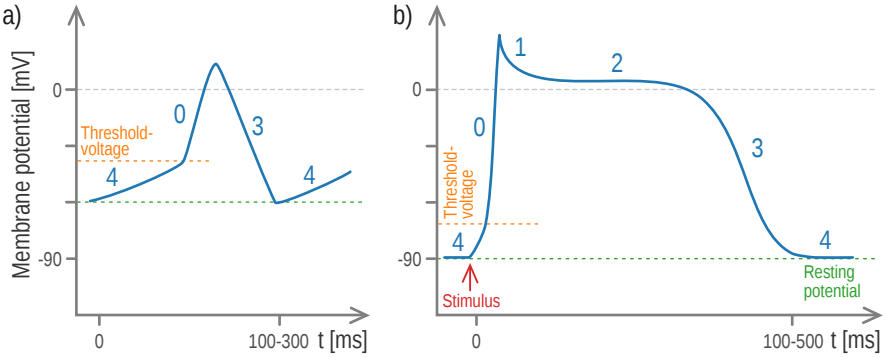

Figure 2.11: The cardiac action potential. a) Pacemaker cell: specialized sodium channels (funny channels) result in a slow sodium influx, raising the potential to threshold (phase 4). The cell then fires an action potential due to the influx of calcium through voltage-gated Ca^{2+} channels (phase 0). Repolarization occurs due to the closing of the calcium channels and opening of potassium channels and consequent K^+ outflux. b) Cardiac myocyte action potential: A stimulus that raises the membrane potential from resting (phase 4) to threshold triggers an action potential due to a rapid influx of sodium through voltage-gated sodium channels (phase 0). During phase 1, Na^+ channels close and K^+ channels open, resulting in a rapid initial repolarization, followed by calcium influx in phase 2, balancing the K^+ outflux and keeping the membrane potential almost constant. Repolarization occurs once the calcium channels close, allowing for potassium outflux to return the potential back to the resting potential (phase 3). Figure adapted from[86,87]

stimulus that raises their membrane potential from the resting potential (Figure 2.11 b, phase 4) to threshold. This is followed by a rapid influx of sodium (Figure 2.11 b, phase 0), depolarizing the cell to approximately +30 mV.[86] While pacemaker cells are classified as 'slow AP cells' with a maximum change in membrane potential of approximately 10 V/s in phase 0, the membrane potential change in cardiac myocytes during phase 0 is very rapid with up to 200 V/s. Subsequently, cardiac myocytes experience a rapid initial repolarization due to an outflux of potassium (Figure 2.11 b, phase 1), followed by a plateau (Figure 2.11 b, phase 2) where the potassium outflux is balanced by calcium influx.[86] This phase facilitates muscle contraction since the influx of calcium triggers further calcium release from the sarcoplasmic reticulum. Binding of calcium to tropomyosin then enables the contraction of the muscle fibers via the interaction between actin and myosin. After-

wards, the cell repolarizes due to potassium outflux (Figure 2.11 b, phase 3). While neuronal action potentials last about 10 ms, pacemaker action potentials last between 100 and 300 ms and action potentials in cardiac myocytes up to 500 ms.[86]

2.2.3 Cell-cell transmission

Within one cell, the action potential is propagated by each membrane segment triggering the neighboring segment to also fire an action potential. Between cells, the action potential is transmitted through synapses - cell-cell contacts that can either be chemical or electrical in nature. At **chemical synapses**, an incoming action potential triggers the exocytosis of chemical moieties called **neurotransmitters** (Figure 2.12). The transmitters diffuse from the presynaptic terminal

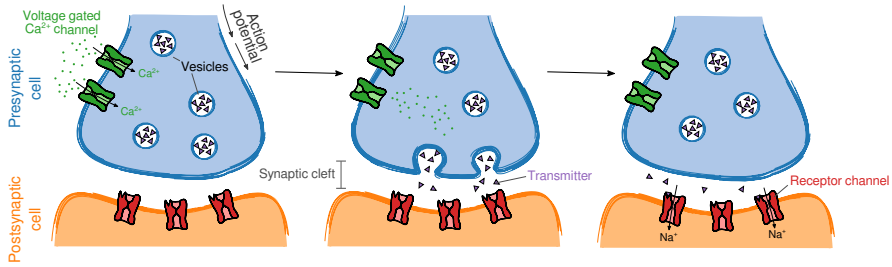

Figure 2.12: Chemical synapse: An action potential triggers the opening of voltage-gated calcium channels and subsequent Ca^{2+} influx. The increased intracellular calcium concentration triggers the fusion of neurotransmitter-containing vesicles with the presynaptic membrane. The neurotransmitter then bind to receptor channels at the postsynaptic neuron, triggering sodium influx, thereby changing the membrane potential of the postsynaptic terminal. Figure adapted from[81]

across the synaptic cleft to the postsynaptic cell, where the binding to receptors triggers an influx of sodium. This changes the membrane potential and, if the threshold potential is reached, triggers an action potential in the postsynaptic cell (Figure 2.12). The synaptic cleft dividing pre- and postsynaptic cell is usually between 20 and 40 nm, with the dependence on neurotransmitter release, diffusion, and recognition resulting in a delay in signal propagation of 1 to 5 ms.[81] Another important characteristic of chemical synapses is their unidirectional nature, with communication running from the pre- to the postsynaptic cell. In contrast, **electrical synapses** or **gap junctions** are specialized channels that form direct connections between cells and do not rely on neurotransmitters. Each cell contributes a hemichannel or connexon, two connecting hemichannels in neighboring cells make up a gap junction channel (Figure 2.13). Due to the direct contact

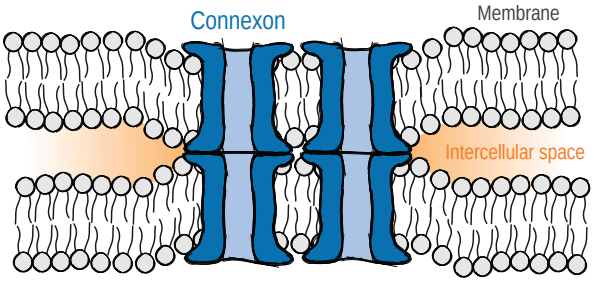

Figure 2.13: Electrical synapses or gap junctions are direct connections between cells. They consist of specialized channels called connexons, that allow the direct transmission of current between cells. Due to the direct ion-current transmission, the communication between cells via electrical synapses is significantly faster than in chemical synapses. Figure adapted from [81]

and cytoplasmic continuity, ion currents can be directly transmitted between cells without delay and without directional restrictions, making this kind of synaptic transmission much faster than chemical synapses.[81] While the nervous system makes use of both modes of signal transmission, cardiac cells communicate exclusively via electrical synapses.

2.2.4 Recording electrogenic activity

The gold standard for the investigation of the electrical activity of biological tissues, electrogenic cells, and specific ion channels, is the **patch-clamp technique**. During patch-clamp recordings, a small diameter glass pipette is brought into contact with the cell membrane. The glass pipette is filled with electrolyte and contains a conductive wire as electrode that measures potentials with respect to a Ag/AgCl reference electrode. Employing this technique, Erwin Neher and Bert Sakman were able to perform their experiments on the activity of single ion channels in frog muscle fibers as early as 1976,[3] a study that later earned them the Nobel Prize in 1991. Different modes of operation can be employed during patch-clamp recordings (Figure 2.14). During the investigation of single ion channels or small membrane patches (Figure 2.14 a,b), the glass pipette is brought into contact with the cell membrane and the application of suction enables a tight sealing between cell and pipette. If more suction is applied, the cell membrane breaks down and the glass pipette gains intracellular access to the cell (Figure 2.14 c). While this enables an improved signal amplitude due to the intracellular access, it also results in a mixing of the intracellular fluid and the electrolyte inside the glass pipette and is thus detrimental to the cell. Applying suction and then removing the pipette from the surface of the cell results in the removal of a small membrane patch (Figure 2.14 d), enabling the study of the ion channels inside the patch while modulating their environment through changes in the bath composition.[88] Patch-clamp measurements have *e.g.* been used to study the general behavior of ion channels, their response to toxins, and the electrogenic activity

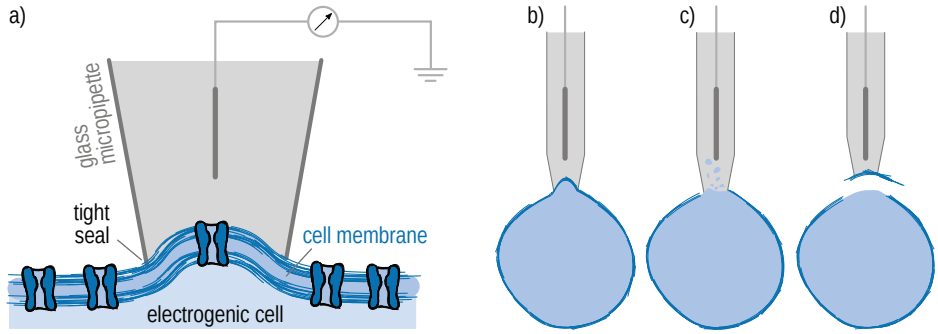

Figure 2.14: Schematic representation of different patch-clamp experiments. In each case, a small diameter glass pipette filled with electrolyte is brought into contact with the cell. (a,b) Cell-attached variation for the investigation of few or single ion channels. By application of suction, a tight sealing between cell and patch-pipette is achieved. In this mode, the cell membrane remains intact. (c) Whole-cell patch-clamp: Increasing the suction through the patch pipette results in the removal of the cell membrane patch and the electrode thus achieves intracellular access. (d) Inside-out variation: A piece of the membrane is removed from the cell, allowing the study of specific ion channels while modulating their environment through the bath composition. Figure adapted from [81,88]

of single neurons. They offer the advantage of a very high **signal-to-noise (S/N) ratio**, thereby enabling even the detection of subthreshold potentials. However, their invasive nature precludes long-term studies such as are needed for the investigation of the establishment of network connectivity or the process of learning. Furthermore, their large size in relation to the cell and the bulky mechanics and electronics needed for their delicate manipulation and signal amplification make it highly challenging to investigate multiple cells at the same time. In order to circumvent these limitations, a different approach is needed. A promising alternative are **microelectrode arrays (MEAs)**. MEAs are extracellular devices that transduce the cellular ionic currents to an electric signal by coupling to the voltage drop inside the gap between cell and electrode. Thereby, they enable the communication of biology and electronics. Figure 2.15 schematically depicts a 64 electrode MEA as employed within this body of work. MEAs offer a multitude of advantages for interfacing with electrogenic cells: Through their multiple interaction sites and non-invasive nature, they enable long-term studies of cellular networks, they provide excellent temporal resolution, and can facilitate a two-way communication, enabling both the recording of cellular signals as well as the stimulation of electrogenic activity. However, two limiting factors for the efficiency of MEA-based systems remain: The **spatial resolution** and **coupling efficiency**. The spatial resolution depends of the number, size, and arrangement of electrodes on the device, with an increase

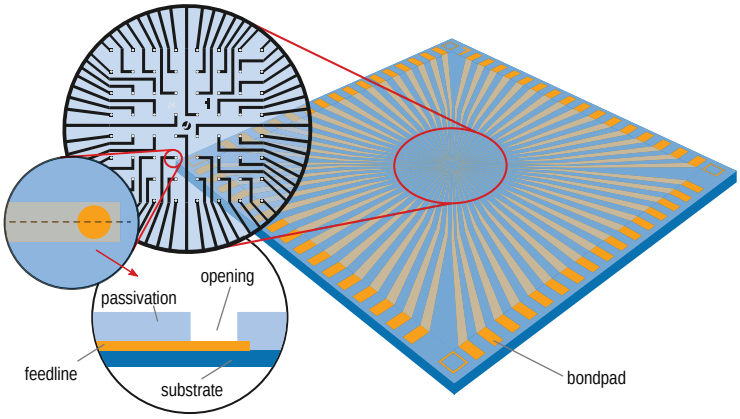

Figure 2.15: Schematic representation of a 64 electrode microelectrode array (MEA). The metallic feedlines are covered by an insulator - the passivation - allowing interaction with the environment only at the circular apertures in the center of the device and the bondpads in the periphery.

in electrode density conceivably resulting in an improved spatial resolution. At the same time, a higher electrode density introduces a new set of problems: The fabrication-based challenge of addressability, and the inherent problem of device impedance, with the smaller size of electrodes needed for an increase in density causing a significant increase in impedance and thus thermal noise. Complementary metal oxide semiconductor (CMOS) based circuitry can resolve the problem of addressability by mapping several electrodes onto a single read-out channel.[16,17] In this manner, Bakkum *et al.*[17] were able to address 11,011 electrodes with just 126 external channels. The issue of device impedance, on the other hand, is more complicated to resolve, with many attempts being made at increasing the surface area while maintaining a small geometric footprint of the electrode, for example with rough or porous metal surfaces,[4,20–28] carbon nanotubes,[29–32] or conducting polymers.[33–36] Many promising results have been reported, though problems such as the stability of the surface, *e.g.* degradation of the high surface area for porous platinum deposits (Pt black) or delamination of polymeric layers, continue to necessitate further investigations into possible solutions. The main focus of this body of work, however, is the improvement of the coupling efficiency. Due to their extracellular position and limited cell-device coupling, planar MEAs record cellular signals with significantly lower amplitude (up to about 1% of the intracellular cellular signal[5]) and signal-to-noise ratio than patch-clamp measurements do. Furthermore, no detection of sub-threshold activity is possible with these devices. Besides the significant atten-

uation of the signal as compared to intracellular recordings using probe-based approaches, the obtained signal shape usually differs considerably, with the signals obtained with MEA-based action potential recordings commonly being the first order derivative of intracellular signals,[40,55,89] with either negative or biphasic peaks as opposed to the positive monophasic peaks expected for intracellular recordings (Figure 2.16).[54] Many approaches towards the improvement of the signal

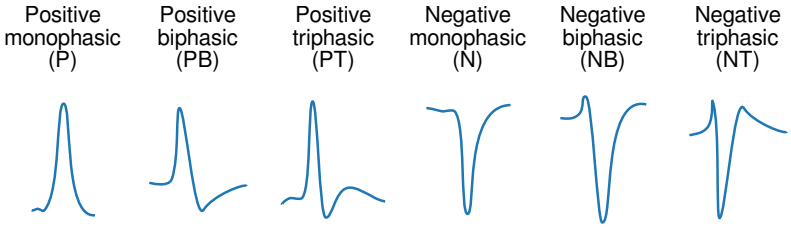

Figure 2.16: AP shapes as observed during planar MEA-based action potential recordings. In the majority of cases, negative (N), negative biphasic (NB) and negative triphasic (NT) signals are observed with occurrence of 61%, 15% and 15%, respectively.[90] Figure adapted from[90]

amplitude obtained from MEA-based recordings have been developed. However, their rationale first necessitate a further discussion of the underlying principles limiting the signal quality of MEA devices.

2.2.5 Point contact model, impedance, and sealing resistance

Figure 2.17[5,91] shows a schematic representation of a neuroelectronic hybrid. Both the cell membrane and the electrode exhibit resistive as well as capacitive characteristics. The electrical characteristics of the electrode are described by the **electrode impedance**, the effective resistance of the electrode in an alternating-current (AC) power circuit. Different circuit components exhibit different impedance characteristics, with the impedance Z_R of a perfect resistor being its resistance and the impedance Z_C of a perfect capacitor being[70]

$$Z_C = \frac{i}{\omega C} \tag{2.25}$$

where i is the imaginary unit with $i^2 = -1$, ω is the angular frequency of the AC signal, and C is the capacitance. Since the capacitance is proportional to the area A, the impedance scales with the size of the electrode, with smaller electrodes resulting in a higher impedance. As an increase in impedance results in an increase in thermal noise during voltage-based recordings,[92,93] smaller

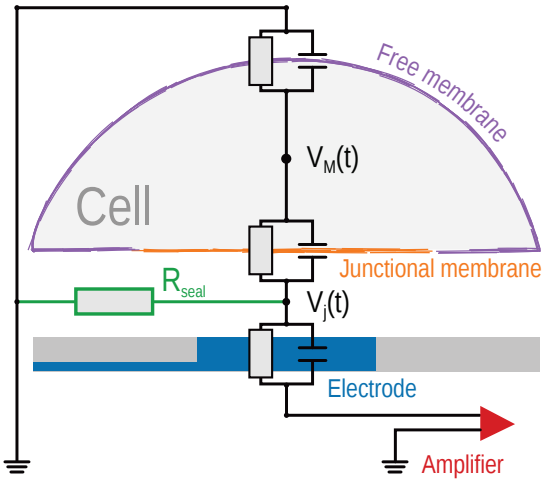

Figure 2.17: The point contact model: Equivalent circuit of a neuroelectronic hybrid. Both cell membrane and electrode have resistive and capacitive characteristics. The cell establishes a membrane potential V_M, which can be detected extracellularly at the cell-electrode junction (V_j). The resistance of the cleft between cell and electrode is termed sealing resistance R_{seal}, and is highly important for the efficiency of the cell-device coupling. Figure adapted from [5,11,91]

electrodes exhibit higher noise and thus smaller S/N. Apart from these electrical characteristics, the most important parameter affecting the efficiency of the cell-device coupling is the **sealing resistance R_{seal}**, which is the resistance of the cleft between cell and electrode.[5] If the sealing resistance is low, the ionic currents occurring inside the cleft during an action potential will merely generate a small voltage difference between the cell-electrode junction and the bulk solution. The values obtained for R_{seal} during patch-clamp recordings are up to 1 GΩ,[5] while R_{seal} for MEA-based action potential recordings is usually in the range of 100 kΩ up to 1 MΩ.[5] This is due to the significantly larger gap between cell and device surface of between 40 nm and 150 nm, as compared to the direct contact established with patch-clamp electrodes.[5,38,94] According to the literature, R_{seal} depends both on the distance between cell and electrode ($d_{cell\text{-}electrode}$), the coverage of the electrode by the cell ($A_{cell\text{-}electrode}/A_{electrode}$), and the resistance of the electrolyte ($\rho_{electrolyte}$) inside the cleft[39,56,95–97]

$$R_{seal} \mid \rho_{electrolyte} \pm \frac{1}{d_{cell\text{-}electrode}} \pm \frac{A_{cell\text{-}electrode}}{A_{electrode}} \tag{2.26}$$

While this is a simplified representation of the influential factors, it does suffice to highlight major aspects affecting the sealing resistance. These influences result in a significantly reduced coupling coefficient C_c

$$C_c = \frac{V_{recorded}}{V_{generated}} \tag{2.27}$$

for MEA-based measurements of around $C_{c,MEA} = 0.001\text{-}0.01$[5] as compared to patch-clamp recordings with $C_{c,patch\text{-}clamp} = 1$.[5] Usually, the coupling coefficient increases with higher R_{seal}, is inversely proportional to the resistance of the junctional membrane, and depends on the geometry of the cell-electrode contact,[56] with a larger contact area resulting in a smaller junctional membrane resistance due to a larger presence of ion channels.[54] The dependence of the signal at the cell-electrode interface V_j on the characteristics of the cell-electrode contact and the electrical characteristics of the junctional membrane can be further described by the equation reported by Regehr *et al.*[11]

$$\begin{aligned} V_j &= \left(i_c + \sum_{channel=1}^{n} i_{channel} \right) \cdot R_{seal} \\ &= \left(C_m \frac{dV_M}{dt} + \sum_{channel=1}^{n} \frac{V_M - V_{channel}}{R_{channel}} \right) \cdot R_{seal} \end{aligned} \tag{2.28}$$

where i_c is the current flowing due to the membrane capacitance, $i_{channel}$ is the current flowing through each channel n, $V_{channel}$ is its electrochemical driving force, $R_{channel}$ its resistance, V_M the membrane potential, and C_m the membrane capacitance.[11] The amplitude and shape of extracellular recordings thus depend on R_{seal} and the current that flows across it.[5] For MEAs, the coupling occurs mostly capacitively,[98] which results both in an area dependence and a high dependency of the extracellular signal on the rise- and decay times of the intracellular signal.[89] For fast action potentials, dV/dt is large, the capacitive current predominant over the ionic current and the extracellular signal thus is the first order derivative of the intracellular signal. Slow action potentials can result in various waveforms.[99]

Due to the direct dependency of V_j on R_{seal}, a central goal for the improvement of the cell-device coupling for MEAs is thus increasing the sealing resistance by facilitating a closer contact between cell and electrode. Recently, Wijdenes *et al.*[41] reported a nano-edge microelectrode, a planar microelectrode exhibiting a protruding edge around the perimeter of the electrode. In this manner, they were able to record high-amplitude action potentials of around 10 mV peak-to-peak (p2p) from neurons from the mollusk *Lymnaea*, which were stable for at least two weeks. However, since their electrode is relatively large at 30 µm diameter, this approach is not applicable for smaller vertebrate neurons since the low spatial resolution precludes single-cell resolution. Another approach is the introduction of recessed nanocavities via the back-etching of a sacrificial electrode layer beneath the passivation.[42–45] This approach exhibits various advantages: The

increased surface area greatly reduces the device impedance while maintaining a small overall geometrical footprint of the interaction site and thus high spatial resolution by use of a small aperture in the passivation.[45] Furthermore, cellular protrusion into the sensor area facilitates an improvement of the sealing resistance and thus coupling efficiency, yielding action potential recordings of up to 3 mV_{p2p} for cardiomyocyte-like HL-1 cells.[44] Within this body of work, a different approach is investigated, aiming to improve the cell-device coupling by introduction of three-dimensional electrode designs.

2.2.6 The 3D approach

Since their first report in the literature by Spira *et al.* in 2007,[46] 3D electrodes have been the focus of extensive research as possible solution for the problem of low sealing resistance. Spira observed the formation of a very tight cell-electrode contact by application of mushroom-shaped 3D structures, with *Aplysia californica* neurons and human cardiomyocytes[46] as well as various cell lines[47] readily engulfing mushroom-shaped gold spines of 850 nm stalk width, 1 µm stalk height, 1.8 µm cap width and 1.6 µm total height. For *Aplysia* neurons, the cell-electrode gap was determined to be around 35∼21 nm around the spine in contrast to 56∼29 nm on flat surfaces.[47] First electrophysiological investigations employing this system were conducted in 2009, with a set of four mushroom-shaped electrodes yielding a 4.5 times increase in signal amplitude as compared to planar MEAs, while maintaining the normal electrophysiological behavior of the cells.[47] Later reports by the same group described action potential recordings with amplitudes of up to 25 mV_{p2p} from *Aplysia* neurons, with signal shapes similar to the positive monophasic action potentials recorded intracellularly, resulting in the introduction of the term 'In-Cell' recording. First successful recordings from vertebrate neurons were conducted by Fendyur *et al.* in 2011,[90] who recorded action potentials from rat hippocampal neurons with amplitudes of up to 0.75 mV_{p2p}. Additionally, in contrast to the negative peaks recorded with planar MEAs, the signal shape obtained employing these structures was primarily (>80%) of the P, PB or PT category (see Figure 2.16).[54,90] Recently, Shmoel *et al.*[54] reported action potentials of up to 5 mV_{p2p} for embryonic rat hippocampal neurons, which is equivalent to a coupling coefficient of approximately $C_c = 0.05$. Plain nanopillars have also been reported to improve the cell-electrode contact, with Hanson *et al.*[100] achieving gap distances that were on average below 15 nm on nanopillars of 200 nm in diameter and 1 µm height and thus much less than on the surrounding flat areas. However, the introduction of a mushroom

cap was shown to facilitate a closer cell-electrode contact as compared to plain pillars.[49] The mechanism proposed as reason for the improved contact induced by mushroom-shaped structures is two-fold: On the one hand, Hai *et al.* suggest an **increase in the junctional conductance**, which they attribute to a cytoskeletal rearrangement induced by the convex surface, as well as an activation of ion channels due to the mechanical tension imposed on the cell due to the 3D geometry.[55] On the other hand, it was proposed that the 3D structure induces the cellular mechanism of **phagocytosis**, which is the process through which cells internalize large objects, up to a size of approximately 0.5 µm.[46] During this process, the cell membrane first attaches to and then wraps around the target. Afterwards, actin is arranged around the formed compartment, pinching it off from the membrane. Applying the same process to a surface-attached 3D structure will prevent the last step and thus full internalization of the target. The formed actin ring is expected to stabilize the contact and result in good sealing (Figure 2.18).[90,101] However, while *e.g.* microglia,

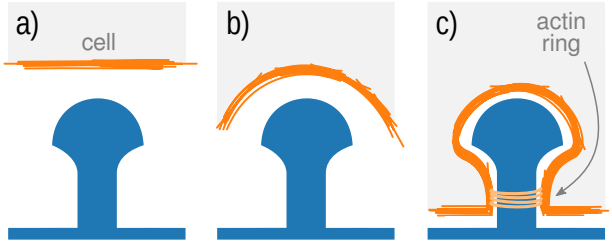

Figure 2.18: Phagocytosis-like mechanism for the establishment of a tight contact between cell and electrode. The cell approaches (a) and then wraps around the 3D structure (b,c). The formation of an actin ring around the foot of the structure results in a stable contact (c). Figure adapted from[46,47]

the macrophages of the nervous system, are known to phagocytose apoptotic cells or cellular debris,[102] neurons are not generally thought to be phagocytotic, despite a report by Bowen *et al.*[103] suggesting that the neuronal capability for the uptake of large objects is more extended than previously thought. In later publications detailing the interaction of neurons with 3D structures, the term 'phagocytosis' is therefore exchanged for **'engulfment'**. Several studies have tried to elucidate the geometrical requirements for a tight engulfment of 3D structures, reporting a strong dependency on the shape and aspect ratio of the structures,[49] with mushroom-shaped structures of higher aspect ratio resulting in significantly improved engulfment as compared to plain pillars or mushrooms of lower aspect ratio. Nevertheless, the exact mechanism that facilitates the considerable improvement in coupling efficiency remains controversial.

Figure 2.19 depicts different three-dimensional electrode designs. While both solid pillars (Figure 2.19 a) and solid mushrooms (Figure 2.19 b) have been copiously studied, the efficiency of

'1D' nanostraws (Figure 2.19 c) for a spontaneous impalement of the cell is still under debate. Melosh *et al.* have conducted extensive research on nanowires as delivery platform for nanobiotech-

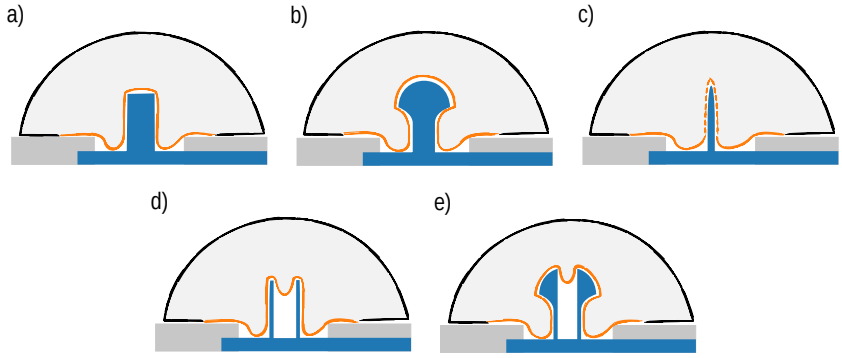

Figure 2.19: Schematic cross-sections of different 3D geometries and expected junctional membrane shapes as reported in the literature: (a) solid pillar,[49] (b) solid mushroom,[46,104] (c) nanostraw,[53] (d) hollow pillar,[50] (e) target structure for this body of work: hollow mushroom, envisioned as combination of (b) and (d).

nology.[57,105] They found that for nanowires of 100 nm in diameter and 1 µm in height, about 7% spontaneously penetrated the cell.[57] Furthermore, they could show that the efficiency of penetration is highly dependent on the structure size, with 100 nm diameter structures being able to spontaneously penetrate the cell membrane, while 250 nm structures maintain their extracellular position.[51] Apart from the characteristics of the nanostructure itself, the mechanics of the cell also play a crucial role, with stiffer cells showing a higher penetration efficiency but also a higher dependency on the geometry of the structure.[52] To date, reports on the efficiency of this approach for electrophysiological studies, however, have been scarce. Robinson *et al.* reported a 50% penetration efficiency on human embryonic kidney cells (HEK 293) cells using nanowires of 150 nm in diameter and 3 µm in height, as well as positive monophasic action potential recordings from rat cortical neurons after stimulation with a patch pipette.[53] Dipalo *et al.*[106] recorded spontaneous action potentials from rat hippocampal neurons employing nanoantennas of 160 nm in diameter and 2 µm in height with adequate S/N ratio, however, the recorded amplitude was in the 100 µV range and thus far below the coupling efficiency needed for the recording of subthreshold activity, suggesting that the structures maintain their extracellular position. Recently, Liu *et al.*[58] reported unprecedented recording quality of up to 99 mV_{p2p} for mouse hippocampal neurons on vertical nanowires of 200 nm in diameter and 6.5 µm in height, which is in the range of signal amplitudes

achieved with patch-clamp recordings. However, the range of potentials recorded as part of this study was reported as 0.1 to 99 mV_{p2p}, highlighting the large variability of signal amplitudes obtained with this method. Overall, the scientific community remains skeptical of the efficiency of the impalement approach as well as the criteria facilitating spontaneous penetration. The low penetration probability, which can befittingly be classified as 'serendipitous surface adhesion',[62] the limitation to very small structures and resulting high impedance of the devices, and the cell dependence all necessitate more empirical evidence to prove the applicability of this approach for electrophysiological studies. Another question is the dependence of the cellular behavior on high aspect ratio structures, with some papers reporting little influence on cell viability and gene expression,[51] while others report significant alteration of cell behavior including morphology, motility, and proliferation.[107,108] Little can be found with respect to the efficiency of hollow nanopillars (Figure 2.19 d), though the available report by Lin *et al.*[50] is very promising. They reported significantly higher action potential recordings for hollow iridium oxide (IrOx) structures as compared to solid gold pillars. The employed structures were 180 nm in outer diameter, 500 nm in height, and exhibited sidewalls of 40 nm thickness. They attributed the differences in recording capability not only to differences in material, but also to the tendency of cells to protrude into openings as small as 100 nm in diameter, generating a positive curvature that could be advantageous for the coupling efficiency.[50] The structure in Figure 2.19 (e) has been developed as part of this body of work, aiming to marry the advantages of mushroom-shaped structures (Figure 2.19 b) and their engulfment-inducing capacities, with the cellular protrusion into hollow structures (Figure 2.19 d).

2.2.7 Electroporation and membrane insertion

Despite encouraging progress in the field of 3D electrodes, many scientists still argue that a purely geometric induction of a closer cell-electrode contact is not sufficient to achieve the coupling efficiency needed to record sub-threshold activity.[59] One approach to improve the coupling is the reduction of the junctional membrane resistance via the introduction of transient pores through a process called **electroporation**.[109] Electroporation is a method widely used in biology for the transfection of cells and bacteria. A high-voltage pulse results in the dielectric breakdown of the membrane and the formation of pores[110] (Figure 2.20). Higher amplitude pulses result in pore formation in a larger area, while longer pulses result in a higher degree of permeabilization.[110] If the amplitude of the pulse is small enough, the pores reseal within the range of several min-

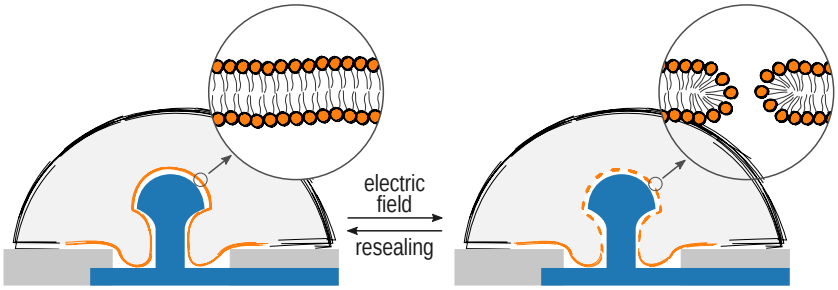

Figure 2.20: Schematic representation of electroporation on 3D electrodes. Upon application of a sufficient electric field, the membrane experiences dielectric breakdown, resulting in the formation of transient pores. Figure adapted from[109]

utes.[110] For very high pulses, however, the damage is too severe and results in cell death. While the voltage necessary for efficient electroporation is very high in macro-plate electroporation systems as employed for the delivery of cargo into cells (0.5-100 kV/cm),[111] 3D electrodes exhibit an enhanced electric field and can thus perform electroporation at reduced voltages as compared to planar electrodes.[111] This was also observed by various groups employing 3D structures for the electroporation of a number of different cell types, with potentials below 3.5 V usually sufficient to facilitate pore formation.[50,98,109] The application of a low potential is important to prevent unfavorable effects such as electrode degradation, heating, and bubble formation due to the electrolysis of water,[111] all of which have adverse effects on cell viability and device stability. Electroporation using 3D mushroom-shaped electrodes has been employed on *Aplysia* neurons,[112] embryonic rat cardiomyocytes,[109] and rat skeletal myotubes.[89] In all cases, the application of a voltage pulse results in a significant initial increase in signal amplitude, followed by an amplitudal decay over the time course of 10 to 30 min due to the resealing of the transient pores without detrimental effect on the studied cells. Similar results were obtained by Xie *et al.*[98] employing Pt nanopillars of 1.5 µm height and 150 nm in diameter. In contrast, Lin *et al.*[50] reported a significantly prolonged intracellular access employing hollow iridium oxide pillars as compared to solid gold pillars, with up to an order of magnitude longer intracellular access after electroporation pulses employed via hollow IrOx structures. This approach struggles with three main challenges though: Firstly, pore formation is transient and can thus not be employed to achieve long-term stable, high-amplitude signals. Secondly, the effective field experienced by the cell depends - just like the electrode-detected signal does - on the coupling between cell and electrode, making the establishment of

universal parameters challenging. And lastly, the application of excessive pulses results in cell death and is thus highly undesirable. Melosh *et al.* reported a different approach to facilitate long-term intracellular access (Figure 2.21). They prepared 3D structures exhibiting a thin band of gold in

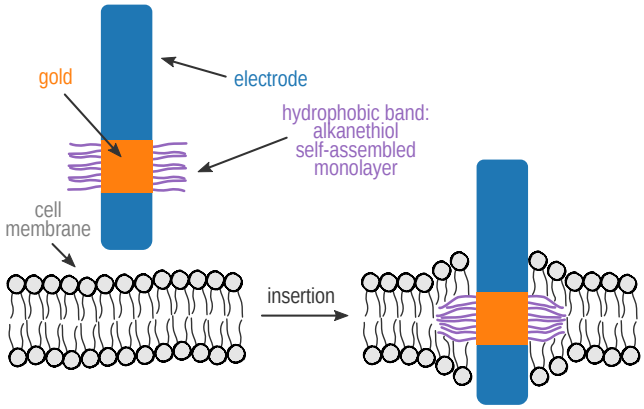

Figure 2.21: Schematic representation of the membrane insertion concept: A thin band of gold (5-10 nm) is introduced to the probe and functionalized with alkanethiols. The hydrophobic alkane chains are incorporated into the lipid bilayer upon insertion of the probe, stabilizing the configuration and providing good sealing between cell and probe. Figure adapted from [61]

the range of 5-10 nm, which they then functionalized with a self-assembled monolayer of alkanethiols, aiming to mimic the structure of transmembrane proteins. [60] Upon insertion into the cell membrane, this hydrophobic band intercalates into the lipid bilayer. They could show that thinner hydrophobic bands in the range of the thickness of the hydrophobic membrane core result in a stronger adhesion force, as did the usage of shorter alkane chains which exhibit more fluid-like rather than crystalline characteristics. [61,113] In this manner, they were able to form a very tight seal to red blood cells in the GΩ range. [62] Figure 2.21 depicts the concept of these membrane-insertion rings or stealth probes. While this approach is promising for the establishment of a tight seal with 3D electrodes, electrophysiological data proving their applicability for this goal are still missing.

Chapter 3

3D Structure design

As has been stated before, the interaction of cells with 3D electrodes is highly dependent on the geometry of the structure, with shape, size, and aspect ratio highly influencing the behavior of the cell.[49] However, while many different electrode designs have been reported in the literature, little is reported on the **direct comparison** of the influence of different 3D structures with respect to the cell interaction. If this is to be possible, different structures have to be made accessible in a way that enables a parallel production on a single chip. A vast variety of different approaches for the fabrication of 3D structures has been presented in the literature to date, *e.g.* employing reactive ion etching,[53] focused ion-beam milling,[114,115] as well as various templated approaches, for example using electron-beam structured polymers,[46] membranes,[51] or anodized alumina[21] as framework for the fabrication of three-dimensional designs. Within this body of work, electron-beam lithography is employed in conjunction with electrodeposition, which enables an easy adjustment of the structure design and a bottom-up, parallel, controlled deposition process. This Chapter focuses on the development of appropriate parameters for the preparation of the various three-dimensional electrode designs reported in the literature within a common fabrication scheme. Furthermore, it is concerned with the interaction of both cardiomyocyte-like HL-1 cells as well as primary embryonic rat cortical neurons with said 3D structures.

Excerpts of this Chapter have been published in Nanotechnology, Volume 28, Number 9 (2017), S. Weidlich *et al.* 'MEAs and 3D nanoelectrodes: electrodeposition as tool for a precisely controlled nanofabrication'.[116]

3.1 Materials and Methods

3.1.1 3D electrode fabrication

All samples were produced in an ISO 1 cleanroom[117] on n-doped silicon wafers (Si-Mat Silicon Materials, Kaufering, Germany) modified with either 5 nm Ti and 50 nm Au or 10 nm Ti and 100 nm Au via electron-beam evaporation (Pfeiffer PLS 570, Pfeiffer Vacuum, Asslar, Germany). The wafers were cut into 15x15 mm^2 samples, subsequently cleaned in acetone and isopropanol for 5 min under ultrasonication, and dried in a stream of nitrogen. They were dehydrated at 200°C for 30 min, followed by spincoating of poly(methyl methacrylate) (PMMA) (AR-P 669.07, Allresist, Strausberg, Germany) at 500 rpm with an acceleration of 100 rpm/s for 5 s immediately followed by 2000 rpm with an acceleration of 500 rpm/s for 35 s. The samples were then tempered on a 120°C, 180°C, and 120°C hotplate for 2, 5, and 2 min, respectively. Different structures were transferred into the PMMA employing a Vistec EBPG 5000plus HS (Vistec Electron Beam GmbH, Jena, Germany) electron-beam lithography system.

1. **Solid structures:** Circles of 300 nm in diameter arranged in a square grid of 25 µm spacing were written with a dosis of 402.5 $\mu C/cm^2$. Circles of 600 nm and 800 nm in diameter arranged in a square grid of 25 µm spacing were written with a dosis of 350 $\mu C/cm^2$. All structures were written with a resolution of 2 nm, beam current of 500 pA, automatic sequencing, and without proximity correction.

2. **Determination of optimal dosis for hollow structures:** Hollow structures with diameters of 300, 600, and 800 nm and ring thicknesses of 25, 50, 100, and 150 nm arranged in a square grid of 25 µm spacing were written with a dosis series starting from 400 $\mu C/cm^2$ up to 2028 $\mu C/cm^2$ with a factor of 1.07 from one dosis to the next. The structures were written without proximity correction at a resolution of 2 nm, a beam current of 100 pA, and automatic sequencing.

3. **Hollow structures:** Rings of 600 nm in outer diameter and 25 nm ring thickness arranged in a square grid of 25 µm spacing were written with a dosis of 1400 $\mu C/cm^2$. Rings of 800 nm in outer diameter and 25 nm ring thickness arranged in a square grid of 25 µm spacing were

written with a dosis of 1400 µC/cm^2. All structures were written with a resolution of 2 nm, beam current of 100 pA, automatic sequencing, and without proximity correction.

4. **Big hollow structures:** Rings of 1 µm in outer diameter and 25 nm ring thickness were written with a dosis of 1400 µC/cm^2, rings of 2 µm in outer diameter and 50 nm ring thickness with a dosis of 750 µC/cm^2, and rings of 3 µm in outer diameter and 50 nm ring thickness with a dosis of 750 µC/cm^2. All structures up to a size of 3 µm were written with a beam current of 100 pA. Rings of 4 µm in outer diameter and 100 nm ring thickness were written with a dosis of 550 µC/cm^2, rings of 5 µm in outer diameter and 100 nm ring thickness with a dosis of 550 µC/cm^2, and rings of 7.5 µm in outer diameter and 150 nm ring thickness with a dosis of 500 µC/cm^2. Structures in the range between 4 µm and 7.5 µm were written with a beam current of 200 pA. All structures were arranged in a square grid of 50 µm spacing, were written with a resolution of 2 nm, automatic sequencing, and without proximity correction.

Development of the structures was performed by immersion into AR 600-55 (Allresist, Strausberg, Germany) for 220 s at room temperature, followed by immersion into isopropanol and deionized water for 1 min each. The samples were dried in a stream of nitrogen. Glass rings (14 mm outer diameter, 1 mm wall thickness, 10 mm height) were glued onto each sample using a two-component epoxy resin (EPO-TEK 302-3M 8OZ Kit, Epoxy Technology, Billerica, USA) and cured at 65°C for 3 h. They were then placed into a custom-made sample holder (see Figure 3.1) and 700 µl gold bath solution (Pur-A-Gold 202B, Enthone, Langenfeld, Germany containing 12 g/l Au from $KAuCN_2$ (99.9% metal basis, Alfa Aesar, Karlsruhe, Germany)) were filled into the ring and pipetted up and down at least 15 times to ensure penetration into the template. Electrodeposition was performed on a Biologic VSP-300 (Bio-Logic SAS, Claix, France) potentiostat using a three-electrode configuration with the MEA electrodes as working, a Pt mesh as counter, and a Ag/AgCl pellet as reference electrode. In early experiments, the current was recorded with a 20 Hz sampling rate and a 50 kHz low-pass filter. Later, the current was recorded with a 4 Hz sampling rate and a 5 Hz low-pass filter. Electrodeposition was either performed at -1.00 V, -1.05 V, -1.10 V, -1.15 V, -1.20 V, -1.25 V or employing a two-step process; In this case, a potential of either -1.25 V or -1.35 V versus reference was applied for 5 s, followed by -1.10 V for various times to prepare structures of different sizes. After electrodeposition, the gold bath solution was removed, the samples washed with ultrapure water thrice and placed into acetone for PMMA removal. The acetone was exchanged twice to

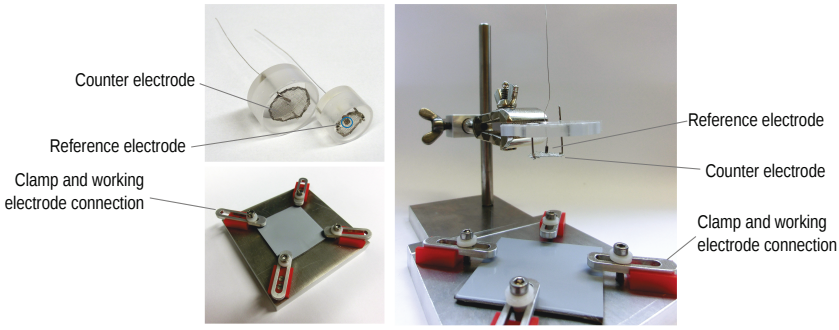

Figure 3.1: Custom-built sample holder as used for the deposition of large-area 3D structures. The left side depicts the first design as employed in early experiments, with a lid made of acrylic glass containing counter and reference electrode being placed over the glass ring employed as reservoir for the gold bath. The right side depicts the final design, with the counter and reference electrode fixed as free-standing structures in acrylic glass and merely being lowered into the plating bath. The position of the reference electrode in respect to working and counter electrode was fixed according to the concepts presented by Zhang *et al.* [118]

ensure full removal. The samples were dried in a stream of nitrogen and imaged at a LEO 1550 (Carl Zeiss AG, Oberkochen, Germany) scanning electron microscope at 20 kV acceleration voltage using inlens detection.

3.1.2 HL-1 CULTURE

3D structure-containing samples were consecutively cleaned in acetone and isopropanol (Merck KGaA, Darmstadt, Germany) for at least 15 minutes, each, and dried in a stream of nitrogen. They were sterilized by incubation with 70% ethanol, transferred to a sterile hood, and rinsed with sterile, ultrapure water thrice. They were coated with 5 µg/ml fibronectin from bovine plasma (Sigma-Aldrich, Schnelldorf, Germany) in 0.02 % gelatin from porcine skin (Sigma-Aldrich, Schnelldorf, Germany) (FibGel) for one to two hours at RT. They were washed with medium once, right before cell seeding. Cardiomyocyte-like HL-1 cells were maintained in T-25 culture flasks in Claycomb medium (Sigma-Aldrich, Steinheim, Germany) supplemented with 10 vol% fetal bovine serum (FBS) (Life Technologies GmbH, Darmstadt, Germany), 100 µg/ml penicillin-streptomycin (Life Technologies GmbH, Darmstadt, Germany), 0.1 mM (±)-norepinephrine (+)-bitartrate salt (Noradrenaline) (Sigma-Aldrich, Steinheim, Germany) and 2 mM L-glutamine (Life Technologies GmbH, Darmstadt, Germany) in a humidified incubator at 37°C and 5% CO_2. The medium was exchanged for 5 ml fresh, pre-warmed, supplemented Claycomb medium daily. Once confluency was reached and

mechanical contraction was visible, adherent HL-1 cells were washed with 0.05% trypsin-EDTA (1 ml) (Life Technologies GmbH, Darmstadt, Germany) once and detached by incubation with 0.05% trypsin-EDTA (1 ml) at 37°C for 3 to 5 min. Trypsin digestion was then inhibited by addition of supplemented Claycomb medium (5 ml) and the cells were sedimented by centrifugation at 500 rcf (relative centrifugal force) for 5 min. The supernatant was aspirated, the cells resuspended in prewarmed, supplemented Claycomb medium (1-4 ml), seeded onto the samples at appropriate densities and topped-up with supplemented Claycomb medium. The media was exchanged daily until cell fixation.

3.1.3 Neuronal culture

3.1.3.1 Sample cleaning Planar samples (n-doped silicon, 5 nm Ti, 50 nm Au, 15x15 mm^2) were successively cleaned in acetone (Merck KGaA, Darmstadt, Germany) and isopropanol (Merck KGaA, Darmstadt, Germany) under ultrasonication for 10 minutes, each. 3D structure-containing samples were incubated with acetone and isopropanol for 10 minutes, each. Prior to plasma cleaning, the plasma oven (Pico low-pressure plasma system, Diener electronic, Bielefeld, Germany) was purged of organic residues using O_2 plasma at 0.2 mbar and 200 W for 10 min. Afterwards, the samples were cleaned with O_2 plasma at 0.4 mbar and 200 W for 10 min.

3.1.3.2 Coating establishment Unmodified gold-on-silicon samples (n-doped silicon, 5 nm Ti, 50 nm Au, 15x15 mm^2) were cleaned according to the procedure described in 3.1.3.1. They were then either directly placed into ethanol and transferred to a sterile hood, or functionalized with a self-assembled monolayer by incubation with 5 mM 11-mercapto-1-undecanol (Sigma-Aldrich, Schnelldorf, Germany) in ethanol (Merck KGaA, Darmstadt, Germany) for 4h and subsequent washing with ethanol five times. After transfer to a sterile hood, each sample was placed into a well of a 12-well dish and incubated with 70% ethanol for 10 min, followed by rinsing with ultrapure water thrice. Coverslips were used as control; they were sterilized over an open flame and placed into a 12-well dish. Afterwards, different protein coatings were incubated on the samples, consisting of either 10 µg/ml poly-L-lysine hydrobromide (PLL) (Sigma-Aldrich, Steinheim, Germany) in different buffers, 125 µg/ml Avidin (Life Technologies GmbH, Darmstadt, Germany) in 20 mM N-2-hydroxyethyl piperazine-N'-2-ethane sulphonic acid (HEPES, pH 7.5) (Carl Roth GmbH + Co. KG, Karlsruhe, Germany) or a mixture of 31.25 µg/ml Avidin and 7.5 µg/ml PLL in 20 mM HEPES.

Each coating solution was left to incubate on the samples for 1 h at RT and then washed with the respective buffer twice. The solution was then aspirated so as to dry the samples completely. The multiwell dishes were wrapped in parafilm and stored in the fridge over night. Table 3.1 provides an overview over the different substrate/coating combinations studied within this body of work.

Table 3.1: Overview over different substrate/coating and employed buffer combinations investigated as part of this study

Substrate	Thiol modification	Coating protein	Buffer
Au	No	PLL	Ultrapure water
		PLL	Hank's balanced salt solution
		PLL	20 mM HEPES
		Avidin	20 mM HEPES
		Avidin/PLL	20 mM HEPES
Au	Yes	PLL	20 mM HEPES
		Avidin	20 mM HEPES
		Avidin/PLL	20 mM HEPES
Glass	No	PLL	20 mM HEPES
		Avidin	20 mM HEPES
		Avidin/PLL	20 mM HEPES

Cortices were isolated from E18 wistar rats (animal testing approval: Landesumweltamt für Natur, Umwelt und Verbraucherschutz Nordrhein-Westfalen, Recklinghausen, Germany, record number 84-02.04.2015.A173) and dissociated into individual cells by incubation with 0.05% Trypsin-EDTA (Life Technologies GmbH, Darmstadt, Germany) at 37°C, 5% CO_2, and 95% humidity for 15 min. The tissue was gently moved after 5 and 10 min. The tissue was then transferred to a 2 ml Eppendorf tube, the supernatant removed and the tissue carefully washed with cold, Neurobasal medium (Life Technologies GmbH, Darmstadt, Germany) supplemented with 1% B-27 supplement (Life Technologies GmbH, Darmstadt, Germany), 50 µg/ml gentamicin solution (Sigma-Aldrich, Steinheim, Germany) and 0.5 mM L-glutamine (Life Technologies GmbH, Darmstadt, Germany) thrice. Between washing steps, the tissue was allowed to settle at the bottom of the tube before removal of the supernatant. After the last washing step, the supernatant was removed in full, 1 ml supplemented Neurobasal medium was added, and the tissue was trituated. Undissociated tissue pieces were allowed to settle for 2 min. Afterwards, the upper 900 µl were transferred to a new Eppendorf vial. Cells were counted using a Neubauer improved cell counting chamber and 80 k cortical neurons

in 1.5 ml supplemented Neurobasal medium were seeded onto each sample. One to two hours after seeding, the medium was exchanged against fresh, pre-warmed, supplemented Neurobasal medium in two steps of 750 µl each to prevent drying of the samples. The cells were maintained in a humidified incubator at 37°C and 5% CO_2. Half the media was exchanged against fresh, pre-warmed, supplemented Neurobasal medium every three to four days. Live/dead staining was performed after 3, 7 and 14 days *in vitro* (DIV), at which time the samples were incubated with a 1:1:1000 solution of calcein-AM (→1 mM in DMSO) (Life Technologies GmbH, Darmstadt, Germany) and ethidium homodimer-1 (2 mM in DMSO) (Sigma-Aldrich, Schnelldorf, Germany) in warm, supplemented Neurobasal medium at 37°C, 5% CO_2, and 95% humidity for 15 min. Afterwards, the samples were transferred to fresh, warm, supplemented Neurobasal medium and imaged at a ZEISS Axio Imager Z1 (Carl Zeiss AG, Oberkochen, Germany).

3.1.3.3 Neuronal culture on 3D structures After sample cleaning, the samples were incubated with 5 mM 11-mercapto-1-undecanol (Sigma-Aldrich, Schnelldorf, Germany) in ethanol (Merck KGaA, Darmstadt, Germany) for 4 h and subsequently washed with ethanol five times. They were transferred into a sterile hood and placed into the wells of a 12-well dish containing 70% ethanol. After incubation for 10 min, the samples were washed with ultrapure water thrice, followed by incubation with a mixture of 31.25 µg/ml Avidin (Life Technologies GmbH, Darmstadt, Germany) and 7.5 µg/ml PLL (Sigma-Aldrich, Steinheim, Germany) in 20 mM HEPES (pH 7.5) (Carl Roth GmbH + Co. KG, Karlsruhe, Germany) in ultrapure water for 1 h at RT. Afterwards, the samples were washed with 20 mM HEPES twice. The solution was aspirated so as to dry the samples completely. The multiwell dishes were wrapped in parafilm and stored in the fridge over night. Cortices were isolated and dissociated as described in 3.1.3.2 and cortical neurons seeded onto all samples at the desired cell density (60 k-400 k) in 1.5 ml supplemented Neurobasal medium per well of the 12-well dish. One to two hours after seeding, the medium was exchanged against fresh, pre-warmed, supplemented Neurobasal medium in two steps of 750 µl each to prevent drying of the samples. The cells were maintained in a humidified incubator at 37°C and 5% CO_2. Fixation was performed at 3 DIV.

3.1.4 Fixation and imaging

3.1.4.1 Critical point drying The samples were washed with warm phosphate buffered saline (PBS) thrice. Chemical fixation was performed employing a warm solution of 3.2% glutaraldehyde (Sigma-

Aldrich, Schnelldorf, Germany) in PBS for 15 min. After washing with PBS twice, the samples were washed with ultrapure water five times. Afterwards, a solvent exchange from water to ethanol was performed by incubation with 10%, 30%, and 50% ethanol (Merck KGaA, Darmstadt, Germany) in ultrapure water for 5 min each, followed by 70% ethanol in ultrapure water for 15 min, 90% ethanol in ultrapure water for 5 min thrice, and 95% ethanol in ultrapure water for 5 min thrice. Afterwards, the samples were transferred into 100% ethanol. The samples were then dried via critical point drying (CPD). The ethanol was slowly exchanged against liquid CO_2, which was then heated to the critical point. The samples were glued to sample holders with silver glue and allowed to dry. They were then sputtered with iridium.

3.1.4.2 Resin embedding The samples were washed with warm PBS or warm cacodylate buffer (pH 7.4, 0.1 mol/l) (Morphisto GmbH, Frankfurt am Main, Germany) thrice. Chemical fixation was performed employing a warm solution of 3.2% glutaraldehyde (Sigma-Aldrich, Schnelldorf, Germany) in PBS or cacodylate buffer for either 15 min (HL-1) or 30 min (HL-1, neurons). After washing with PBS/cacodylate buffer twice, the samples were washed with ultrapure water thrice. Afterwards, samples were either immediately dehydrated through an ethanol concentration series (see below) or incubated with osmium tetroxide, tannic acid, and uranyl acetate to facilitate a staining of biological membranes and thus contrast within the biological tissue during electron microscopy studies. The samples were incubated with 1% OsO_4 (Sigma Aldrich, Schnelldorf, Germany) in cacodylate buffer for 2 h on ice. They were then rinsed with ultrapure water five times for 2 min each and incubated with 1% tannic acid (Electron Microscopy Sciences, Hatfield, USA) in ultrapure water for 30 min at RT before being again rinsed with ultrapure water five times for 2 min each. After incubation with 2% uranyl acetate (Electron Microscopy Sciences, Hatfield, USA) at 4°C for 5 h (neurons) or over night (HL-1), the samples were rinsed with ultrapure water five times for 2 min each. Afterwards, a solvent exchange from water to ethanol was performed by incubation with 10%, 30%, and 50% ethanol (Merck KGaA, Darmstadt, Germany) in ultrapure water for 5 min each, followed by 70% ethanol in ultrapure water for 15 min, 90% ethanol in ultrapure water for 5 min thrice, and 95% ethanol in ultrapure water for 5 min thrice. Afterwards, the samples were transferred into 100% ethanol. For the resin embedding, 12.5 ml epoxy embedding medium Epon 812 (Sigma Aldrich, Schnelldorf, Germany) were mixed with 20 ml epoxy embedding medium hardener DDSA (Sigma Aldrich, Schnelldorf, Germany). Additionally, 17.3 ml Epon 812 were mixed with

15.2 ml epoxy embedding medium hardener MNA (Sigma Aldrich, Schnelldorf, Germany). Finally, 32.5 ml of the Epon 812/DDSA mixture were thoroughly mixed with 32.5 ml of the Epon 812/MNA mixture and 1.3 ml 2,4,6-tris(dimethylaminomethyl)phenol (DMP-30) (Sigma Aldrich, Schnelldorf, Germany) for 1 h. The fixed samples were then treated with a series of increasing epoxy resin concentration, starting with ethanol:resin as 3:1 for 3 h, followed by ethanol:resin as 2:1 for 3 h, ethanol:resin as 1:1 over night, ethanol:resin as 1:2 for 3h, and ethanol:resin as 1:3 for 3 h. All steps were performed at RT, with the sample container wrapped with parafilm to prevent evaporation. Finally, the samples were incubated uncovered with pure resin for 3 h at RT. Excess resin was removed by washing with ethanol. Afterwards, the resin was cured at 60°C over night. The samples were mounted onto scanning electron microscopy (SEM) stubs with silver glue and sputtered with platinum at 15 mA in 0.05 mbar argon atmosphere for 20-45 s.

3.1.4.3 Focused ion-beam sectioning Focused ion-beam (FIB) sectioning was performed employing a HELIOS NanoLab 600i (FEI Deutschland GmbH, Frankfurt, Germany) DualBeam microscope with electron- and ion-beam source at an angle of 52°. A thin layer of platinum was deposited onto the region of interest via electron-beam-induced deposition (EBID) at 3 kV acceleration voltage and a current between 1.4 nA and 11 nA to protect the area during the sectioning process. Afterwards, a thicker platinum layer was deposited via ion-beam-induced deposition (IBID) at an acceleration voltage of 30 kV and a current between 0.23 pA and 2.5 nA. Bulk milling was performed at 30 kV and a current in the range of 0.23 nA to 2.5 nA. Finally, the cross-section was polished at an acceleration voltage of 30 kV and currents between 40 pA and 0.79 nA. All sectioning was performed employing a gallium ion source. SEM imaging was performed at 3 kV and 21 pA using inlens detection for unstained samples, and at 3 kV and 0.69 nA using a backscattered-electron detector for stained samples.

3.1.5 Quartz crystal microbalance

The adsorption behavior of different coating proteins was investigated employing a Q-Sense E4 quartz crystal microbalance with dissipation (QCM-D) (Biolin Scientific, Stockholm, Sweden). The chambers were disassembled and all Teflon parts and O-rings were sonicated in 2% Hellmanex III (Sigma Aldrich, Schnelldorf, Germany) for 15 min, followed by rinsing under flowing water for 5 min and subsequent sonication in ultrapure water for 5 min. They were then dried and reassembled.

Gold chips (QSX 301, LOT-QuantumDesign GmbH, Darmstadt, Germany) were O_2 plasma treated at 100 W and 0.8 mbar for 5 min and then cleaned in a 5:1:1 mixture of ultrapure water, 25% NH_4OH (Sigma Aldrich, Schnelldorf, Germany), and 30% H_2O_2 (Sigma Aldrich, Schnelldorf, Germany) at 75°C for 5 min. After thorough rinsing with ultrapure water, they were dried in a stream of nitrogen and plasma treated at 100 W and 0.8 mbar for 5 min. SiO_2 (QSX 303, LOT-QuantumDesign GmbH, Darmstadt, Germany) sensors were plasma treated at 100 W and 0.8 mbar for 5 min, followed by incubation with 2% sodium dodecyl sulfate (SDS) (Sigma Aldrich, Steinheim, Germany) for 30 min. After thorough rinsing with ultrapure water, they were dried in a stream of nitrogen and plasma treated at 100 W and 0.8 mbar for 5 min. The sensors were placed into the modules and 1 ml of the respective buffer solution was added to all chambers. Both temperature and resonance frequency were allowed to equilibrate for several hours until the frequency shift was below 0.2 Hz in 10 min. The resonance frequencies were determined and the measurement started. Approximately 10 min into the measurement, the buffer was removed so as to not allow for the sensor area to run dry and the analyte was added. Once the frequency had stabilized, all chambers were rinsed with buffer and the frequency was left to stabilize again before stopping the experiment. Table 3.2 gives an overview over the coating proteins investigated.

Table 3.2: Overview over different substrate/coating combinations investigated as part of this study

Sensor	Coating protein	Concentration	Buffer
Au	PLL	10 µg/ml	Hank's balanced salt solution
	PLL	10 µg/ml	20 mM HEPES (pH 7.5)
	PLL	10 µg/ml	Ultrapure water
	Avidin	125 µg/ml	20 mM HEPES (pH 7.5)
	Avidin/PLL	31.25/7.5 µg/ml	20 mM HEPES (pH 7.5)
SiO_2	PLL	10 µg/ml	Hank's balanced salt solution
	PLL	10 µg/ml	Ultrapure water

3.2 Results

3.2.1 Structure design

The fabrication of nanoscale, mushroom-shaped 3D electrodes has already been established in our institute as part of previous work.[119] The process, as developed there, employs electron-

beam lithography to define circular apertures in poly(methyl methacrylate) (PMMA), followed by electrodeposition of gold (Figure 3.2). Deposition of gold up to the boundary of the PMMA template yields pillars, deposition beyond the boundary of the template yields mushroom-shaped structures.

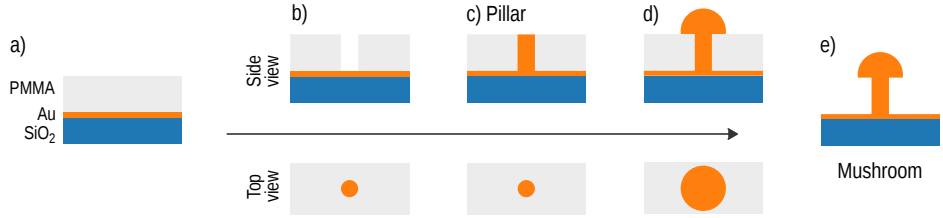

Figure 3.2: Fabrication concept: PMMA is spincoated onto a gold-on-silicon sample ((a) exemplary single structure). (b) Circles are defined via electron-beam lithography. Afterwards, electrodeposition of gold up to the boundary of the PMMA template produces solid pillars (c), while continued deposition beyond the boundary of the template yields solid mushrooms (d). Removal of the PMMA template produces the freestanding 3D structures (e).

Within this fabrication scheme, the deposition was performed by full immersion of the samples into a plating solution and a voltage source was employed to apply a potential of 3.5 V between the sample holder and an aluminum counter electrode (Figure 3.3, left). While this approach enables the large-scale fabrication of 3D electrodes, a major disadvantage is the lack of real-time control over the deposition. Additional drawbacks are the use of large amounts of cyanide-containing solution, as well as the slow change in gold concentration and salt drag out due to the reuse of the same plating solution over extended periods of time.

The first aim of this body of work therefore was to develop a fabrication scheme that enables better control over the production of 3D structures, since a regulated process is a prerequisite for the deposition of multiple different structures on a single chip as presented in Chapter 4. This necessitates the downscaling of the process to facilitate the deposition of gold only inside the defined apertures (Figure 3.3, right), which, in contrast to the full immersion into the plating bath and resulting deposition both on the sample and sample holder, facilitates feedback about the state of the deposition without interference of the supporting material. Furthermore, employing only small volumes of gold plating solution taken from a large stock enables the usage of a fresh solution of equal concentration for each experiment, only necessitating a recycling of the solution once the original stock is depleted. This warrants a continuous gold concentration and constant

conditions as well as safer handling. Furthermore, the usage of a potentiostat and three-electrode setup enables better control over the applied voltage and facilitates the recording of the current.

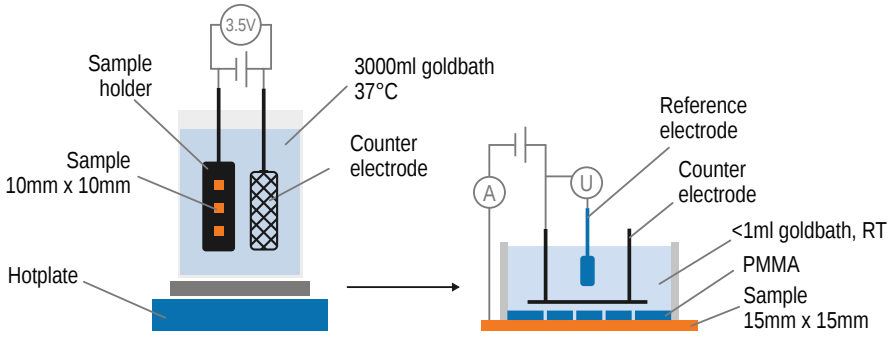

Figure 3.3: Design concept: Adapting the fabrication scheme from full immersion (left) to a controlled deposition only within the apertures defined in PMMA (right). In this manner, it is possible to achieve a better controllability by elimination of changes in the bath composition and to enable the control of the deposition by use of a potentiostat, allowing to observe changes in the current.

An important aspect for the design of the setup is the positioning of counter and reference electrode. As reported by Zhang *et al.*,[118] the positioning of the electrodes within an electrochemical cell employing a three-electrode setup greatly influences the obtained data. They found that with the reference electrode inside the path of current, the results obtained for electrochemical experiments were strongly dependent on the distance between reference and working electrode. They suggest placing the reference electrode outside the way of current and close to the working electrode to achieve consistent measurements.[118] Since this is not possible for the setup presented here while at the same time maintaining a homogeneous electric field via the employment of a large counter electrode, the reference electrode was placed at a constant distance from the counter electrode, with only minor changes in the distance between working and counter and thus working and reference electrode from one experiment to the next. In order to achieve a stable system, counter and reference electrode were mounted into a lid (see Figures 3.1 and Figure 3.3, right), with the reference electrode above the counter electrode and thus outside of the applied electric field. The initial counter/reference electrode installation was included into a lid made of acrylic glass that tightly fit onto the glass rings defining the deposition reservoir (Figure 3.1, top left). Later, both counter and reference electrode were used as free-standing structures mounted

into a piece of acrylic glass (Figure 3.1, right). This design facilitates a more convenient usage, with the lid clamped into a stand and being lowered into the solution, resolving issues with discrepancies between lid and glass ring size and allowing for a more stable position since, in contrast to the lid fitted over but not clamped onto the glass ring, counter and reference electrode are now fixed in their vertical location. Another change with respect to previous work is the reduction of the temperature from 37°C to room temperature. This was done due to several reasons: First, due to the small size of the samples and design of the counter/reference electrode setup, controlling the bath temperature by introduction of a thermometer would have been challenging and would have necessitated a re-design of the setup. Second, while the sample holder was designed to enable good thermal conductivity, the heating of the sample on a hotplate resulted in problems with polydimethylsiloxane (PDMS) adhesion, which was originally employed for gluing rings onto the samples. Last, decreasing the temperature had negligible effect on the crystal structure of the formed deposits as compared to the influence of the applied potential. Figure 3.4 depicts gold electrodeposited onto unstructured samples at different temperatures and potentials. While the deposition at -1.10 V results in needle like crystals, the deposition at -1.25 V yields triangular crystals, with the difference between RT and approximately 37°C being merely the size of the crystals.

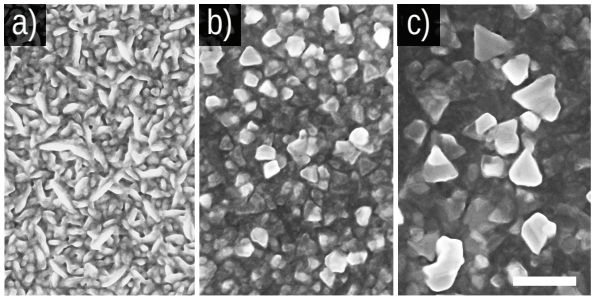

Figure 3.4: SEM images of gold deposited at different temperatures and potentials. (a) -1.10 V, 30 s, RT (b) -1.25 V, 30 s, RT, (c) -1.25 V, 30 s, tempered on a 45°C hotplate for 30 min prior to deposition. The influence of the deposition potential is considerably more pronounced than the influence of the temperature. Scalebar represents 500 nm.

Within this new fabrication process, glass rings of 14 mm diameter and 10 mm height were thus glued onto the samples as liquid reservoir for the plating bath during the electrodeposition. Depositions were then performed using a custom-build sample holder and counter and reference electrode setup (Figure 3.3) on a Biologic VSP-300 potentiostat, followed by removal of the glass ring and PMMA template in acetone. An aspect which proved to be significant for homogeneous deposition is the ascertainment of even penetration of the plating bath into the template. Early depositions resulted in a very inhomogeneous size distribution, which was significantly improved

by enforcing even wetting by repeated up-and-down pipetting of the bath solution on top of the samples prior to the electrodeposition. Furthermore, epoxy residues were found to settle on the substrates during ring removal, which could be circumvented by placing the samples upside-down into acetone first and transferring them to fresh acetone after the ring and consequently the attached epoxy were removed from the sample.

Inspired by the publication of Jahed *et al.*,[120] the fabrication scheme depicted in Figure 3.2 was expanded to include hollow pillars and hollow mushrooms, with the aim to make the different 3D structures reported in the literature accessible within one fabrication scheme and, at the same time, introduce the novel hollow mushroom 3D design as hybrid between mushrooms and hollow structures. Figure 3.5 depicts the fabrication of hollow structures. After spincoating of PMMA (a), circles are written into PMMA via electron-beam lithography (b). Following development, gold is electrodeposited into the apertures. Deposition up to the boundary of the PMMA template yields hollow pillars (c), deposition beyond the boundary of the template yields hollow mushrooms (d,e). With the parameters employed in this study, the obtained PMMA thickness averages to 1048∼9 nm

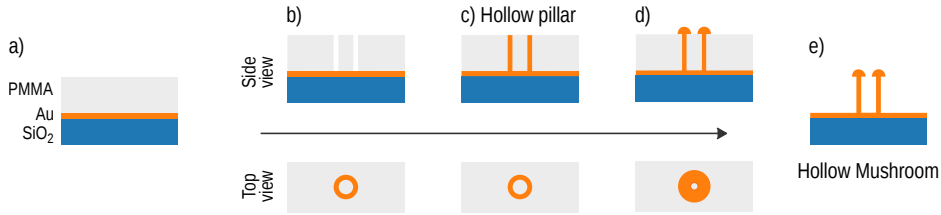

Figure 3.5: Fabrication concept: PMMA is spincoated onto a gold-on-silicon sample ((a) exemplary single structure). (b) Rings are defined via electron-beam lithography. Afterwards, electrodeposition of gold up to the boundary of the PMMA template produces hollow pillars (c), while continued deposition beyond the boundary of the template yields hollow mushrooms (d). Removal of the PMMA template produces the freestanding 3D structures (e).

and 1053∼39 nm as determined by ellipsometry and Dektak stylus profilometry, respectively, therefore resulting in structures with a stalk height of approximately 1 µm. A dosis test was performed in order to determine optimal electron-beam lithography parameters for the fabrication of hollow structures. The outer diameter of the hollow structures was matched to the diameters employed for solid structures in earlier studies, namely 300, 600, and 800 nm. For each structure diameter, the wall thickness of the ring written into PMMA was varied from 25 to 50, 100, and 150 nm. The dosis was tested from 400 µC/cm^2 to 2028 µC/cm^2 with a factor of 1.07 from one dosis to the next.

Since electron-beam sensitive PMMA cannot easily be analyzed via SEM, especially for high aspect ratio structures where the determination of full exposure down to the underlying substrate is necessary, a thin layer of gold was electrodeposited inside the template and the analysis of the dosis test performed after PMMA removal. While both the 600 nm and 800 nm diameter structures with 100 nm ring thickness were already fully exposed at the lowest investigated dosis, structures with ring size of 50 nm needed at least 687 µC/cm^2 to enable full exposure down to the underlying gold, while structures with 25 nm ring size needed at least 1264 µC/cm^2. Structures of 300 nm in outer diameter and either 150 nm or 100 nm in ring thickness were solid. Furthermore, for structures of 300 nm in diameter and either 50 nm or 25 nm in ring thickness, the PMMA plug was too small to be mechanically stable and thus tilted, which became apparent once the electrodeposition was conducted up to the boundary of the template (Figure 3.6). To a lesser extend, this effect could also be observed for structures of 600 nm in outer diameter and ring thicknesses of either 150 nm or 100 nm. For this structure size, the problem can be resolved employing smaller ring thicknesses. For structures of 300 nm in diameter, however, this issue cannot be circumvented within this fabrication scheme. Their production was therefore discontinued.

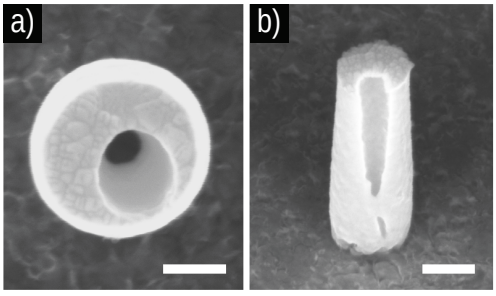

Figure 3.6: SEM images of 300 nm structures: the mechanical instability of the PMMA plug results in its tilting during the deposition, which can either result in an off-center opening (a) or a hole along the length of the structure (b). Scalebar in (a) represents 150 nm, scalebar in (b) is 250 nm.

As stated above, decreasing the ring size resulted in a significant increase in necessary dosis, which again resulted in an enlargement of the structure, yielding similarly sized structures for doses close to the minimal dosis for rings of 100 nm, 50 nm and 25 nm (Figure 3.7). Figure 3.8 shows the development of the external and internal diameter as well as the wall thickness of structures with 800 nm mask diameter and 25 nm and 50 nm ring thickness with increasing dosis. As already noted above, structures with 50 nm wall thickness with respect to their mask parameters became available at a dosis of 687 µC/cm^2, while structures with 25 nm ring size needed 1264 µC/cm^2 to enable full exposure down to the underlying gold. Increasing the dosis from there lead to a linear increase

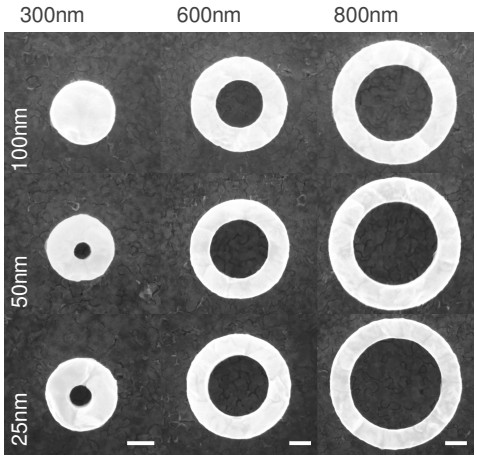

Figure 3.7: SEM top-view images of different structure sizes (300, 600, and 800 nm in outer diameter with template ring thickness of 25, 50 and 100 nm) at approximately the minimum dosis required for their preparation. Within one structure size, the increase in dosis required for the full exposure of smaller ring thicknesses results in similarly large structures, irrespective of the wall thickness of the template. Scalebar represents 150 nm.

in outer diameter and, consequently, a linear decrease in inner diameter. At the onset dosis for 25 nm rings, the structure size is comparable to that of 50 nm rings at their onset dosis. Due to the slightly larger internal diameter, a parameter that is highly important for efficient cellular protrusion into the opening, all following structures, both 600 nm and 800 nm in diameter, were written with a ring thickness of 25 nm. The dosis was chosen slightly above the onset dosis to prevent extensive effects due to batch-to-batch variations in the PMMA thickness.

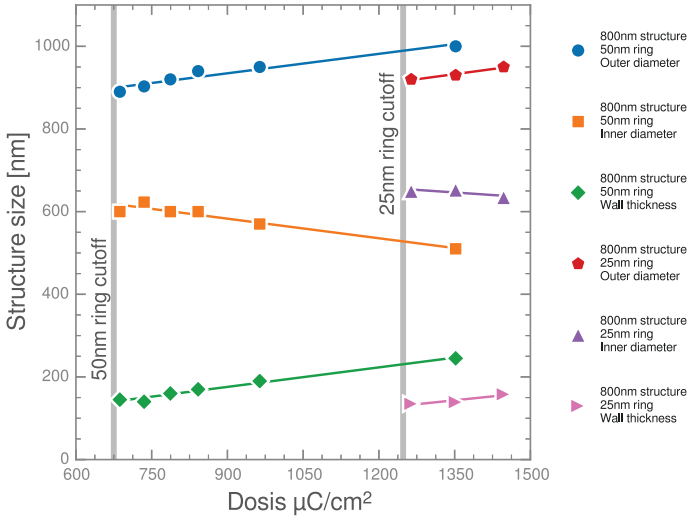

Figure 3.8: Development of the outer and inner diameter as well as the wall thickness for structures of 800 nm mask diameter. Structures with 50 nm wall thickness with respect to their mask parameters became available at a dosis of 687 µC/cm^2 while structures with 25 nm ring size needed 1264 µC/cm^2 to enable full exposure down to the underlying gold. Increasing the dosis from this onset dosis resulted in a linear increase in diameter and wall thickness, and linear decrease in inner diameter.

For the initial establishment of the fabrication parameters, gold was deposited at different potentials in the range of -1.00 V to -1.25 V vs. Ag/AgCl. Assuming that the reference electrode has a potential close to that of Ag/AgCl in saturated KCl, which is about 0.20 V against SHE, and $[Au(CN)_2]^-$ having a standard potential of -0.61 V, this results in an overpotential of between 190 mV and 440 mV. Figure 3.9 shows representative current traces for depositions performed between -1.00 V and -1.25 V at 50 mV intervals. After an initial sharp peak in the current, which is most likely due to both capacitive charging of the double layer as well as seed formation, the current exhibits a plateau. Eventually, a bend in the current occurs, after which the current starts to increase. SEM

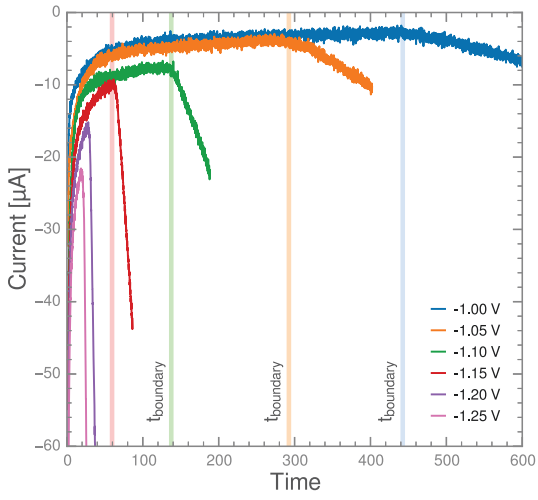

Figure 3.9: Current traces recorded during the deposition of 3D gold structures at different potentials. After an initial spike, the current exhibits a plateau. Eventually, the current reaches a bend and starts to increase. At the bend in the current, the deposition is just at the boundary of the PMMA template ($t_{boundary}$). Afterwards, the current increases due to an increase in surface area as the deposition transitions from 1D to 3D growth. Shifting the applied potential to more negative values resulted in a significant decrease in $t_{boundary}$ for every 50 mV change in potential.

analysis of the resulting structures proved that the bend in the current occurs once the deposition reaches the boundary of the PMMA template, thus transitioning from one-dimensional growth inside the template to three-dimensional growth beyond. The resulting change in the surface area available for the deposition results in an increase in reduction events and thus in the recorded current. While depositions in the literature are often done by application of a certain current density rather than by application of a set potential, the deposition speed is independent of the available surface area when using the method employed here, while at the same time providing information about the state of the deposition via the amplitude of the current. Therefore, for a precise control of the structures, a voltage controlled approach is preferable over a current controlled method for the system presented here.

As can be seen in Figure 3.9, changing the potential greatly influences the deposition speed. Figure 3.10 shows the values obtained for the boundary time $t_{boundary}$ vs. the employed potential. Additionally, the deposition velocity was approximated by division of the expected template height of 1050 nm by $t_{boundary}$. For every 50 mV shift to more negative potentials, the deposition rate approximately doubles. This strong dependency again confirms the need of well-controlled parameters for reproducible results.

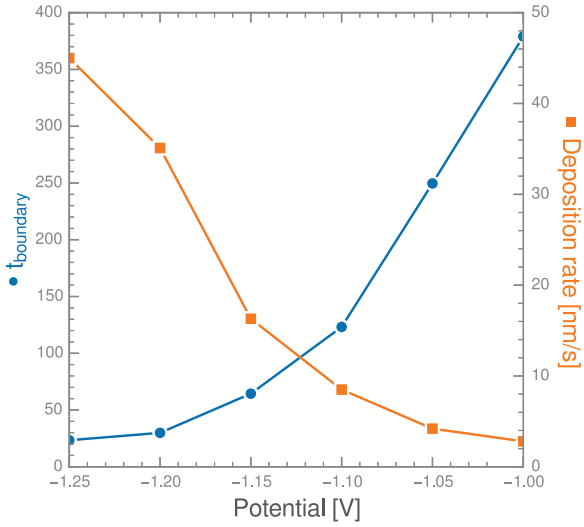

Figure 3.10: Time needed to reach the boundary of the PMMA template ($t_{boundary}$) vs. applied potential as well as deposition velocity as approximated by division of the expected template height of 1050 nm by $t_{boundary}$. The deposition velocity about doubles for every 50 mV shift to more negative potentials. This strong dependency necessitates good control over the applied potential.

One severe problem surfacing during these initial experiments were large variations of the template stability with a clear dependence on the applied potential. Figure 3.11 shows exemplary structures as obtained for depositions at different potentials. While depositions at -1.00 V generally yielded intact structures (Figure 3.11 a,b), increasing the potential to -1.05 V resulted in the formation of both solid and hollow structures (Figure 3.11 c and d, respectively) from hollow templates. The same effect occurred for the deposition at -1.10 V (Figure 3.11 e,f), while depositions at -1.25 V yielded intact structures with high fidelity (Figure 3.11 g,h). Under certain conditions, the PMMA plug masking the interior of the hollow structure thus seems to be removed during the deposition. Supposedly, this is aided by the fact that, in contrast to the situation depicted in Figure 3.5, the sidewalls of the template are not fully vertical (Figure 3.12). This is due to the high dosis needed for these high aspect ratio structures, with the expansion of the electron-beam inside the

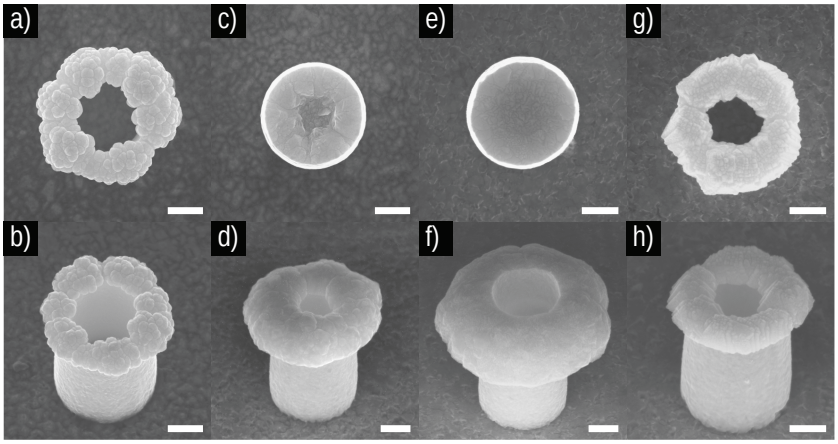

Figure 3.11: SEM images of structures obtained by deposition at (a,b) -1.00 V for 300 s, (c,d) -1.05 V for 200 s (c), or 400 s (d), (e,f) -1.10 V for 110 s (e), or 190 s (f), (g,h) -1.25 V for 27 s. Scalebar represents 300 nm. Sample tilt in bottom row is (b) 30° and (d,f,h) 45°.

PMMA resulting in a wider opening at the PMMA/substrate interface than at the top of the resist. This generates an upwards force during electrodeposition that could result either in an 'outgrowth' of the plug, yielding mushrooms with circular opening as in Figure 3.11 (f), in a tilting of the plug, resulting in structures that exhibit an off-center opening, or in complete removal of the plug as in Figure 3.11 (c) and (e). Figure 3.13 shows the dependency of the percentage of intact structures

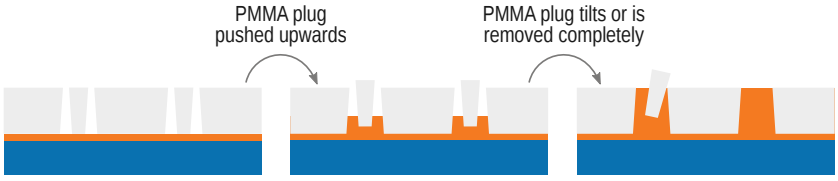

Figure 3.12: Schematic representation of the process of PMMA plug removal: Due to the tilted sidewalls, the deposition of gold generates an upwards force that can either result in a partial outgrowth or full removal of the PMMA plug.

on the applied potential, as well as the correlation between intact structures, development time, and different potential. As can be seen, the PMMA plug is particularly unstable in the potential range between -1.05 V and -1.10 V. While the development time does not influence the structure stability for depositions at -1.25 V, increasing the development time results in a strong decrease in structure stability for depositions at -1.10 V. The reason for this instability in the potential range

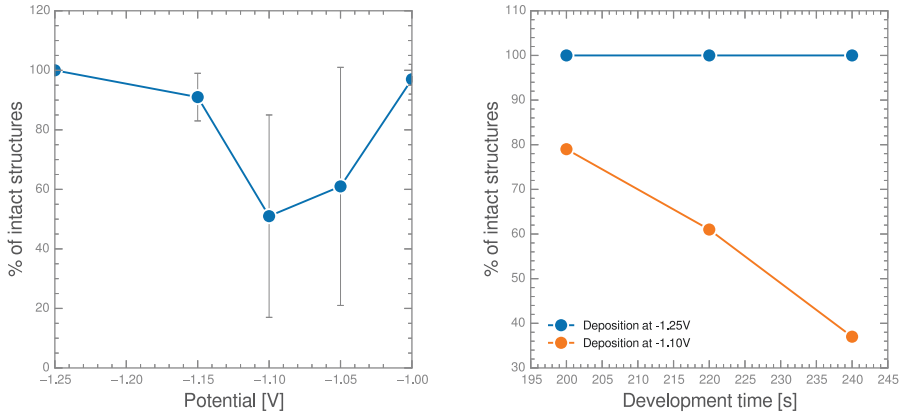

Figure 3.13: Left: Percentage of intact structures for depositions at different potential. While hollow structures can be produced with high fidelity both at -1.00 and -1.25 V, in between these two potentials, the resulting samples show large variations in structural stability. Error bars represent the corrected sample standard deviation. Right: Percentage of intact structures in dependence on the development time and applied potential. While an increase in the development time does not influence the structural stability of samples deposited at -1.25 V, longer development times result in a strong decrease in the number of intact structures for depositions at -1.10 V.

from -1.05 V to -1.15 V remains unknown. However, several influential parameters could be distinguished. As already stated above, the potential seems to play a crucial role in this process. Linear sweep voltammetry between 0 and -1.5 V showed a distinct peak at around -1.12 V, so in the range of potentials that seems to result in significant instability of the PMMA plug. Furthermore, the crystals deposited in this potential range are sharper than both below and above the range. While the contact time could also play a role in promoting the removal of the plug due to a degradation of the PMMA, contact time alone does not seem to be problematic as can be seen in Figure 3.14. The SEM images show the edge of the FZ Jülich Logo, written into the PMMA at the center of each

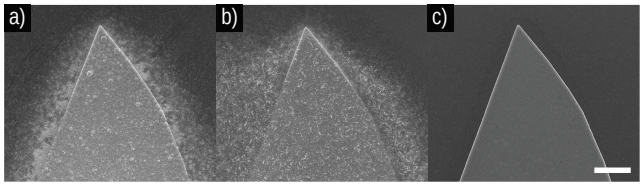

Figure 3.14: PMMA lifting and gold underplating for deposition at (a) -1.00 V for 300 s, (b) -1.05 V for 200 s, and (c) -1.15 V for 5 s. Scalebar represents 5 µm.

sample. While lifting of the resist and resulting underplating can be observed for depositions at -1.00 V for 300 s (Figure 3.14 a), underplating is significantly increased for depositions conducted

at -1.05 V for 200 s despite shorter contact time (Figure 3.14 b). If the deposition is only conducted for 5 s at -1.15 V, no underplating can be observed (Figure 3.14 c).

In order to achieve a well-controlled process, the characteristics of the deposition and resulting structures are required to comply with the following three qualities:

1. **Structural stability:** The structure of the provided template is preserved during the electrodeposition
2. **Controllability:** The deposition should be reasonably slow to enable good control over the process
3. **Time:** The deposition should be fast enough to maintain a short contact time to the plating bath since the cyanide in the deposition bath will degrade the template and result in underplating

However, while only depositions at -1.25 V and -1.00 V serve requirement 1, neither of them serve both points 2 and 3. Depositions at -1.25 V reach $t_{boundary}$ within less than 30 s, thus precluding good control over the cap size by real-time adaption of the deposition parameters, and depositions at -1.00 V require too much time, resulting in the initiation of PMMA lift-off and underplating beneath the resist. In order to facilitate the fabrication of hollow structures with high fidelity, the deposition was subsequently performed as a two-step process. The first deposition step was conducted at -1.25 V for 5 s to stabilize the PMMA plug, followed by a second step at -1.10 V, facilitating an adequately slow deposition to enable good control over the process. In this manner, it was possible to produce hollow pillars and mushrooms (Figure 3.15) with good reproducibility.

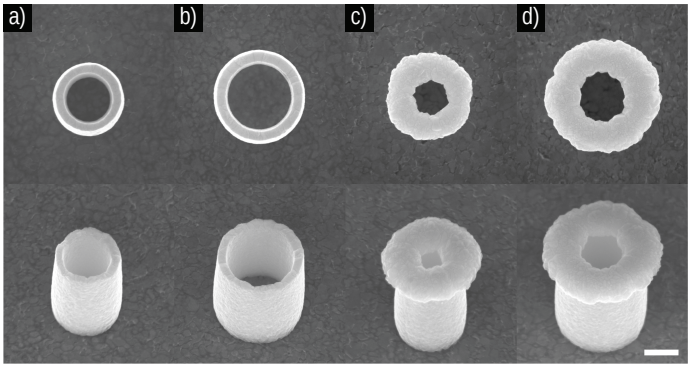

Figure 3.15: SEM images of hollow pillars (a,b) and hollow mushrooms (c,d) with (a,c) 600 nm, and (b,d) 800 nm stalk width. Scalebar represents 350 nm. Bottom row is acquired at 30° sample tilt.

With the approach presented here, hollow structures of 739 ∼ 11 nm in outer diameter with opening size of 438 ∼ 16 nm and thus ring thickness of 150 nm were obtained for 600 nm masks and structures of 948 ∼ 12 nm in diameter with opening size of 641 ∼ 17 nm and thus ring thickness of 153 nm were obtained for 800 nm masks. Despite their larger actual size, for simplicity's sake, the structures will nonetheless be defined by their outer mask diameter in future reference.

Due to the fact that the reaching of the boundary of the template can easily be observed in the current trace recorded during the deposition, a tailoring of the resulting structure size is possible, with depositions stopped before the boundary time yielding hollow pillars, while depositions continued past $t_{boundary}$ yield structures with varying mushroom cap-size. Figure 3.16 shows a characteristic current trace and exemplary structures as obtained by stopping the deposition at points (a) through (d). Due to this clear correlation between the recorded current and characteristics of the resulting nanostructure, the presented approach facilitates a direct control over the obtained 3D design.

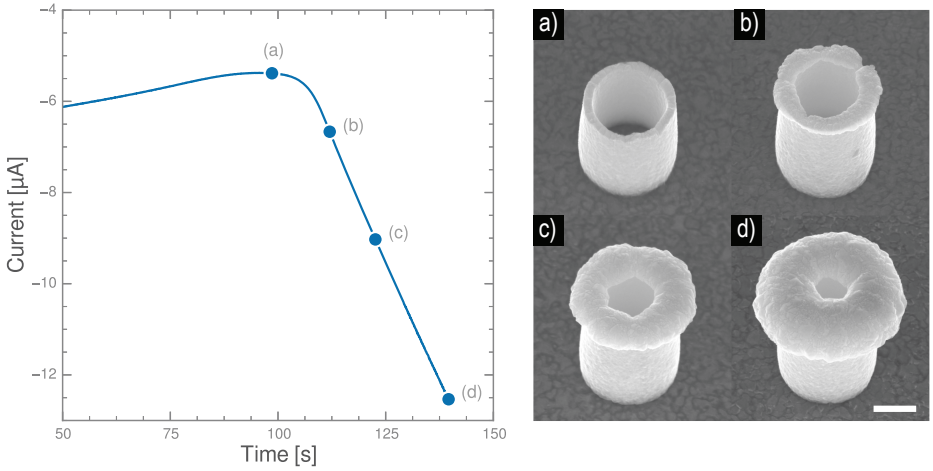

Figure 3.16: Characteristic current trace recorded during the deposition of hollow mushrooms and SEM images of representative structures for timepoints (a) through (d). At timepoint (a) where $t < t_{boundary}$, the resulting structures are hollow pillars. Beyond $t_{boundary}$, the cap size of the hollow mushrooms increases with increasing time. Due to this direct correlation between the nanoscale characteristics of the structures and the measured current, a good control over the resulting structures is possible. Scalebar represents 400 nm. Images acquired at 30° sample tilt.

However, while this process initially enabled the fabrication of hollow structures with high fidelity, later sample batches again exhibited the problem of PMMA plug removal. SEM analysis of early and later samples proved significant differences in the sample roughness (Figure 3.17). While earlier

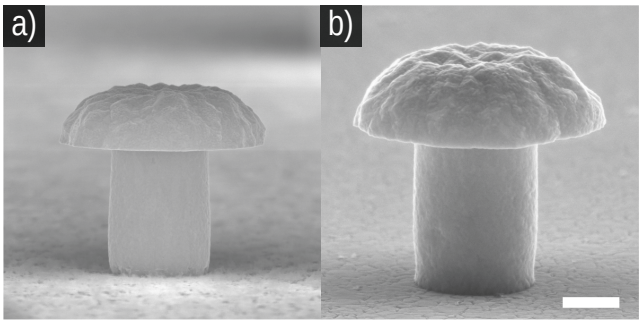

Figure 3.17: SEM images of an earlier sample (a) and later sample (b). While earlier samples exhibited a very rough surface, later samples were significantly smoother. Scalebar represents 500 nm. (a) is acquired at 80° sample tilt, (b) at 75° sample tilt.

samples exhibited a very rough surface, thus facilitating stronger PMMA adhesion, later samples were significantly smoother, which resulted in an easier removal of the PMMA plug. The problem of template instability will thus also be changed with changes in the PMMA adhesion. Since it was not possible to receive samples similar to the ones produced for earlier batches, the first deposition step was changed from -1.25 V to -1.35 V while the time for this step was kept at 5 s, which alleviated the issue in most cases. However, for future studies, a better control over the sample characteristics is of utmost importance since the stability of the process critically depends on this.

In order to enable the adaptation of the parameters obtained for the deposition time needed for either hollow pillars or hollow mushrooms to the fabrication of solid structures, solid pillars and mushrooms were also deposited according to the two-step process employed for the hollow structures. Figure 3.18 depicts exemplary pillars and mushrooms from 300 nm (a), 600 nm (b), and 800 nm (c) templates, with a mask diameter of 300 nm yielding structures of $370 \sim 11$ nm in diameter, 600 nm masks yielding structures of $676 \sim 18$ nm in diameter, and 800 nm masks yielding structures of $883 \sim 16$ nm in diameter with respect to the stalk width of the structure. As with the hollow structures, the cap size of mushroom-shaped structures can be tailored by changing the deposition time. In addition to hollow structures of 600 nm and 800 nm stalk width, bigger structures were developed with outer mask diameters of 2 µm, 3 µm, 4 µm, 5 µm, and 7.5 µm and 50 nm, 50 nm, 100 nm, 100 nm, and 150 nm in wall thickness, respectively (Figure 3.19). Due to their larger opening size, better cellular protrusion and thus coupling was expected for these devices,

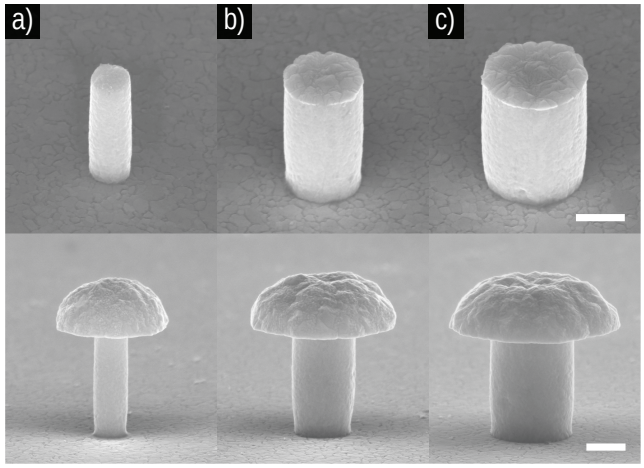

Figure 3.18: SEM images of solid pillars (top) and mushrooms (bottom) with (a) 300 nm, (b) 600 nm and (c) 800 nm stalk width. Scalebar represents 400 nm. Top row is acquired at 45°, bottom row at 75° sample tilt.

with larger mushroom structures intended to induce a large membrane curvature in the center of the ring while producing good cellular attachment around the periphery due to the mushroom cap. The structure sizes obtained are 2208 ∼ 17 nm in diameter with opening size of 1830 ∼ 13 nm and thus ring thickness of 189 nm for 2 µm masks, 3230 ∼ 28 nm in diameter with opening size of 2828 ∼ 30 nm and thus ring thickness of 201 nm for 3 µm masks, 4278 ∼ 32 nm in diameter with opening size of 3737 ∼ 30 nm and thus ring thickness of 271 nm for 4 µm masks, 5279 ∼ 43 nm in diameter with opening size of 4736 ∼ 42 nm and thus ring thickness of 272 nm for 5 µm masks, and 7836 ∼ 55 nm in diameter with opening size of 7148 ∼ 53 nm and thus ring thickness of 344 nm for 7.5 µm masks. As with smaller structures, big hollow templates experience the issue of plug removal

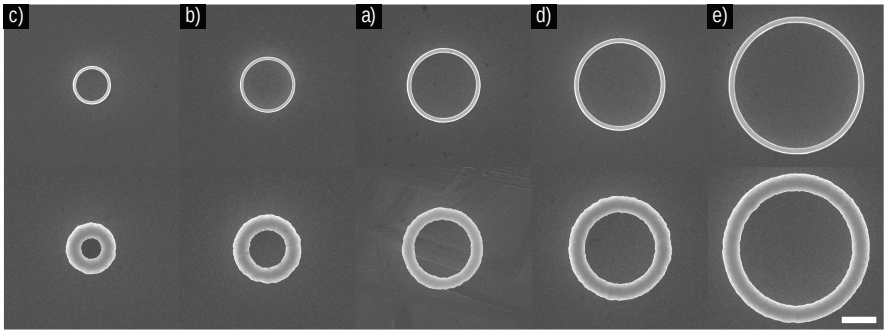

Figure 3.19: SEM top-view images of big hollow pillars (top) and mushrooms (bottom) with (a) 2 µm, (b) 3 µm, (c) 4 µm, (d) 5 µm, and (d) 7.5 µm foot width. Scalebar represents 2 µm.

during electrodeposition. This was unexpected since the larger size of the plug and resulting larger contact area between substrate and PMMA was expected to warrant better adhesion. While the underlying problem is not fully understood, there seems to be a relation between the ratio of diameter and wall thickness and the tendency for plug removal, with 2 µm structures of 50 nm ring thickness showing a higher tendency for template instability than 3 µm structures of 50 nm ring thickness, as is the case for 4 µm structures with 100 nm ring thickness as opposed to 5 µm structures with 100 nm ring thickness. Ultimately, the effect was most pronounced for 4 µm structures, with only few intact structures fabricated overall, most of which were located on scratches and other surface defects. Figure 3.20 shows tilted views of successfully fabricated big hollow mushrooms (a-c) as well as the problems occurring during the fabrication with partially pushed out (d), tilted (e), and completely removed PMMA plug (f). Since big hollow structures were only fabricated on later

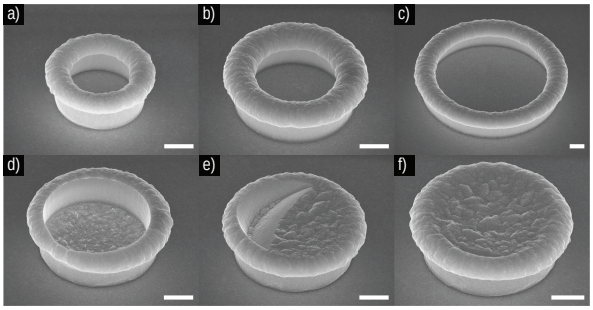

Figure 3.20: SEM images of big hollow mushrooms with (a) 3 µm, (b) 4 µm, and (c) 7.5 µm foot width. The bottom row depicts problems arising during the deposition of big hollow structures. Analogous to smaller structures, the PMMA plug can be pushed upwards during the deposition (d). Further displacement of the plug results in its tilting (e) and finally complete removal (f), yielding solid structures. Scalebars represent 1 µm. Images acquired at 45° tilt.

sample batches, it is not possible to determine whether their structural integrity would have been improved on the earlier, rougher sample batches. Another possibility that could provide better maintenance of the PMMA template would be the application of an adhesion promoter such as AR 300-80 manufactured by Allresist specifically for their AR-P PMMA series. This approach should be developed in parallel to a better sample control in the future.

An alternative to changing the structure by modification of the mask design is the application of a large overpotential. Figure 3.21 shows structures fabricated employing solid templates at a potential of -1.50 V for 16 s. Due to the high overpotential, the formed structures exhibit a very sharp, spiky morphology, consistent with theoretical expectations. While these structures are significantly too large to enable the interaction with neurons, their large area and expected decrease in impedance could be advantageous for the interaction with cardiac cells.

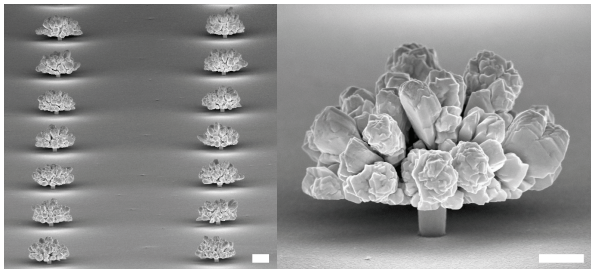

Figure 3.21: SEM images of cauliflower-like structures, fabricated by gold deposition at very high overpotential. Scalebars represent 2.5 µm (left) and 1 µm (right). Images acquired at 75° tilt.

3.2.2 HL-1 culture on 3D structures

In order to evaluate the interaction of cells with the fabricated 3D structures and to determine which design facilitates a tight contact, focused ion-beam (FIB) sectioning was employed. Initially, HL-1 cells were seeded onto different hollow structures. HL-1 cells are a cardiomyocyte-like cell line derived from a mouse atrial tumor that maintain the characteristics of cardiac myocytes such as morphology, biochemical behavior, and electrophysiological behavior, even after multiple passages.[121] They are often employed as model system for the benchmarking of MEA-based devices due to their ease of use and stability as compared to primary cells and good electrophysiological properties. In the past, their interaction with 3D structures has been intensively studied,[49] therefore, first experiments were performed employing HL-1 cells for the sake of comparability. Figure 3.22 shows SEM images of HL-1 cells on hollow pillars (a) and mushrooms (b), growing seemingly unperturbed by the presence of 3D structures.

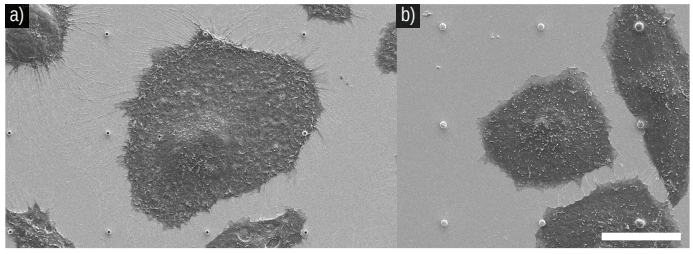

Figure 3.22: SEM images of HL-1 cells grown on 3D structures arranged in a 25 µm grid. These cells are very large as compared to the structures, with cell diameters of several tens of micrometers. Scalebar represents 20 µm.

All focused ion-beam sections of HL-1 cells were either performed on 800 nm structures or on big hollow structures to provide a large opening for the cells to grow into. The developed structures were cleaned and then coated with a mixture of fibronectin and gelatin to facilitate cell adhesion. HL-1 cells were maintained on the samples until an intermediate cell density was achieved. Afterwards, the cells were chemically fixed by incubation with a glutaraldehyde solution, a highly reactive

dialdehyde that quickly crosslinks the proteins within the cell[122] and also exhibits some reactivity towards lipids, nucleic acids, and carbohydrates.[123] In this manner, the cell is quickly transformed into an interconnected mesh. Subsequently, the samples were dehydrated to enable the study in high vacuum as present in an electron microscopy chamber. The dehydration can be performed in different ways. In the easiest case, water is exchanged for ethanol via slow exchange through a concentration series and the ethanol is then exchanged for CO_2, which is brought to the critical state and then removed from the sample. The critical point of CO_2 is at 31°C and 7.4 MPa,[71] at which point the boundary between liquid and gaseous phase vanishes, creating one phase called supercritical CO_2, which is then removed from the system. Employing this approach called critical-point drying (CPD), the cells do not experience the surface tension of a liquid/gas interface, which would crush the cell and destroy any discernible structural information if the liquid was merely left to dry. Following earlier publications,[49] experiments were first performed employing this approach. Figure 3.23 shows SEM images acquired from CPD-prepared HL-1 cells. As has been

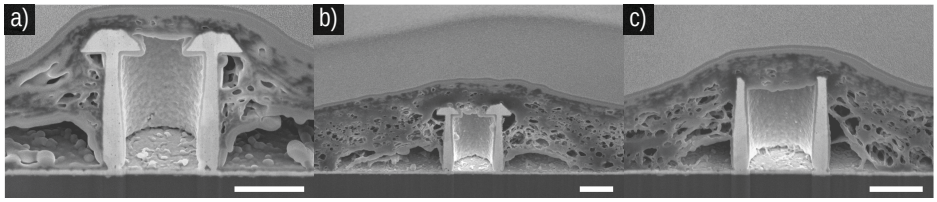

Figure 3.23: Focused ion-beam sections of HL-1 cells on hollow pillars and mushrooms of 800 nm stalk width. The cells tightly engulf hollow mushrooms but detach from the sample close to the base (a,b) of the structure as has been previously reported.[49] While the cells form a close contact in the upper area of hollow pillars, they fan out in a tent-like fashion around the base. In contrast to the results reported in the literature,[50] no cellular protrusion can be observed into the interior of the structures, with only very little bending into the opening of the hollow structure. Scalebars represent 500 nm.

reported before, the cells tightly engulf structures exhibiting a mushroom-shaped cap but detach along the substrate close to the 3D structure[49] (Figure 3.23 a,b), while they form a tent-like interface with plain pillars, as can also be observed for hollow pillars (Figure 3.23 c). In contrast to the publication by Lin *et al.*,[50] who reported that HL-1 cells protrude into hollow pillars of 400 nm in inner diameter, only a slight bending into the opening can be observed for the hollow pillar in Figure 3.23 (c), despite their larger opening size of over 600 nm.

In accordance with previous reports,[49] the cells exhibit a very spongy interior. This is a fixation artifact due to the removal of intracellular matter during the CPD process and subsequent cy-

toskeletal collapse. While the fixation process inherently results in the introduction of artifacts such as significant shrinking of 5-17%,[56] the destruction of the cellular ultrastructure can be circumvented through a resin embedding step. After solvent exchange to ethanol, the cells are infused with an epoxy resin through a concentration series in ethanol, slowing achieving full perfusion of the cell with the resin. Excess resin is removed with ethanol to enable the imaging of the cell in the SEM and after curing of the resin, the samples can be sputtered and directly used for electron microscopy studies.[124] Figure 3.24 shows FIB sections of initial experiments employing this approach. The obtained results suggest a tight contact between the cell and the electrode with only very little detachment around the base of the structure. However, due to the lack of contrast between cellular matter and the embedding medium, no direct conclusions can be drawn since the tight contact could also be due to resin filling the formed gaps rather than actual cell-structure interaction. As before, only a slight bending into the opening can be observed rather than full protrusion. While an extension into the structure can be observed in Figure 3.24 (c), the question whether this is a cellular process or a result of the resin cannot be answered without contrast enhancement. The differentiation of cell and embedding medium is only possible if sufficient contrast between cell and resin is given.

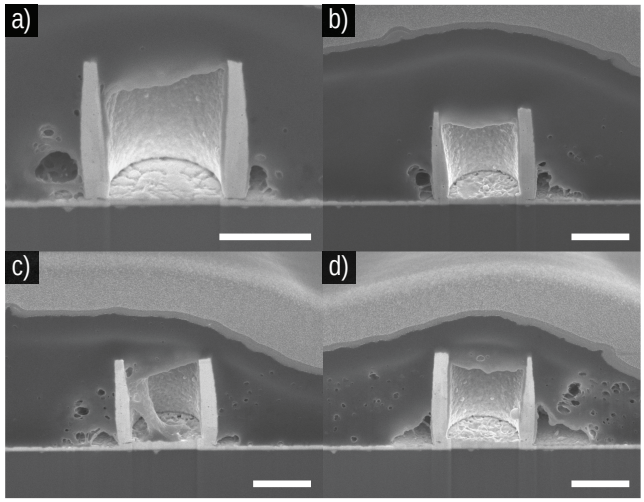

Figure 3.24: Focused ion-beam sections of HL-1 cells on hollow pillars of 800 nm stalk width, dehydrated via resin embedding. While the results suggest a tight contact between cell and 3D structure, the lack of contrast between the cell matter and embedding medium precludes any conclusions. As before, only a slight bending into the opening can be observed. While an extension into the structure can be seen in (c), the question whether this is a cellular process cannot be answered without contrast enhancement, enabling a differentiation of cell and embedding medium. Scalebars represent 500 nm.

In order to enable an artifact minimized process but also facilitate the differentiation of cell matter and embedding medium, the cells were stained with osmium tetroxide and uranyl acetate

for contrast enhancement. Osmium primarily interacts with lipids in membranes by oxidation of and binding to unsaturated bonds in fatty acids,[123,125] thereby facilitating their visualization during electron microscopy studies due to presence of the heavy metal, which provides a sufficient scattering of the electron-beam. The mechanism of uranyl staining is still poorly understood and generally declared as 'unspecific', however, it is known that uranyl interacts strongly with phosphate and amino groups.[123] The combination of these two stains results in significant contrast enhancement as can be seen in Figure 3.25. Furthermore, the enhanced fixation of the cellular compartments prior to the ethanol dehydration facilitates a significantly improved ultrastructural preservation. Even though the sections in both Figure 3.24 and 3.25 were obtained from cells containing the 3D structures in their central area, significant height differences can be observed for cells with and without osmium post-fixation.

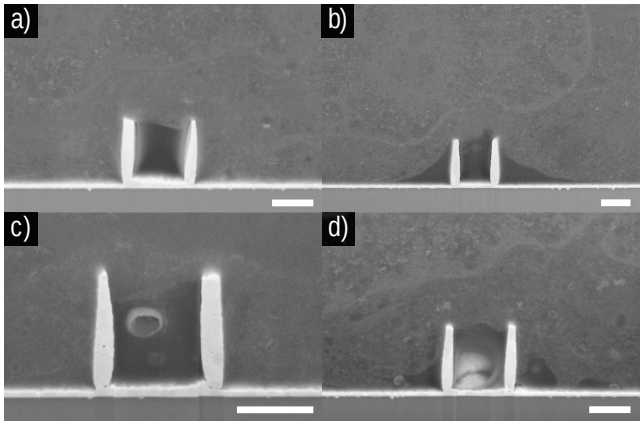

Figure 3.25: Focused ion-beam sections of HL-1 cells on hollow pillars of 800 nm stalk width post-fixed with osmium tetroxide, uranyl acetate and embedded in epoxy resin. While in some cases a tight contact and slight protrusion into the interior of the structure can be observed (a,b), in other cases, the cell adapts a loose, tent-like shape (c,d). The circular openings inside the structures in (b) and (d) are bubbles enclosed in the resin embedding medium. Scalebars represent 500 nm.

Due to the heavy metal staining of the cellular membranes, cell and embedding medium can be clearly distinguished and it even becomes possible to visualize different cellular compartments. Three different behaviors of the HL-1 cells on hollow pillars could be observed during this study: The cells either tightly engulfed the structures with slight bending into the interior of the hollow pillar as seen in Figure 3.25 (a,b), they formed a loose, tent-like contact as seen in Figure 3.25 (c,d), or they exhibited a hybrid behavior with one side tightly engulfed and the other in the tent-like configuration. The prevalence of these cases was 5/13 tight engulfment as in (a,b), 5/13 tent-like as in (c,d), and 3/13 hybrid (n=13). Nevertheless, no cellular protrusion as reported by Lin *et al.*[50] could be observed. Therefore, HL-1 cells were cultured, fixed, stained, and embedded in epoxy resin

on big hollow pillars to determine whether larger openings facilitate cellular protrusion. Figure 3.26 shows exemplary FIB sections.

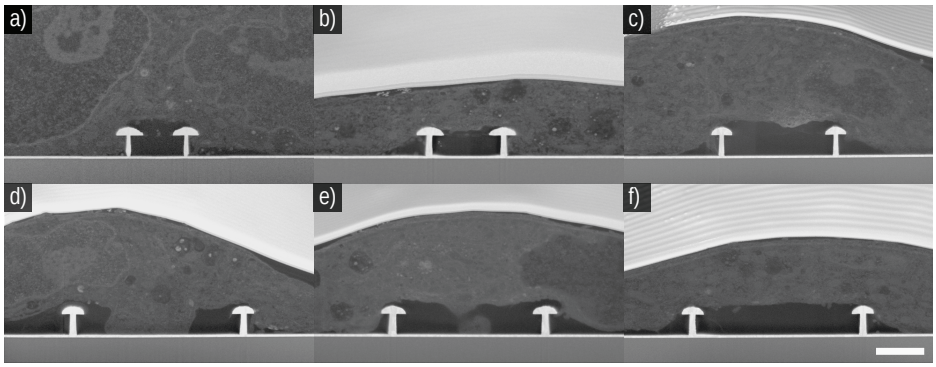

Figure 3.26: Focused ion-beam sections of HL-1 cells on big hollow mushrooms. (a) 2 µm structure with 1.2 µm opening, (b) 3 µm structure with 1.9 µm opening, (c) 5 µm structure with 3.9 µm opening, (d)-(f) 7.5 µm structures with (d) 6.2 µm, (e) 5.3 µm, and (f) 6.2 µm opening. Even with these large structures, cellular protrusion is not observed with high reproducibility. Differences between the theoretical and observed opening size result from cuts that are not at the exact center of the structure and thus not at its widest point. Scalebar represents 2 µm.

Despite the large opening size, cellular protrusion was not observed with high fidelity. While few cases of cell-substrate contact could be observed for structures of 7.5 µm in diameter, other 7.5 µm structures showed a clear spanning of the cell over the opening. On smaller structures, only slight bending could be observed. This raises the question why the results obtained here are fundamentally different from the ones reported by Lin *et al.*,[50] especially considering the significantly larger structures employed here. While the employed material is different, which could result in changes in the adsorption of the protein coating and thus different biochemical cues, another possibility are differences in the employed cell cultures. While HL-1 cells can be cultured over long periods of time while maintaining their cardiomyocyte-like characteristics, mutations will change the genetic information of the cell stock over time, resulting in differences in cellular behavior in different labs even when employing a cell line originally stemming from the same source. Furthermore, since HL-1 cells are cardiomyocyte-like and thus show spontaneous contractions, they exhibit fairly strong mechanical characteristics, which is counterproductive to the sharp bending and cytoskeletal deformation needed to protrude into small openings. Further studies were thus performed employing embryonic rat cortical neurons.

3.2.3 Neuronal culture on 3D structures

Neural tissue exhibits the softest mechanical characteristics in the body, with a Young's modulus of around 0.2 kPa for embryonic rat cortical neurons.[126] Therefore, significant differences can be expected for the interaction of neuronal cells with 3D structures as compared to the mechanically tough HL-1 cells with an elastic modulus of around 1.6 kPa.[127] Prior to cell seeding, 3D structure-containing samples were coated with poly-L-lysine (PLL). PLL is a positively charged polymer that has been shown to facilitate the adhesion of neurons.[37] While the exact mechanism is unclear, it is thought to proceed via electrostatic interaction between the positively charged amino groups of the polymer and negatively charged proteoglycans of the cell membrane,[37] since the neuronal surface has been shown to exhibit many glycoproteins with anionic groups.[128] For the preparation of cell-adhesive surfaces, PLL is most commonly physisorbed onto the sample by incubation with a PLL-containing solution. An approach often employed in our lab is incubation with a 0.01 mg/ml solution of PLL in Hank's balanced salt solution (HBSS). However, no viable cortical neurons were found on these substrates after three days *in vitro*, while very good viability was observed on glass coverslips treated with the same coating solution. It was hypothesized that this effect is due to different adsorption behavior of PLL on the different substrates. In order to investigate these differences, QCM-D measurements were performed. A QCM-D instrument is a quartz crystal microbalance with dissipation monitoring,[129] that enables the measurement of changes in the resonance frequency Δf of a quartz crystal due to an adsorbed mass. The frequency change and the change in mass Δm are directly proportional to one another. Their relationship is described by the Sauerbrey equation[129]

$$\Delta m = \frac{C_{QCM\text{-}D}}{n_h} \Delta f \tag{3.1}$$

where n_h is the harmonic number and $C_{QCM\text{-}D}$ is a characteristic parameter of the employed quartz crystal. In addition to the mass change, a QCM-D characterizes the viscoelastic properties of the formed layer due to the measurement of the decay of the oscillation after the driving power is switched off. This decay or dissipation is significantly higher for elastic layers than for rigid ones. In order to understand the differences in neuronal viability for different substrates coated with the same PLL solution, QCM-D measurements were performed with PLL on either gold or SiO_2 employing different buffers as well as ultrapure water (UPW) (Figure 3.27). For all measurements, PLL was diluted to 10 µg/ml in the respective buffers. As can be seen, the frequency shift increases

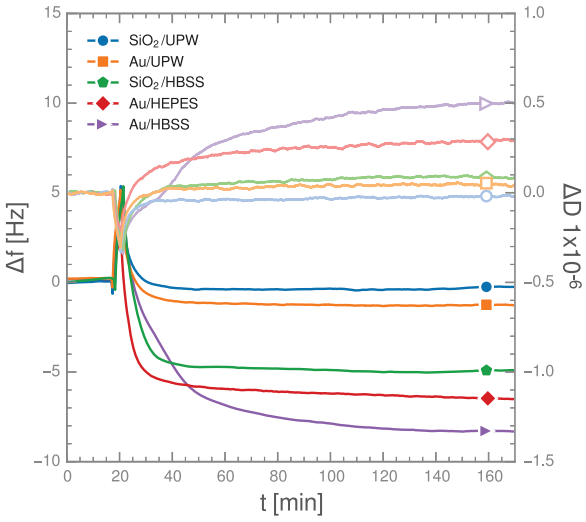

Figure 3.27: PLL in different buffers on SiO_2 and Au. Both, frequency shift Δf and dissipation ΔD, increase from SiO_2/ultrapure water to Au/ultrapure water, SiO_2/HBSS, Au/20 mM HEPES and finally Au/HBSS. For equal buffers, the adsorption of PLL is thus always stronger on gold than on silicon dioxide. Coating with PLL in HBSS on gold results in the highest frequency shift and dissipation, suggesting that this combination yields the largest density of PLL on the surface. Closed symbols represent Δf, open symbols ΔD. All traces were smoothed with a moving average over a maximum of 165 s to enable a better visualization.

from SiO_2/ultrapure water to gold/ultrapure water, to SiO_2/HBSS, to gold/20 mM HEPES, and finally to gold/HBSS, suggesting that coating gold with PLL in HBSS results in a significantly higher surface coverage than employing the same coating on SiO_2. In accordance with the results for the frequency change, the dissipation increases in the same order, hinting at much thicker, more extended PLL layers on gold when employing HBSS as buffer for the coating. A higher degree of PLL deposition with increasing ionic strength is to be expected due to a decrease in Debye length and thus reduced electrostatic repulsion between the positive charges of the polymer. The amount of PLL adsorbed on the surface can thus be tailored by changing the ionic strength of the buffer. The question remains why the higher amount of PLL results in a significant reduction in cell viability. While PLL is a staple of cell culture adhesion chemistry, with many groups reporting no toxic effects, various cell types have been shown to be adversely affected when treated with PLL-containing solutions,[130–132] with PLL strongly affecting the cell membrane, and potentially even inducing leakage of small moieties.[133] While PLL used for cell attachment is surface adsorbed, the physisorbed state is not highly stable and higher surface concentrations could result in a faster detachment of PLL molecules. Furthermore, the high surface charge of dense PLL layers could influence the neuronal behavior as could be shown by Michael *et al.*,[134] who observed a distinct sweet spot of neuronal viability with respect to the presented positive surface charge. The amount of PLL on the surface thus needs to be carefully tailored.

A focus for future studies is the specific functionalization of the 3D structures by exploitation of the strong biorecognition between biotin and avidin. Avidin is a positively charged, tetrameric glycoprotein that shows unspecific adsorption to surfaces, promotes cell adhesion due to its positive charge,[135] and can bind up to four biotin molecules.[66,135] The avidin-biotin affinity of $K_a = 10^{15}\ M^{-1}$ is the strongest non-covalent interaction known between protein and ligand.[131,136] Using biotinylated giant unilammelar vesicles linked to a biotinylated supported lipid bilayer via neutravidin, Fenz *et al.*[137] could achieve a very small intermembrane distance of just 7 nm. Exploiting this approach to facilitate close contact between cell and electrode by specific surface-attachment of fusogenic liposomes as introduced by Czsiar *et al.*,[138] followed by fusion with the cellular membrane could result in a significantly improved cell-chip coupling. Therefore, it was investigated whether avidin can be physisorbed to gold. Additionally, in order to be able to tailor the amount of avidin available on the surface, a mixture of PLL and avidin was studied. All solutions were prepared in 20 mM HEPES at pH 7.5 with concentration of either 10 µg/ml PLL, 125 µg/ml avidin, or a mixture containing 7.5 µg/ml PLL and 31.25 µg/ml avidin. Figure 3.28 shows the results obtained from this study. While PLL results in a small frequency shift that quickly stabilizes, the mixture of

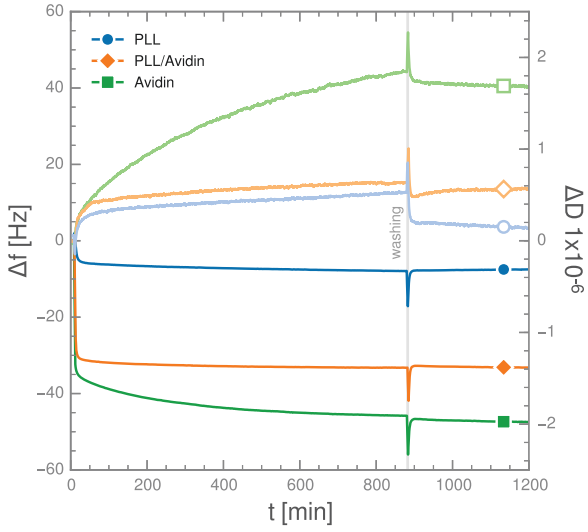

Figure 3.28: Different coating proteins incubated in 20 mM HEPES on gold. PLL quickly saturates at a low frequency shift Δf and dissipation ΔD, as does the mixture of PLL and avidin, though at higher frequency shift and slightly higher dissipation. Avidin, however, continues to be adsorbed on the surface, with increasing frequency shift up to 900 min, when the coating solution was washed off with HEPES for all QCM chambers. After washing, the dissipation decreases for all coating proteins, suggesting a reorganization on the surface. Closed symbols represent Δf, open symbols ΔD. All traces were smoothed with a moving average over a maximum of 165 s to enable a better visualization.

PLL and avidin results in a significantly higher frequency change. In contrast to coatings containing only avidin, however, the mixture quickly reaches saturation, suggesting that no further adsorption

takes place and the surface coverage remains stable. Avidin, on the other hand, continues to adsorb, with the frequency change continuing to increase up to 900 min into the experiment, when the analyte was removed and the chamber was washed with HEPES. Avidin thus does not seem to form stable monolayers. After washing, the frequency shift remained fairly stable for all solutions while the dissipation decreased slightly, which could suggest a reorganization of the coatings to form more compact layers.

In the next step, the different coatings were investigated with respect to their capability to support neuronal growth. As has been stated before, coating with PLL in HBSS results in rapid cell death, necessitating the investigation into alternative approaches. Silicon samples exhibiting a 50 nm gold layer were either coated with PLL in ultrapure water or 20 mM HEPES, avidin in HEPES or a mixture of avidin and PLL in HEPES, employing the same concentrations as used for the QCM-D studies. Additionally, gold samples were first modified with a self-assembled monolayer of 11-mercapto-1-undecanol (MUD) in order to establish a defined surface, followed by coating with the different cell adhesion molecules (CAMs) in HEPES. Glass coverslips were taken as control. The samples were stained for live and dead cells with calcein-AM and ethidium homodimer-1 after 3, 7, and 14 days *in vitro*. Figure 3.29 shows the results obtained for the different combinations of substrate, CAM, and employed buffer. While coating with PLL in HEPES yields good cell adhesion and viability on all samples (glass, gold, and gold coated with MUD) up to at least two weeks in culture, coating gold with PLL in ultrapure water (UPW) results in the formation of satellite cells at time points past 3 DIV. Satellite cells are formed if the intercellular force exceeds the cell-substrate adhesion force, suggesting either poor interaction between cell and CAM, between CAM and substrate, or insufficient coverage of the substrate with the cell adhesion molecules and thus insufficient cell-substrate adhesion. Since the neurons grow nicely on substrates coated with PLL in HEPES and the adhesion strength of PLL in neuronal culture medium is independent of the buffer employed for the coating step, it can be concluded that the low PLL density obtained by coating in ultrapure water as proven by QCM-D experiments is not sufficient to ensure good adhesion. All substrates coated with avidin alone exhibit different levels of satellite formation at 7 DIV and pronounced satellites at 14 DIV, with many areas entirely exempt of cells. This could either be due to the thick coatings formed on the surface as shown by QCM-D being instable, due to insufficient cell adhesion to avidin in general, or a combination hereof. Mixtures of PLL and avidin, on the other hand, result in good adhesion

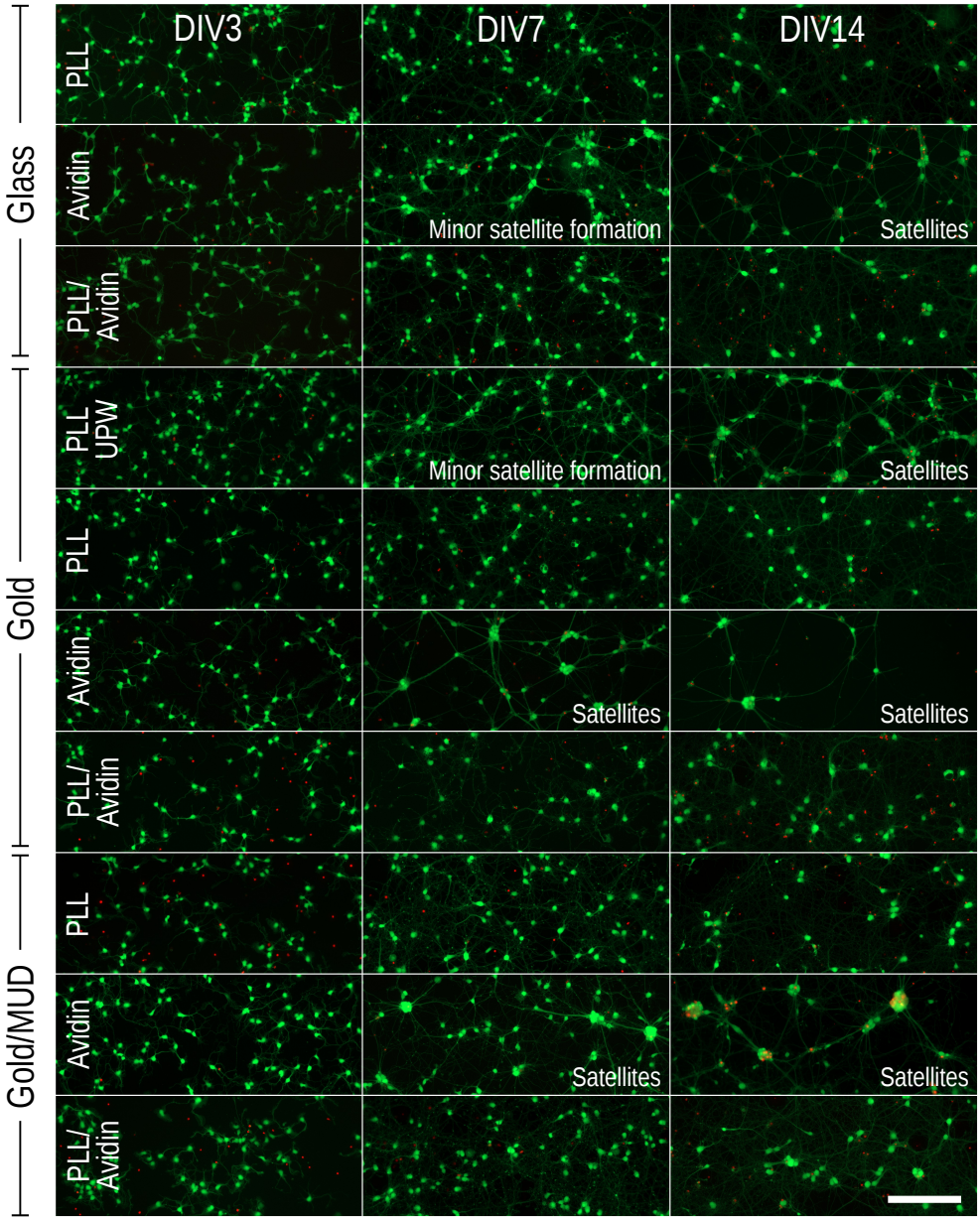

Figure 3.29: Live/dead staining of rat cortical neurons on different substrates and cell adhesion molecules. While coating with PLL in HEPES or mixtures of PLL and avidin yields good cell adhesion and viability on all substrates, both PLL in ultrapure water (UPW) and avidin result in the formation of satellite cells. Scalebar represents 200 µm.

and viability on all substrates. While these data generally provide sufficient information on possible coatings allowing for the culture of cortical neurons on gold, significant variations between gold-on-silicon samples obtained from the cleanroom make the establishment of a reproducible process challenging. For five different sample batches obtained, only two exhibited good neuron survival in accordance with the results obtained in Figure 3.29. On two batches, no adequate coating could be found, with a variety of different CAMs tested all resulting in cell death. One batch showed sample-dependent behavior, with some samples showing adequate cell survival, while others showed poor cell viability. Head-to-head experiments with different sample batches and glass controls were performed to exclude the influence of culture variations or experimental error. While the cell viability was good both on 'good' samples and the glass control, none of the different coatings tested resulted in cell survival on the 'bad' sample batch. Energy-dispersive x-ray (EDX) spectroscopy was employed to investigate the samples not supporting cell growth to test for detrimental contaminants. However, no toxic components could be found within the detection limits of the instrument. Subsequently, two samples, one supporting cell growth and one not supporting cell growth, were analyzed via secondary ion mass spectrometry (SIMS). Again, no significant difference was observable. While the concentrations of oxygen and fluorine were marginally different within the gold layer, more data is needed to draw conclusions. The lack of toxic compounds is in accordance with the fact that bare silicon areas around the periphery of the samples generally exhibited good cell survival, even on samples where all cells on gold were dead. While earlier sample batches received proved better for the structural preservation during the electrodeposition of 3D designs, no such trend could be observed with respect to the neuron viability, with bad batches received at seemingly random intervals. While surface roughness seems to be an important aspect for the occurrence of good structural preservation (see Figure 3.17), no significant differences in surface topography could be observed between sample batches supporting and precluding cell growth. The sample fabrication thus seems to be a fundamental limitation for the application of these structures, raising a strong need for an in-depth investigation into the underlying problems of the electron-beam evaporation process in the future.

In order to enable a specific functionalization in future experiments, neurons were seeded onto 3D gold structures coated with a mixture of PLL and avidin. Pre-coating with MUD was performed to receive a more stable interface. The neurons were fixed at 3 DIV, stained with osmium tetroxide

and uranyl acetate and embedded in epoxy resin. In order to increase the chance of neuronal protrusion into the structures, hollow pillars of 600 nm and 800 nm stalk width were chosen for this study since they exhibit a larger opening size than hollow mushrooms. Figure 3.30 shows exemplary FIB sections. As was observed for HL-1 cells, some cells tightly engulf the structures

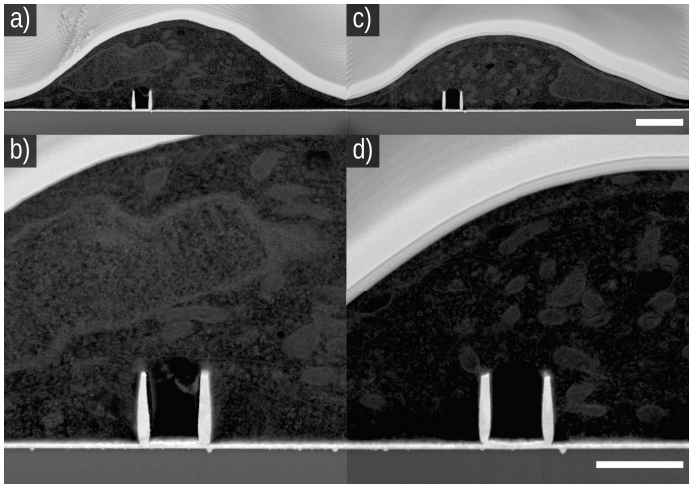

Figure 3.30: Focused ion-beam sections of rat cortical neurons on hollow pillars of 800 nm stalk width. The cells either tightly engulf hollow pillars (a,b) or detach around the base (c,d). In all cases, the cells bend away from the hollow opening. The bright spots inside the structure in (d) are most likely due to platinum redeposition. Scalebars represent 2 µm (top row) and 1 µm (bottom row).

(Figure 3.30 a,b), while others only form a tight contact around the upper part of the sidewall, while bending away from the base (Figure 3.30 c,d). For 800 nm structures, 2/3 of the cells were found to be partially attached and 1/3 fully engulfed (n=9). In contrast to HL-1 cells, however, the neurons do not only prefer to not bend into the openings, but actively adapt a convex membrane conformation around the top of the structures. The same effect was observed on structures of 600 nm in diameter. The low number of sectioned cells, however, precludes any conclusion towards the ratio of fully engulfed to partially attached cells in this case. The reason for the small number of available sections is two-fold. First, in contrast to the very large HL-1 cells that can easily achieve several tens of microns in diameter, embryonic rat cortical neurons exhibit a soma of around 13 µm in diameter, making a direct placement on top of an approximately 1 µm diameter structure significantly less likely than for HL-1 cells. This results in only few interactions to be analyzed per sample unless very high cell counts are employed. Second, the resin embedding process poses several challenges, resulting in low sample output: On the one hand, excessive removal of the resin results in very porous cells, comparable to the ones obtained via CPD. Insufficient removal of the resin, on the other hand, makes an investigation via electron microscopy impossible since no localization of cells

and structures is possible. The sweet-spot between insufficient and excessive removal of the resin is, so far, difficult to achieve experimentally, resulting in a significant amount of unusable samples. Due to these issues, no FIB cuts of neurons on big hollow structures can be presented here. In future studies, employing a higher cell number in conjunction with optimized parameters for the resin embedding process should improve the yield of analyzable structures.

Irrespective of the experimental challenges encountered with neurons on 3D structures, the fact remains that despite what literature suggests,[50] no protrusion into the interior of hollow samples can be observed, even with the soft neuronal cells. One potential problem causing this effect could be the necessity to remove either liquid or even gas bubbles from the interior of the structure, which could oppose cellular protrusion into the opening. However, with most structures being entirely filled with resin during focused ion-beam sectioning, it can be expected that this is not a major concern. Another aspect is the question of the deformation energy cost $E_{bending}$. Generally, a membrane engulfs an object if the adhesion energy gained exceeds the deformation energy cost. The bending energy of a membrane can be described as the integral over the membrane area $S_{membrane}$ [49,139]

$$E_{bending} = 2\kappa \int_S dS_{membrane} H^2 \tag{3.2}$$

where κ is the membrane's bending rigidity and H is the mean curvature, with $H = (c_1+c_2)/2$. Here, c_1 and c_2 are the minimal and maximal curvature, or principal curvatures, at each point of the membrane.[139] In order for the membrane to engulf an object, this energy term has to be smaller than the adhesion energy, $E_{adhesion}$, which is defined as

$$E_{adhesion} = w \int_{S_{ad}} dS_{membrane} \tag{3.3}$$

where w is the adhesion strength between the object and the membrane and S_{ad} is their contact area.[49,139,140] Considering a hollow pillar, cellular protrusion into the interior of the structure would result in a significant overall increase in membrane curvature, with both the area on top of the sidewalls as well the area inside the hollow experiencing a much higher curvature than what would be expected for a tightly engulfed solid pillar. Therefore, protrusion into a hollow structure is expected to result in a strong increase in deformation energy as compared to the interaction with solid pillars. In order for this process to be energetically favorable, the increase in adhesion

energy has to be higher than the energy loss resulting from the deformation. Considering that the interaction area is actually less than for a solid pillar in the case of a slight bending into the interior (Figure 3.31), it is no entirely surprising that the deformation energy cost seems to exceed the adhesion energy.

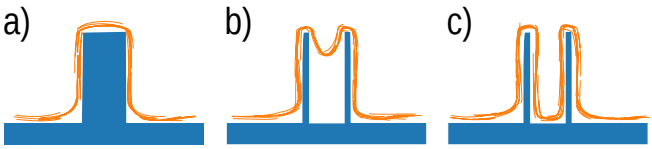

Figure 3.31: Engulfment of a solid pillar (a) as well as bending (b) and full protrusion (c) into a hollow mushroom. S_{ad} decreases from (a) to (b) but increases from (a,b) to (c).

While a full protrusion would increase the interaction area, the deformation energy cost can be expected to be significant in this case. However, for a full description of the system, additional parameters need to be included such as cytoskeletal influences. Furthermore, information is needed on the actual characteristics for both neurons and HL-1 cells with respect to these parameters to enable a better evaluation of the different behavior of these cells. In either case, the development of a mathematical model and subsequent simulation of the system could provide valuable information towards elucidating the geometrical parameters necessary to induce cellular protrusion.

3.3 Conclusion

Within this Chapter, solid pillars and mushrooms as well as hollow pillars and mushrooms of various sizes were made available through a common fabrication scheme, thereby facilitating a parallel production of the different 3D designs. Through the downscaling of the deposition process, it became possible to monitor the nanoscale characteristics of the structures by observation of changes in the recorded galvanization current. Some challenges remain due to differences in the received substrates, resulting in discrepancies in the stability of the produced PMMA templates. These changes in the characteristics of the underlying substrate also influence the viability of cultured neurons, though the exact cause of poor cell viability on some of the sample batches could neither be determined nor circumvented, despite extensive studies into possible reasons and different potential coatings. Focused ion-beam sectioning showed good engulfment of the fabricated 3D structures both by HL-1 cells and embryonic rat cortical neurons. However, in contrast to the expectations resulting from a report of pronounced cellular protrusion into hollow structures,[50] only a slight

bending into the opening can be observed for HL-1 cells on hollow pillars of 800 nm in diameter, while cortical neurons actively bend away from the opening. Even for large openings of several micrometers in diameter, cellular protrusion of HL-1 cells could not be observed with high fidelity. Experiments with cortical neurons on big hollow structures are pending, their behavior on structures with larger opening thus remains to be determined. Due to the discrepancies between the experimental results and the reports in the literature, the development of a mathematical model and subsequent simulation of the system would be a valuable approach to shed light on the question of cellular protrusion into hollow structures.

Chapter 4

3D Structures on Microelectrode arrays

An increasingly important aspect of 3D nanoelectrode fabrication is good control over the resulting structure size. As was previously demonstrated,[49,56] cellular engulfment of 3D structures is highly dependent on the overall size and aspect ratio of the 3D electrode. However, while the obtained results proved the importance of the structure size and the validity of the 3D approach for the investigation of electrogenic cells, little is reported on the **direct comparison** of different 3D structures. While many designs have been proposed in the literature, the conducted experiments differ in fundamental parameters such as the overall size of the electrode, the type and size of the 3D structure, the electrode material, or the number of 3D structures per electrode, all of which preclude a direct comparison of the results with respect to the improvement yielded by application of 3D structures. In order to solve this problem, multiple different structures with respect to both design and size have to be fabricated on a single chip. This, however, is only possible if sets of few nanoelectrodes can be produced in a well-controlled and clearly-defined manner, thereby facilitating a rapid-prototyping approach to 3D electrodes. As has been demonstrated in Chapter 3, the process developed within this body of work enables the fabrication of the common 3D structures as reported in the literature - gold nanomushrooms as introduced by Spira,[46] gold pillars, and hollow structures as employed in the Cui lab,[50] as well as hollow nanomushrooms as novel 3D design - all within one fabrication scheme. In order to prepare multiple different structures on a single chip, the bulk fabrication process developed in Chapter 3 has to be adapted for the fabrication of few nanoelectrodes at a time. This Chapter is thus concerned with the establishment and characterization of the electrodeposition process of 64, eight or just a single nanoelectrode. Subsequently, the capabilities of the developed microelectrode arrays (MEAs) are tested with re-

spect to the influence on the recording capabilities yielded by the different 3D designs, employing cardiomyocyte-like HL-1 cells as model system.

Excerpts of this Chapter have been published in Nanotechnology, Volume 28, Number 9 (2017), S. Weidlich *et al.* 'MEAs and 3D nanoelectrodes: electrodeposition as tool for a precisely controlled nanofabrication'.[116]

4.1 Experimental

4.1.1 MEA fabrication

MEAs were produced in an ISO 1 cleanroom[117] on n-doped silicon wafers (Si-Mat Silicon Materials, Kaufering, Germany) exhibiting a 1 µm silicon dioxide layer. Figure 4.1 schematically depicts the different steps of the fabrication process. Feedlines were defined via photolithography using a double resist system (LOR 3b, Microchem, Newton, USA and AZ nLOF 2020, MicroChemicals, Ulm, Germany). To achieve feedlines that are level with the surrounding oxide, the structure was transferred into the underlying silicon dioxide by reactive ion etching (RIE) (Oxford Instruments, Abingdon, U.K.) with a $CHF_3/CF_4/Ar/O_2$ gas mixture, followed by electron-beam evaporation of Ti, Au, and Ti (7 nm, 145 nm, and 5 nm, respectively) (Pfeiffer PLS 570, Pfeiffer Vacuum, Asslar, Germany) with subsequent lift-off. In the center of the array, the width of the feedlines is 20 µm, with the 64 electrodes arranged in an 8x8 grid of 200 µm spacing. The MEAs were passivated with an 800 nm overall stack of alternating SiO_2 (200 nm) and Si_3N_4 (100 nm) layers (ONONO) via plasma-enhanced chemical vapor deposition (PECVD) (Sentech, SENTECH Instruments GmbH, Berlin, Germany). In a second photolithography step, the bond pad openings and 12 µm or 24 µm apertures on the electrodes were defined and the passivation selectively removed via RIE using a $CHF_3/CF_4/Ar/O_2$ gas mixture. The processed wafers were diced into individual 24x24 mm^2 chips (9 chips/wafer). The MEAs were subsequently cleaned in acetone and isopropanol for 5 min under ultrasonication and dried in a stream of nitrogen. They were dehydrated at 200°C for 30 min, followed by spincoating of poly(methyl methacrylate) (PMMA) (AR-P 669.07, Allresist, Strausberg, Germany) at 500 rpm with an acceleration of 100 rpm/s for 5 s, immediately followed by 2000 rpm with an acceleration of 500 rpm/s for 35 s. The MEAs were then tempered on a 120°C, 180°C, and 120°C hotplate for 2, 5, and 2 min, respectively. Structures were transferred into the PMMA employing a Vistec EBPG

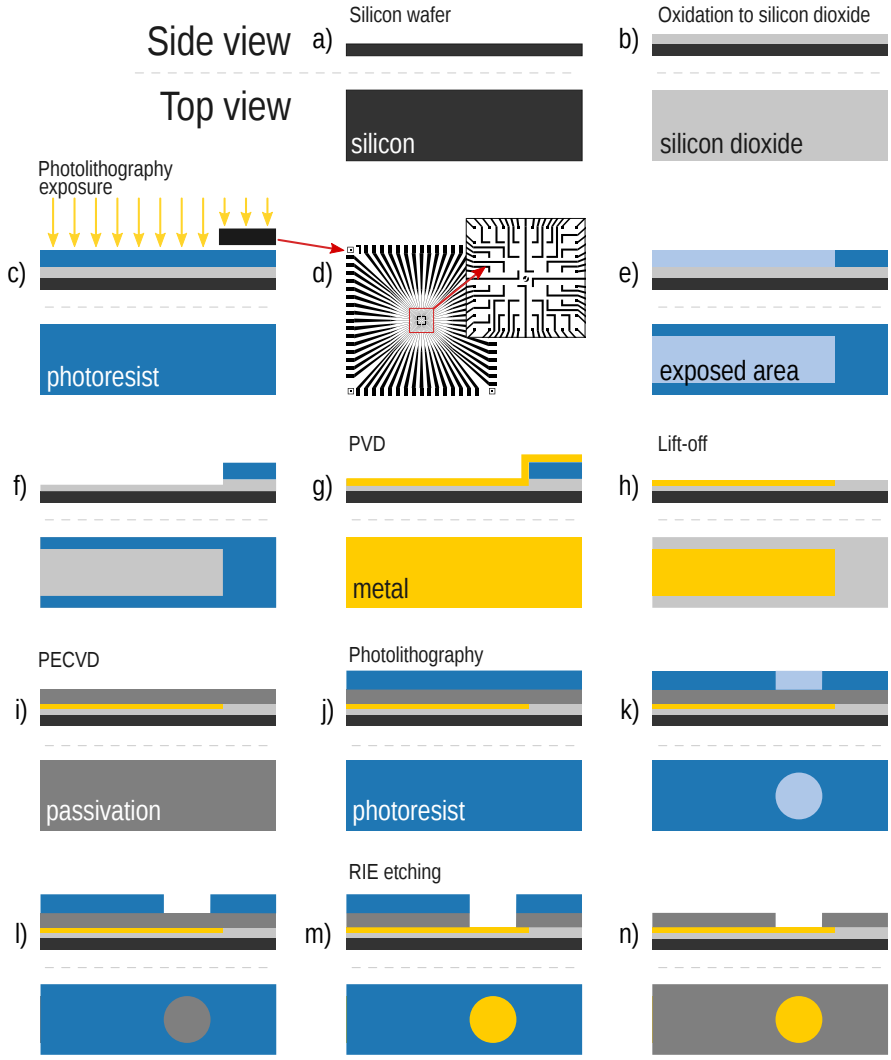

Figure 4.1: MEA fabrication: The surface of a silicon wafer (a) is oxidized to an insulating layer of silicon dioxide (b), MEAs are defined via photolithography (c-e) followed by development of the exposed areas and RIE etching to transfer the structure into the underlying oxide (f). Metal is deposited onto the sample via physical vapor deposition (PVD) (g), subsequent lift-off defines the metal feedlines (h). The surface is passivated with an insulating layer via plasma-enhanced chemical vapor deposition (PECVD) (i). Apertures enabling the interaction with the environment are then defined via photolithography (j-l), RIE etching (m), and subsequent photoresist removal, yielding the final device (n). Mask depicted in (d) shows the entire 64 electrode layout, while the remaining Figure illustrates the fabrication scheme for a single, exemplary electrode. Figure adapted from [141]

5000plus HS (Vistec Electron Beam GmbH, Jena, Germany) electron-beam lithography system.

1. **MEA type (A) Solid and hollow structures (12 µm apertures):** The upper four rows of electrodes (32 electrodes) were each structured with a ring of 800 nm in outer diameter and 25 nm ring thickness with a dosis of 1400 µC/cm^2. The lower four rows of electrodes (32 electrodes) were each structured with a circle of 800 nm in diameter with a dosis of 350 µC/cm^2. All structures were defined with a resolution of 2 nm, beam current of 100 pA, automatic sequencing, and without proximity correction.

2. **MEA type (B) Solid structures (12 µm apertures):** The upper two rows of electrodes (16 electrodes) were each structured with a circle of 300 nm in diameter with a dosis of 402.5 µC/cm^2, the electrodes in rows three and four (16 electrodes) were each structured with a circle of 600 nm in diameter with a dosis of 350 µC/cm^2, the electrodes in rows five, six, and seven (24 electrodes) were each structured with a circle of 800 nm in diameter with a dosis of 350 µC/cm^2, and in row eight with four circles of 800 nm in diameter arranged in a 2x2 square of 4 µm spacing with a dosis of 350 µC/cm^2. All structures were written with a resolution of 2 nm, beam current of 500 pA, automatic sequencing, and without proximity correction.

3. **MEA type (C) Big hollow structures (24 µm apertures):** The upper two rows of electrodes (16 electrodes) were each structured with a ring of 1 µm in outer diameter and 25 nm ring thickness with a dosis of 1400 µC/cm^2. The electrodes in rows three and four (16 electrodes) were each structured with a ring of 2 µm in outer diameter and 50 nm ring thickness with a dosis of 750 µC/cm^2. The electrodes in rows five and six (16 electrodes) were each structured with a ring of 3 µm in outer diameter and 50 nm ring thickness with a dosis of 750 µC/cm^2. The electrodes in rows seven and eight (16 electrodes) were each structured with a ring of 5 µm in outer diameter and 100 nm ring thickness with a dosis of 550 µC/cm^2. All structures were written with a resolution of 2 nm, beam current of 100 pA, automatic sequencing, and without proximity correction.

Development of the structures was performed by immersion into AR 600-55 (Allresist, Strausberg, Germany) for 220 s at room temperature, followed by immersion into isopropanol and deionized

water for 1 min each. The MEAs were dried in a stream of nitrogen. Glass rings (14 mm outer diameter, 1 mm wall thickness, and 10 mm height) were glued onto each MEA using a two-component epoxy resin (EPO-TEK 302-3M 8OZ Kit, Epoxy Technology, Billerica, USA) and cured at 65°C for 3 h. The MEAs were then placed into a custom-made chip holder as depicted in Figure 4.2.

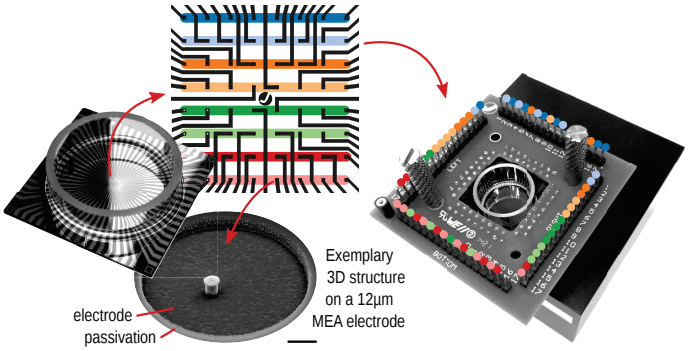

Figure 4.2: 64 electrode MEA and chip holder for contacting the different electrodes. In this manner, each electrode in the 8x8 grid can be addressed individually. In most cases, all electrodes in one row were shorted for the experiments conducted here, as depicted by the different colors. In this manner, a single 3D structure is fabricated on each electrode. SEM scalebar represents 2 µm.

700 µl gold bath solution (Pur-A-Gold 202B, Enthone, Langenfeld, Germany containing 12 g/l Au from $KAuCN_2$ (99.9% metal basis), Alfa Aesar, Karlsruhe, Germany) were filled into the ring and pipetted up and down at least 15 times to ensure penetration into the template. Electrodeposition was performed on a Biologic VSP-300 (Bio-Logic SAS, Claix, France) potentiostat using a three-electrode configuration with the MEA electrodes as working, a Pt mesh as counter, and a Ag/AgCl pellet as reference electrode. In early experiments, the current was recorded with a 20 Hz sampling rate and a 50 kHz low-pass filter. Later, the current was recorded with a 4 Hz sampling rate and 5 Hz low-pass filter. Initially, all 64 electrodes of MEAs exhibiting both hollow and solid templates (MEA type A) were galvanized in parallel for the establishment of adequate parameters, with depositions performed applying a first step of 5 s at either -1.25 V, -1.30 V, -1.35 V, or -1.40 V, followed by a second step at -1.10 V. Afterwards, all 8 electrodes of one row were galvanized in parallel for all templates reported here (MEA types A through C). As before, electrodeposition was performed employing a two-step process with a first step at a potential of -1.35 V versus reference for 5 s, followed by application of -1.1 V for various times to prepare structures of different sizes. After electrodeposition, the gold bath solution was removed, the chips washed with MilliQ water thrice and placed into acetone for PMMA removal. The acetone was exchanged twice to ensure full removal. The chips were dried in a stream of nitrogen and imaged at a LEO 1550 (Carl Zeiss AG,

Oberkochen, Germany) scanning electron microscope at 20 kV acceleration voltage using inlens detection. The height of the resulting structures was determined by laser scanning profilometry (Keyence VK-X100, KEYENCE Deutschland GmbH, Neu-Isenburg, Germany) at 50x magnification. A self-developed Python program was employed for the post-processing of the current traces acquired during electrodeposition. The data was smoothed twice with a third order polynomial Savitzky-Golay filter at a window size of 23, which corresponds to a time window of 5.75 s. The minimum of the second order derivative was determined as time at which the boundary of the template ($t_{boundary}$) was reached. Furthermore, a manual determination of $t_{boundary}$ was performed using the Biologic EC-Lab V10.40 software, enlarging the area of the bend in the current in the raw data and picking $t_{boundary}$ as the timepoint in the center of the bend. The analysis of SEM images was performed using ImageJ. The scaling information was extracted from SEM images using the Tiff Tags plug-in developed by Joachim Wesner in conjunction with the SetScaleFromTiffTag macro. The particle analysis tool was employed to determine the size of the structures from the SEM images. All data points for the outer radius represent at least 6 electrodes and all data points for the inner radius at least 5 electrodes and were averaged from both the minimal and maximal size data from the ImageJ Particle Analysis Tool for all respective electrodes.

4.1.2 Cell culture

Prior to cell culture, all chips were consecutively cleaned in acetone (Merck KGaA, Darmstadt, Germany), isopropanol (Merck KGaA, Darmstadt, Germany), and ultrapure water for at least 10 min each. In cases where PMMA residues were present on the chip, the cleaning cascade was preceded by incubation with AR 600-71 (Allresist, Strausberg, Germany) for at least 1 h. If this step was not sufficient, the chips were O_2 plasma cleaned at 0.2 mbar and 200 W for 10 min (Pico low-pressure plasma system, Diener electronic, Bielefeld, Germany). Afterwards, rings of 9 mm in outer diameter, 7 mm in inner diameter, and either 1 or 2 mm in height were glued around the center of the chips using a two-component epoxy resin (EPO-TEK 302-3M 8OZ Kit, Epoxy Technology, Billerica, USA) and cured on a 100°C hotplate for 1 h. Subsequently, rings of 17 mm in outer diameter, 15 mm in inner diameter, and 10 mm height were glued onto the chips using the same procedure. Afterwards, the area between the two rings was covered with epoxy to protect the passivation layer and again cured at 100°C for 1 h. The chips were sterilized by incubation with 70% ethanol, transferred to a sterile hood, and rinsed with sterile, ultrapure water thrice. They were coated with

2.5 µg/cm^2 fibronectin from bovine plasma (Sigma-Aldrich, Schnelldorf, Germany) in PBS without calcium and magnesium (Life Technologies GmbH, Darmstadt, Germany) for one hour at 37°C, followed by washing with medium once, right before cell seeding. If poor cell adhesion was observed with this method, the chips were dehydrated on a 120°C hotplate for 1 h, followed by silanization with (3-aminopropyl)triethoxysilane (APTES) (Sigma-Aldrich, Steinheim, Germany) at reduced pressure for about 2 h, prior to sterilization and fibronectin coating. Cardiomyocyte-like HL-1 cells were maintained in T-25 culture flasks in Claycomb medium (Sigma-Aldrich, Steinheim, Germany) supplemented with 10 vol% fetal bovine serum (FBS) (Life Technologies GmbH, Darmstadt, Germany), 100 µg/ml penicillin-streptomycin (Life Technologies GmbH, Darmstadt, Germany), 0.1 mM (±)-norepinephrine (+)-bitartrate salt (Noradrenaline) (Sigma-Aldrich, Steinheim, Germany) and 2 mM L-glutamine (Life Technologies GmbH, Darmstadt, Germany) in a humidified incubator at 37°C and 5% CO_2. The media was exchanged for 5 ml fresh, pre-warmed, supplemented Claycomb media daily. Once confluency was reached and mechanical contraction was visible, adherent HL-1 cells were washed with 0.05% trypsin-EDTA (1 ml) (Life Technologies GmbH, Darmstadt, Germany) once and detached by incubation with 0.05% trypsin-EDTA (1 ml) at 37°C for 3 to 5 min. Trypsin digestion was then inhibited by addition of supplemented Claycomb medium (5 ml) and the cells were sedimented by centrifugation at 200 rcf (relative centrifugal force) for 3 min. The supernatant was aspirated, the cells resuspended in pre-warmed, supplemented Claycomb medium (1-4 ml), and diluted to appropriate densities to achieve confluency within two to three days. 50 µl of the cell suspension were seeded into the small ring in the center of the chips. The cells were left to adhere in a humidified incubator at 37°C and 5% CO_2 for 30 min. Afterwards, each chip was topped-up with supplemented Claycomb medium so as to fill the larger ring. The media was exchanged daily. Once the confluent cell layer was beating, action potentials were recorded employing a 64 channel MEA amplifier system developed in-house. The system consists of a headstage or pre-amplifier, connected to a main amplifier which is then connected to the controlling PC via a high-resolution analog-to-digital converter (ADC) (USB-6255, National Instruments, Austin, Texas, USA). The headstage holds the MEA chip and provides an amplification of 10.1 at an effective input impedance of 1 GΩ. The main amplifier can provide a gain of either 1 (non-amplified), 10 or 100, and was operated at a nominal gain of 100 for all measurements, yielding a total amplification of 1010.[142] Data acquisition is controlled through a LabView software (National Instruments, Austin, USA) developed in-house, which enables the definition of the recording parameters such as gain and filter settings.

The effective bandwidth was limited with a high pass filter (AC coupling) and a low pass filter (high frequency cutoff) from 1 Hz to 3 kHz for all measurements reported here. All 64 channels were read out in parallel at a sampling rate of 10 kHz per channel. Additionally, electroporation pulses were applied to all 64 electrodes simultaneously to facilitate intracellular recording of cardiac action potentials. The electroporation protocol consists of 100 consecutive square biphasic pulses, delivered with a frequency of 1250 Hz and thus period of 800 µs, and amplitude of 1 V. Recording was resumed 30 to 60 s after electroporation to prevent ADC overload. Afterwards, the chips were cleaned by incubation with 0.05% trypsin-EDTA (1 ml) at 37°C for 10 min, followed by a second step for at least 30 min, rinsed with ultrapure water, sterilized with ethanol, again rinsed with ultrapure water, and dried in a stream of nitrogen. If microscopic analysis showed cellular residues, the chips were cleaned with a 2% solution of Hellmanex III (Sigma-Aldrich, Steinheim, Germany) in ultrapure water for 30 min, followed by rinsing with water for at least 1.5 h. Afterwards, the chips were re-used for cell culture, starting with sterilization in 70% ethanol. The analysis of the recorded electrophysiological data was performed employing both the BioMAS Analyzer software developed by Fabian Brings, as well as a Python script developed by Johannes Lewen. All amplitude results are given as raw, unfiltered data and averaged over the amplitudes recorded within a timeframe of 60 s. For the electroporation-induced amplification, the highest amplitude recorded within the first minute after application of the voltage pulse is compared to the average amplitude for the unstimulated case.

4.2 Results

4.2.1 3D structures on microelectrode arrays

The structures developed in Chapter 3 were transfered onto microelectrode arrays to enable the recording of electrogenic activity from cardiomyocyte-like HL-1 cells. After MEA fabrication (Figure 4.1), the devices were processed according to the schemes presented in Figures 3.2 and 3.5, with each electrode exhibiting the template for one three-dimensional design unless indicated otherwise. Due to the limited cellular protrusion efficiency as shown in Chapter 3, only hollow pillars and mushrooms equal to or larger than 800 nm in diameter were employed on MEAs to provide a larger opening size than yielded by 600 nm structures. Initially, the upper four rows of the MEAs

were structured with hollow templates of 800 nm in diameter, while the lower four rows were structured with solid templates of 800 nm in diameter (MEA type A) to produce chips exhibiting the four structure types - hollow pillar, hollow mushroom, solid pillar, and solid mushroom - as depicted in Figure 4.3.

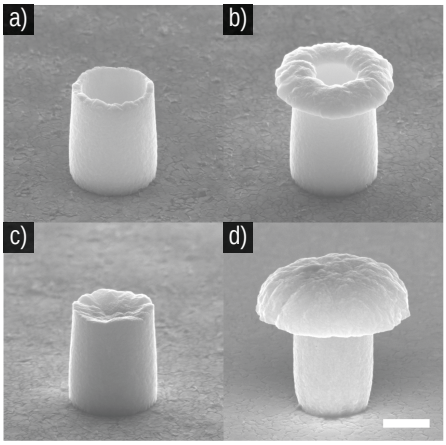

Figure 4.3: The types of 3D structures initially prepared on MEAs: hollow pillars (a) and hollow mushrooms (b) of 800 nm stalk diameter were prepared on the upper half of the 64 electrodes while solid pillars (c) and solid mushrooms (d) of 800 nm stalk diameter were prepared on the lower half. (a,b) were acquired at 55° sample tilt, (c,d) at 65° sample tilt. Scalebar represents 500 nm.

As has been stated before, the electrodeposition of 3D structures is often conducted by setting a specific current density and overall time. However, this has the drawback of being inherently sensitive to changes in the overall area. Therefore, for the deposition of only few nanoelectrodes, where even the failure of a single electrode signifies a large change in overall area, this can only be done in a stable manner when galvanizing the contact pads at the same time, thereby providing an overall area that is considerably larger than that of the nanostructure and only changes insignificantly should one of said nanoelectrodes be non-functional. This fact makes the application of a voltage-controlled approach even more critical for MEAs than it does for the bulk substrates in Chapter 3. By negating the need to galvanize the contact pads, it becomes feasible to down-size the process and, rather than shortcutting all the electrodes and performing the electrodeposition by full immersion into the plating bath as previously reported,[104] enable the deposition of individual nanoelectrodes. Nevertheless, for the establishment of the parameters and the determination of whether the employed measurement system exhibits the accuracy needed to record the small currents expected for the deposition of few nanostructures, all 64 electrodes were initially galvanized in parallel. The MEAs were placed into a custom-build chip holder (Figure 4.2) and all 64 pins addressing the different electrodes were connected to the potentiostat simultaneously. SEM anal-

ysis verified the presence of structures on 94% of the available electrodes with respect to hollow templates, and 87% with respect to the solid samples (n = 13 chips), proving that the electron-beam lithography parameters for bulk substrates are generally applicable for the preparation of 3D structures on MEAs. The reasons for electrodes failing to exhibit 3D structures are diverse: Local variations in PMMA thickness can necessitate a higher electron-beam dosis for full exposure down to the underlying gold, with an insufficient dosis resulting in PMMA residues passivating the metal surface and thus not allowing for the electrodeposition of gold. Similarly, a thin residual ONONO layer that was not entirely removed during RIE processing would yield the same effect. Therefore, missing structures are to be expected to some extend. Increasing the electron-beam dosis employed for solid templates could alleviate this problem in cases where the reason is residual PMMA, with only minor influence expected with respect to the structure size for a small increase in dosis. Globally increasing the dosis for hollow structures, however, would most likely have an adverse effect on the stability of the PMMA plug and thus the ratio of intact hollow designs, making missing structures the less significant issue.

As with the bulk substrates, the galvanization was initially performed at different potentials to determine optimal parameters for a high ratio of structurally intact 3D designs. In agreement with previous results, conducting the entire deposition at -1.10 V resulted in poor structural stability, with 94% of the structures deposited into hollow templates being solid and 6% exhibiting circular openings as seen in Figure 3.11 (f). Therefore, subsequent depositions were performed with the two-step deposition process proposed in Chapter 3. The potential for the first step was varied from -1.25 V, to -1.30 V, -1.35 V, and -1.40 V, while the time was kept constant at 5 s. The second step was performed at -1.10 V as previously reported. As can be seen in Figure 4.4, the distribution of structurally intact hollow 3D designs on MEAs of type (A) strongly depended on the potential applied in step 1, with a first step at either -1.25 V (n = 31 electrodes), -1.30 V (n = 83 electrodes), or -1.40 V (n = 62 electrodes) resulting in the preferential production of either solid structures or structures exhibiting a circular opening due to the outgrowth of the PMMA plug. Performing the first step at -1.35 V, however, resulted in the formation of hollow structures with high fidelity (n = 95 electrodes). Increasing the time of the first step to 10 s at a potential of -1.30 V did not improve the distribution, with 47% of the structures being solid and 47% exhibiting the artifact (n = 62 electrodes). Therefore, due to the good results obtained at -1.35 V, all subsequent depositions

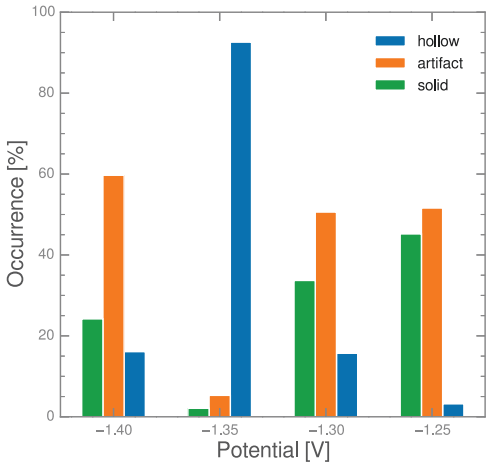

Figure 4.4: Allocation of the different structures resulting from hollow templates in dependence on the potential employed for the first step of the deposition. While a first step at either -1.25 V (n = 31 electrodes), -1.30 V (n = 83 electrodes), or -1.40 V (n = 62 electrodes) results in the preferential production of either solid structures or structures exhibiting a circular opening due to the outgrowth of the PMMA plug (artifact), performing the first step at -1.35 V (n = 95 electrodes) results in the formation of hollow structures with high fidelity.

were conducted employing this potential for the first step of the deposition.

In order to prepare different structures on a single chip, only 8 electrodes were galvanized in parallel in ensuing experiments. The deposition at -1.35 V for 5 s followed by a second step at -1.10 V resulted in the fabrication of hollow structures on 73% of the available electrodes, while 11% exhibited solid structures, and 11% circular artifacts owing to the outgrowth of the PMMA plug. No structures could be found on 4% of the electrodes structures with hollow templates (n = 24 chips). In the best case, 100% hollow structures could be found, while the worst chip exhibited only 28% hollow 3D electrodes, with 28% being solid, and 44% exhibiting the circular artifact. On all chips investigated, solid structures could be found on 89% of the electrodes structured with solid templates. The structures produced in this manner exhibited a stalk width of 905 ∼ 21 nm for solid pillars and a stalk width of 963 ∼ 14 nm and opening size of 629 ∼ 22 nm in diameter for hollow pillars, which is in good agreement with the results obtained on bulk samples as presented in Chapter 3. Figure 4.5 shows all 64 electrodes of an exemplary chip prepared in this manner (a), as well as one electrode from each line for two additional chips (b,c). In Figure 4.5 (a), hollow mushrooms of 1381 ∼ 56 nm and 1314 ∼ 41 nm in cap diameter were deposited in rows one and two, respectively, while rows three and four exhibit hollow pillars of 957 ∼ 10 nm and 970 ∼ 46 nm in diameter. Row five is structured with solid pillars of 889 ∼ 13 nm in diameter, and rows six through eight with solid mushrooms of increasing cap size with diameters of 1255 ∼ 27 nm, 1857 ∼ 70 nm, and 2335 ∼ 63 nm. In (b), the diameter increases from hollow structures of 957 ∼ 12 nm in the first row, to hollow mushrooms of

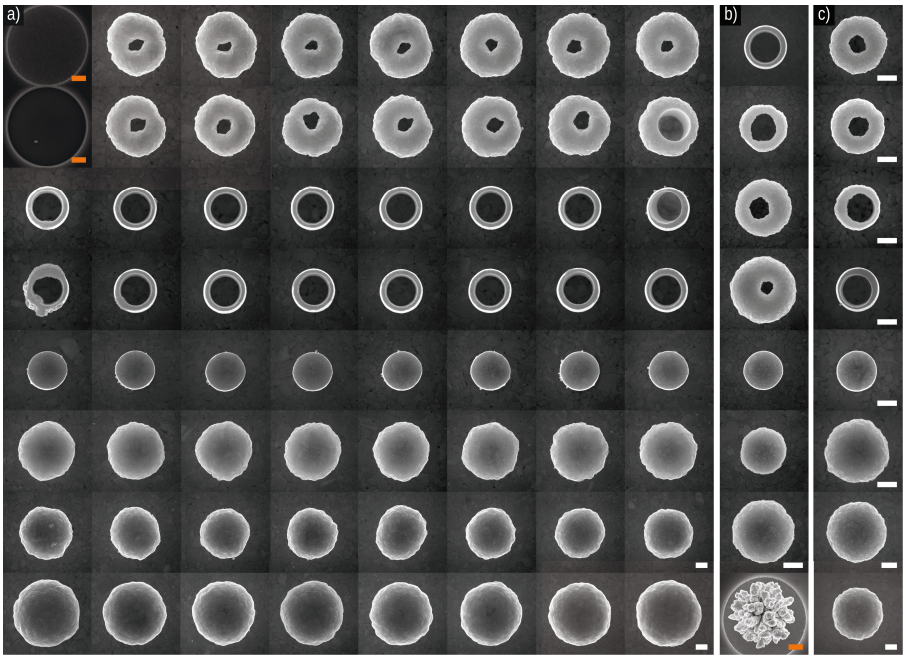

Figure 4.5: SEM top-view images of 3D electrodes on MEAs. (a) 64 electrodes of a single chip. While the top two rows are structured with hollow mushrooms, rows three and four exhibit hollow pillars, row five solid pillars, and rows six to eight are structured with solid mushrooms. (b) and (c) show exemplary 3D electrodes from each row of two different chips. With the method reported here, it is thus possible to prepare a variety of different structures with respect to both shape and size on a single chip. The structure diameters in (a) are 1381 ∼ 56 nm, 1314 ∼ 41 nm, 957 ∼ 10 nm, 970 ∼ 46 nm, 889 ∼ 13 nm, 1255 ∼ 27 nm, 1857 ∼ 70 nm, and 2335 ∼ 63 nm from top to bottom. The structure sizes in (b) are 957 ∼ 12 nm, 1019 ∼ 34 nm, 1257 ∼ 32 nm, 1463 ∼ 29 nm, 879 ∼ 9 nm, 994 ∼ 34 nm, 1372 ∼ 39 nm, and 8994 ∼ 246 nm from top to bottom, and the structure sizes in (c) are 1290 ∼ 38, 1181 ∼ 30 nm, 1029 ∼ 65 nm, 962 ∼ 15 nm, 896 ∼ 13 nm, 1435 ∼ 42 nm, 1646 ∼ 38 nm, and 1905 ∼ 35 nm from top to bottom. All size data is given as diameter of the cap, while the stalk width of all structures was kept constant at 800 nm. Orange scalebars represent 2 µm, white scalebars represent 400 nm and apply to all structures to their left and top unless indicated otherwise.

1019 ∼ 34 nm, 1257 ∼ 32 nm, and 1463 ∼ 29 nm in rows two, three, and four, respectively. Row five exhibits solid pillars (879 ∼ 9 nm), while rows six and seven are structured with solid mushrooms of increasing size, with diameters of 994 ∼ 34 nm and 1372 ∼ 39 nm, respectively. In row eight, cauliflower-like structures are prepared by application of a large overpotential of -1.50 V for 16.5 s, resulting in structures of 8994 ∼ 246 nm in diameter. In (c), the structure size decreases from row one to row four with cap diameters of 1290 ∼ 38 nm, 1181 ∼ 30 nm, 1029 ∼ 65 nm, and 962 ∼ 15 nm, respectively, while it increases for solid structures from row five to row eight, with diameters of

896 ∼ 13 nm in row five, 1435 ∼ 42 nm in row six, 1646 ∼ 38 nm in row seven, and 1905 ∼ 35 nm in row eight. Using the approach developed here thus facilitates the fabrication of various different structure types and sizes on a single chip.

In early experiments, the galvanization current was recorded with a sampling rate of 20 Hz and a 50 kHz low-pass filter. Due to the low current amplitude during the deposition of few nanoelectrodes, this results in significant noise, making the determination of $t_{boundary}$, the point at which the deposition proceeds past the upper boundary of the PMMA template, challenging. Therefore, the sampling rate was reduced to 4 Hz and a 5 Hz low-pass filter was employed in later experiments. Figure 4.6 shows characteristic traces obtained at a sampling rate of 20 Hz with a 50 kHz low-pass filter (a) and recorded at a sampling rate of 4 Hz with 5 Hz low-pass filter (b). Due to the

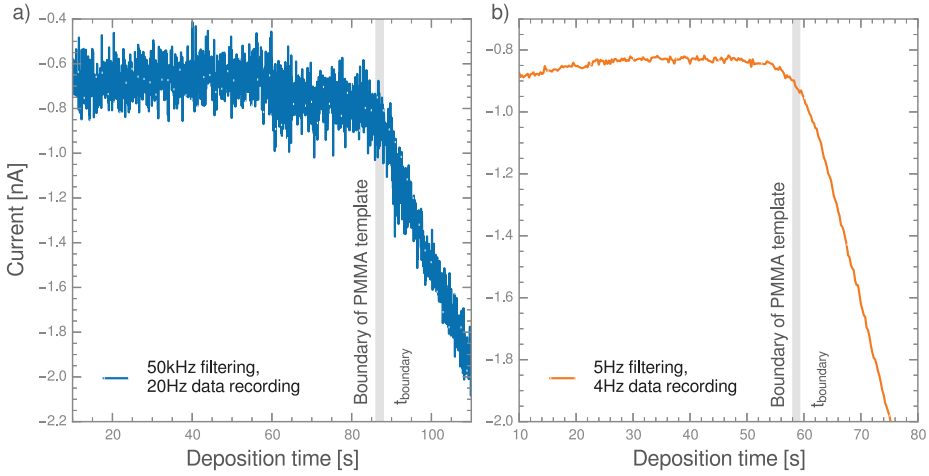

Figure 4.6: Characteristic traces obtained at a sampling rate of 20 Hz with a 50 kHz low-pass filter (a) and recorded at a sampling rate of 4 Hz with a 5 Hz low-pass filter (b). While $t_{boundary}$ can be observed in both cases, the lower noise characteristics obtained at the lower sampling rate enable an easier visualization, particularly for small values of $t > t_{boundary}$.

significantly reduced noise obtained in (b), $t_{boundary}$ can be determined more precisely, allowing for better control of the structure deposition. Therefore, this approach was chosen for all following experiments.

As has been stated before, once the deposition proceeds past the boundary of the PMMA template, transitioning into three-dimensional growth, the current starts to increase, signaling the

commencement of cap growth as seen in Fig. 4.6 after about 85 s (a) and 59 s (b). However, when comparing multiple different traces, it was found that the point at which the current starts to increase ($t_{boundary}$) varies between different sets of electrodes (Figure 4.7 a). This can be due to a number of reasons such as variations in the resist thickness, different roughness of the underlying gold, which results in changes in the kinetics of the galvanization particularly at the beginning of the deposition, or different wetting state that leads to a delay in the initiation of the galvanization. Due to these reasons, the total time of the galvanization (t_{total}) is an imprecise measure for the electrode size, as can be seen in Figure 4.7 (b). Therefore, the electrodeposition time past the

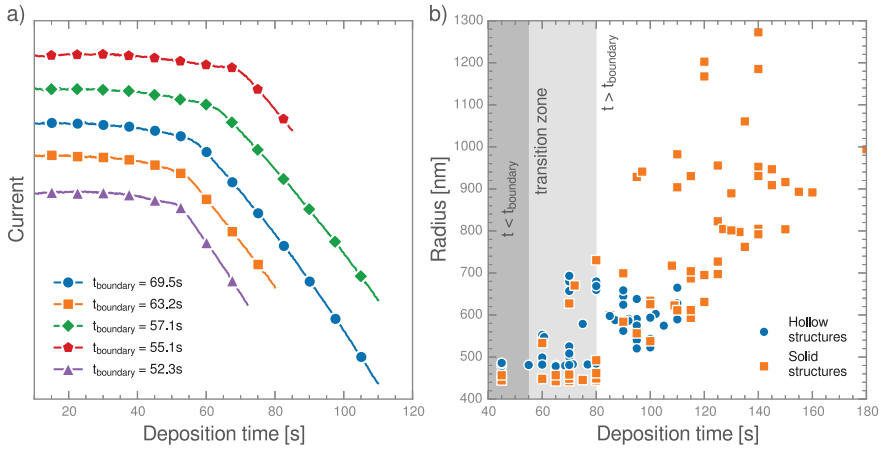

Figure 4.7: (a) Different current traces obtained from the galvanization of eight nanoelectrodes. Significant differences can be observed for $t_{boundary}$ from one deposition to the next. This can be due to differences in resist thickness, different wetting state and resulting delay in the initiation of the galvanization, or different initial kinetics due to variations in the roughness of the substrate. Traces shifted along y-axis for better visualization. (b) Radius of hollow and solid pillars and mushrooms in dependence on the deposition time. Due to the variation of $t_{boundary}$ as seen in (a), the total time of the deposition is an imprecise measure for the size of the resulting structures. While the general trend seems to be linear, no accurate correlation between the time of deposition and structure size can be developed.

boundary of the template (t_{total} $t_{boundary}$) was chosen as figure of merit. While the approximate $t_{boundary}$ in the raw data can be determined visually, enabling the experimentator to react to the change and adjust the deposition time according to the size requirements, $t_{boundary}$ was determined analytically for the establishment of the method by numerically differentiating the current traces and determining the minimum of the second order derivative. Due to the low current regime and high noise characteristics of the data, this necessitates a filtering step. The current traces were

thus smoothed with a third order Savitzky-Golay filter with a window size of 23, twice, which is equivalent to a time window of 5.75 s. Figure 4.8 shows the process for an exemplary current trace. The good correspondence between filtered and unfiltered data in (a) proves the adequacy of the filtering parameters. While the point of inflection in the first order derivative of the current traces is discernible both for the raw and filtered data, the high noise characteristics make the determination of the turning point in the second order derivative of the raw data impossible, proving the necessity of the filtering step. In this manner, $t_{boundary}$ was determined for all data traces, receiving

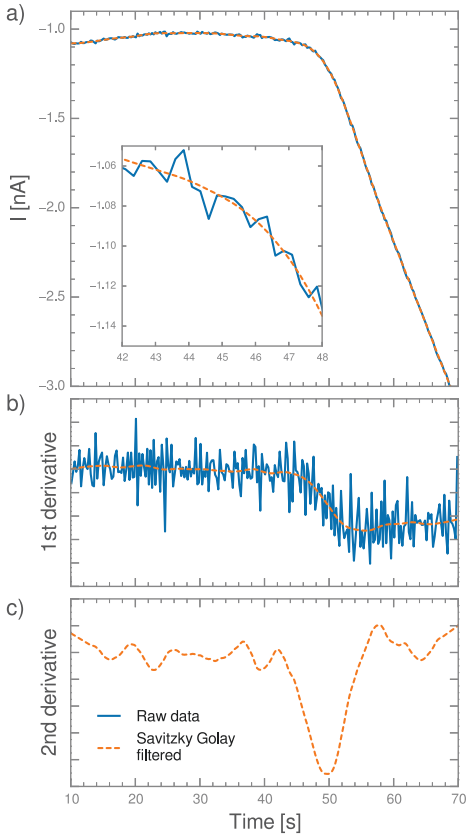

Figure 4.8: Numerical differentiation of the current data for the determination of $t_{boundary}$. In order to enable the determination of the minimum of the second order derivative, the data was smoothed with a third order Savitzky-Golay filter with a window size of 23 twice. This is equivalent to a time window of 5.75 s. The good correspondence between the raw and filtered data can be seen in (a). Subsequently, both raw and filtered data were numerically differentiated (b,c). While the point of inflection can still be estimated in the first order derivative of the raw data (b), the noise of second order derivative of the raw data is significantly too high to enable the localization of any discernible turning point. The second order derivative of the raw data was thus omitted from (c). The legend in (c) is valid for all depicted data.

$t_{boundary}$ of 75.7 ∼ 16.2 s, thus confirming the strong variations in $t_{boundary}$ and the necessity to correct for them. Of the traces recorded at a sampling rate of 4 Hz and 5 Hz low-pass filter, 78% could be analyzed with the developed Python script (n = 150 current traces). In the remaining cases, t_{total} was either too close to $t_{boundary}$ to determine the minimum of the second order derivate, or a drift

in the recorded current made an analysis of the resulting trace impossible.

Figure 4.9 shows the dependence of the structure size on the deposition time, corrected for variations in $t_{boundary}$. In contrast to the data reported for SEM images, the size of the structures is given with respect to their radius for the investigation of the size dependency to enable the determination of the 1D deposition rate and thus facilitate the direct comparison with the deposition rate determined in Chapter 3 and the height development reported at a later stage. Plotting the time past $t_{boundary}$ (t_{total} $t_{boundary}$) versus structure size yields a clear linear dependence in all cases. In addition to the outer radius of solid and hollow pillars, the opening size of hollow pillars is reported as well. Two different trends could be observed for all data series. Evaluation of the

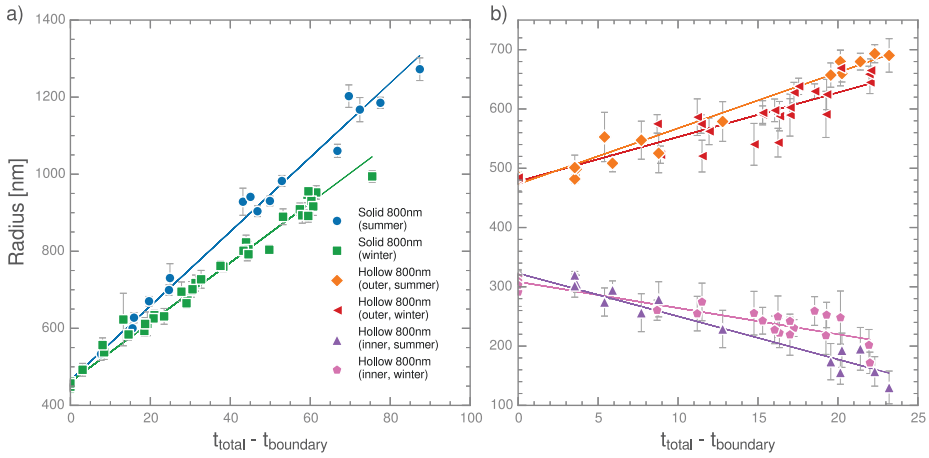

Figure 4.9: Electrodeposition time past boundary (t_{total} $t_{boundary}$) versus structure radius for both solid (a) and hollow (b) structures, as well as the inner radius of hollow structures (b). After correcting the data for variations in $t_{boundary}$, a clear linear relationship can be found in all cases, enabling good control over the size of the electrodes. The two different trends observed for all measurements can be attributed to temperature differences between sets of experiments conducted in summer and in winter, suggesting that the introduction of temperature control is an important aspect for future studies. Nevertheless, the differences are small enough to allow for the prediction of the resulting structure size from the current traces. Error bars represent the corrected sample standard deviation.

differences between the samples constituting the respective results yielded no discernible distinction with respect to either sample batch or cleanroom fabrication date. The only clear difference is that of season, with samples associated with the higher slope being deposited in summer, when the temperature in the lab was higher, than for the samples associated with the lower slope deposited in winter, when the temperature was lower. The introduction of temperature control thus

seems to be an important aspect for future studies. Nevertheless, in the range of structure sizes reasonable for the interaction with neuronal cells, the difference between summer and winter is small enough to enable good control over the resulting structure size. Since hollow templates will result in the formation of solid mushrooms for large values of $t > t_{boundary}$ due to the overgrowth of the opening, values of around $t_{boundary}$ + 20 s are the extend of reasonable deposition times, at which point the radius between the data obtained in summer and winter differs by 30 nm. For solid mushrooms, the range of possible sizes is limited by the innate cellular limit for engulfment of around 2 µm cap diameter for rat hippocampal neurons,[56] rather than fabrication restrictions. Therefore, the possible size deviation is larger in this case. A deposition time of 60 s past $t_{boundary}$ yields solid mushrooms of around 1 µm in radius and thus 2 µm in diameter for depositions conducted in summer, while the radius of structures in winter is approximately 120 nm smaller. This difference in deposition speed also becomes apparent when determining the respective variations in $t_{boundary}$ for the two different data sets, with $t_{boundary}$(summer) of 56.9 ∼ 6.6 s and $t_{boundary}$(winter) of 85.6 ∼ 9.8 s, showing that the deposition proceeds slower at the lower temperatures observed in winter.

From the linear r(t) relation shown in Figure 4.9, the deposition rate (slope) and the radius of the template (y-intersect) are received as

$$r(t)_{solid,\ summer} = (9.8 \sim 0.2\ nm/s) \pm (t_{total} \quad t_{boundary}) + (456 \sim 6\ nm) \tag{4.1}$$

with an adjusted R-square of 0.9927 for solid structures,

$$r(t)_{hollow\ outer,\ summer} = (9.1 \sim 0.5\ nm/s) \pm (t_{total} \quad t_{boundary}) + (476 \sim 3\ nm) \tag{4.2}$$

with an adjusted R-square of 0.9584 for the outer radius of hollow structures, and

$$r(t)_{hollow\ inner,\ summer} = (\quad 7.3 \sim 0.4\ nm/s) \pm (t_{total} \quad t_{boundary}) + (323 \sim 5\ nm) \tag{4.3}$$

with an adjusted R-square of 0.9469 for the inner radius of hollow structures, all with respect to the structures deposited in summer. For the structures in winter, r(t) yields

$$r(t)_{solid,\ winter} = (7.7 \sim 0.1\ nm/s) \pm (t_{total} \quad t_{boundary}) + (461 \sim 4\ nm) \tag{4.4}$$

with an adjusted R-square of 0.9880 for solid structures,

$$r(t)_{\text{hollow outer, winter}} = (7.5 \sim 0.5\,\text{nm/s}) \pm (t_{\text{total}} \quad t_{\text{boundary}}) + (478 \sim 7\,\text{nm}) \tag{4.5}$$

with an adjusted R-square of 0.8722 for the outer radius of hollow structures, and

$$r(t)_{\text{hollow inner, winter}} = (\quad 4.4 \sim 0.4\,\text{nm/s}) \pm (t_{\text{total}} \quad t_{\text{boundary}}) + (308 \sim 6\,\text{nm}) \tag{4.6}$$

with an adjusted R-square of 0.8428 for the inner radius of hollow structures. As can be seen, the deposition velocity for the radius of solid and hollow structures is very similar within the two sets of experiments ($\text{solid}_{\text{summer}}$ and $\text{hollow}_{\text{summer}}$, or $\text{solid}_{\text{winter}}$ and $\text{hollow}_{\text{winter}}$) and generally in good agreement with the value obtained in Chapter 3 of 8.5 nm/s for depositions at -1.10 V (Figure 3.10). In contrast, the growth rate into the interior of the hollows is notably smaller than the growth rate of the outer radius. This could be due to the interference of the outgrowth of the PMMA plug. A slight outgrowth, which is then stopped due to the stabilization of the plug because of overgrowing gold, will result in structures that are hollow in shape but exhibit opening sizes that are slightly larger than what would be expected theoretically. However, since larger opening sizes are advantageous for the intended application, this effect does not signify a negative influence.

To prove that this concept is also applicable for real-time control of the deposition, t_{boundary} was determined visually from the respective current traces. The data received in this manner is very comparable to the results achieved by numerical differentiation (Figure 4.10), with an average difference between the visually and numerically determined t_{boundary} of $1.0 \sim 0.9$ s and a maximum difference of 4.0 s, which is equal to an average and a maximum difference in radius of 10 nm and

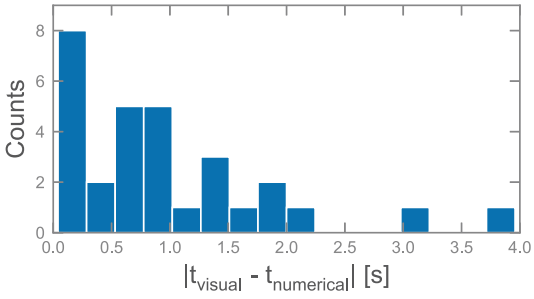

Figure 4.10: Absolute value of the difference between t_{boundary}(visual) and t_{boundary}(numerical), showing that the shift from the mathematically determined value is generally very small, enabling real-time control over the structure size of 3D nanoelectrodes by adjusting the deposition parameters according to the development of the current during the deposition.

39 nm, respectively, for structures deposited in summer, and consequently smaller for structures deposited in winter.

In addition to the investigation into the radius of the structures, the height h of solid structures deposited in summer was determined via laser scanning profilometry to enable a better description of the cap growth of solid mushrooms. Figure 4.11 shows the results for the height versus t_{total} $t_{boundary}$. From the linear interpolation, h(t) is received as

$$h(t)_{solid\ summer} = (9.9 \sim 0.5\ nm/s) \pm (t_{total} \quad t_{boundary}) + (1180 \sim 24\ nm) \tag{4.7}$$

with the growth rate of 9.9 nm/s being almost equal to the value of 9.8 nm/s as determined from the radius of the structures, showing that the deposition rate is equal in all three dimensions as expected. The y-intersect of 1180 nm represents the PMMA thickness in this case and is in good accordance with results obtained from SEM images.

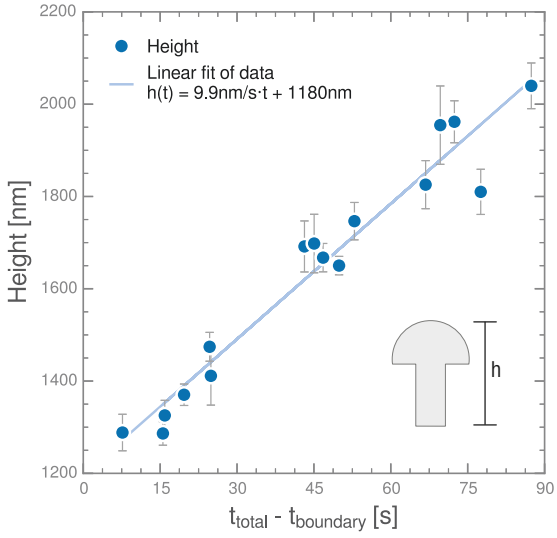

Figure 4.11: Total height h of solid nanoelectrodes in dependence on the time of galvanization after the bend (t_{total} $t_{boundary}$). As observed for the radius of the structures, h(t) exhibits a linear relationship in dependence on the time of deposition past the boundary of the template, yielding a growth rate that is very comparable to the growth rate determined for the radius of the structures. Error bars represent the corrected sample standard deviation.

As a proof-of-concept study, the hollow area of one type (A) MEA was deposited one electrode at a time to determine whether control over single-electrode depositions is possible. Figure 4.12 shows the results obtained for the structures thus produced. From the linear r(t) relation, the

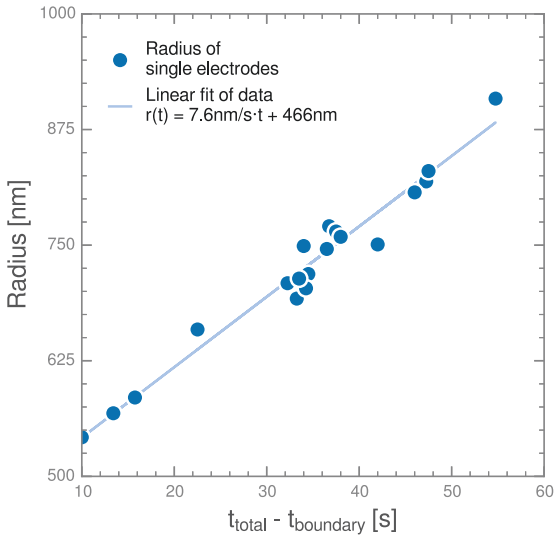

Figure 4.12: Dependence of the radius of the structure on t_{total} $t_{boundary}$ for single-electrode depositions into hollow templates. A clear, linear correlation can be observed that is in good agreement with the data received for sets of eight electrodes. While more data is needed, the approach developed here seems to facilitate well-controlled depositions of single electrodes.

growth rate (slope) and the radius of the template (y-intersect) are received as

$$r(t) = (7.6 \sim 0.4\,\mathrm{nm/s}) \pm (t_{total} \quad t_{boundary}) + (466 \sim 13\,\mathrm{nm}) \tag{4.8}$$

with an adjusted R-square of 0.9628. This is in good accordance with the results obtained from sets of eight electrodes, proving that the control of single-electrode depositions is possible (n = 19 electrodes). One major problem occurring during this experiment was significant drift in the current in approximately 50% of cases. This drift seems to not be due to an actual galvanization current since, for the traces where $t_{boundary}$ could be determined from the second order derivative, the size data for t_{total} $t_{boundary}$ is in good agreement with the general trend. Currently, the reason for this effect cannot be determined. In general, when significant drift occurred, the chip holder was thoroughly cleaned prior to the next deposition to ensure that all potential salt bridges are removed.

In addition to MEAs exhibiting both hollow and solid structures of 800 nm stalk width (MEA type A), chips containing solid structures of 300 nm, 600 nm, and 800 nm stalk width (MEA type B) as well as chips containing bigger hollow structures (MEA type C) were fabricated. Figure 4.13 shows SEM images of the 64 electrodes on a MEA exhibiting solid structures (MEA type B). The upper two

rows exhibit structures of 300 nm template diameter, resulting in mushrooms of 1591 ∼ 45 nm in cap diameter and pillars of 378 ∼ 16 nm in stalk width. Rows three and four exhibit mushrooms and

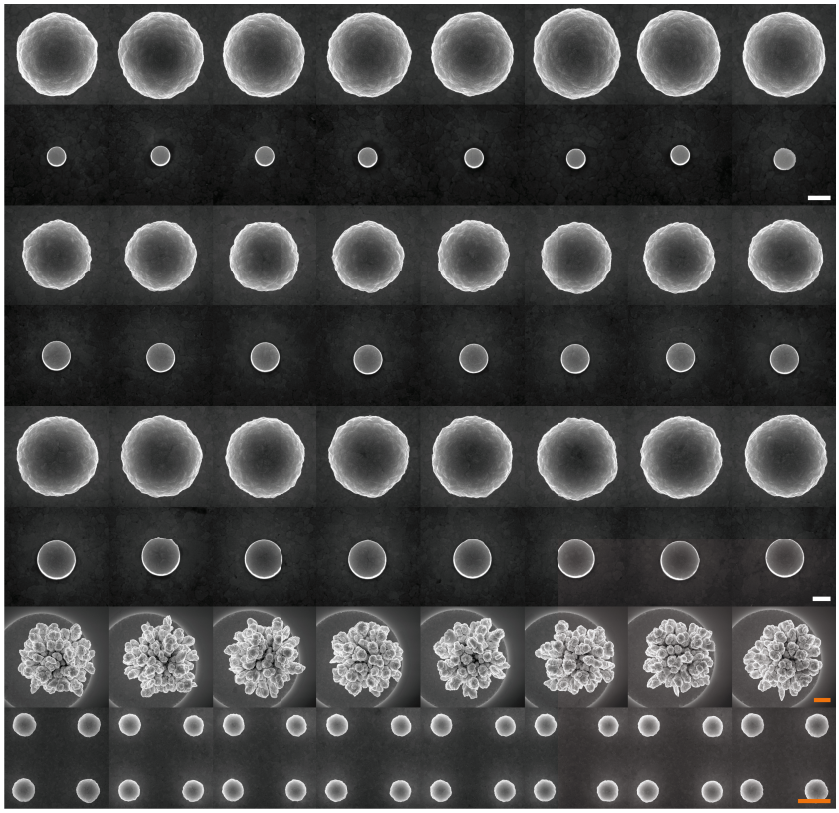

Figure 4.13: SEM top-view images of solid 3D electrodes on MEAs (MEA type B). Rows one and two exhibit structures of 300 nm stalk width, while the stalk of the structures in rows three and four is 600 nm in diameter, and 800 nm in diameter in rows five to eight. Solid pillars were deposited in rows two, four and six, solid mushrooms in rows one, three, and five, as well as row eight, where each electrode exhibits four mushrooms. In row seven, cauliflower-like electrodes were produced. The resulting structure sizes are (top to bottom) 1591 ∼ 45 nm, 378 ∼ 16 nm, 1687 ∼ 34 nm, 688 ∼ 8 nm, 1911 ∼ 20 nm, 914 ∼ 12 nm, 9036 ∼ 312 nm, and 1381 ∼ 59 nm with respect to the diameter of cap of the structures. Orange scalebars represent 2 µm, white scalebars represent 400 nm and apply to all structures to their left and top unless indicated otherwise.

pillars of 600 nm stalk width, with a mushroom cap of 1687 ∼ 34 nm in row four, while the pillars in row five are 688 ∼ 8 nm in size. Structures of 800 nm were defined in rows five to eight, with mushrooms of 1911 ∼ 20 nm cap diameter and pillars of 914 ∼ 12 nm in rows five and six, cauliflower-like structures of 9036 ∼ 312 nm in row seven, and a 2x2 arrangement of mushrooms of 1381 ∼ 59 nm

each in row eight. The low number of chips prepared in this manner precludes a detailed analysis of the size-dependence for these structures. The data received for the 800 nm structures, however, is in good accordance with the results presented above. More data is needed for 300 nm and 600 nm structures to enable a reliable analysis.

Figure 4.14 shows a MEA exhibiting big hollow structures (MEA type C), with rows one and two being structured with 1 µm, rows three and four with 2 µm, rows five and six with 3 µm, and rows seven and eight with 5 µm hollow pillars and mushrooms. While both 1 µm and 5 µm templates

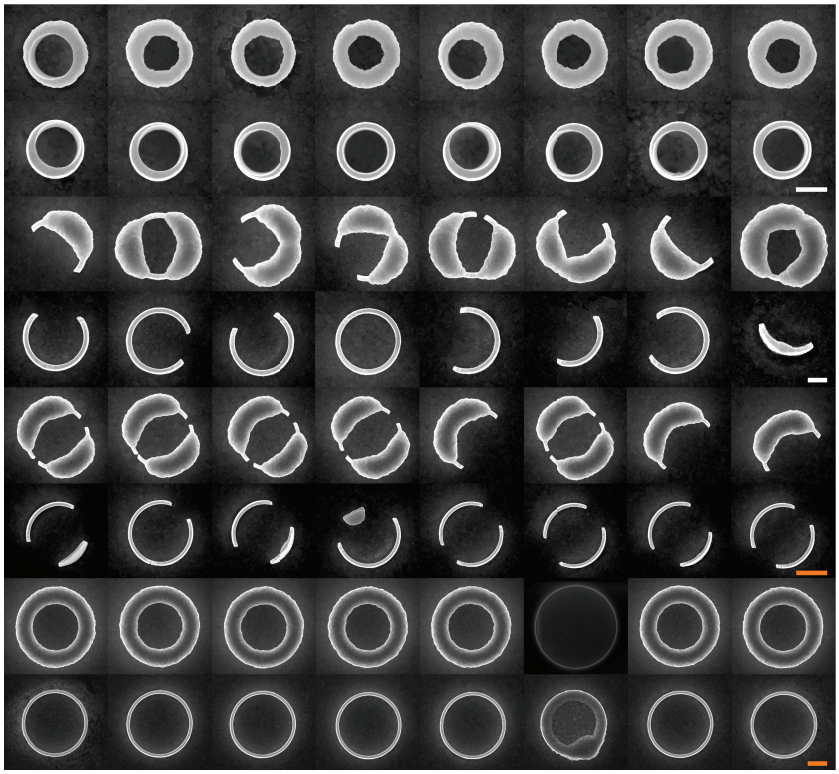

Figure 4.14: SEM top-view images of big hollow 3D electrodes on MEAs. Rows one and two exhibit structures of 1 µm stalk width, while the stalk of the structures in rows three and four is 2 µm in diameter, 3 µm in rows five and six, and 5 µm in rows seven and eight. Hollow pillars were produced in rows two, four, six, and eight, while hollow mushrooms were deposited in rows one, three, five, and seven. While both 1 µm and 5 µm structures could be produced with high fidelity, structures of 2 µm and 3 µm seem to not be exposed down to the underlying gold, resulting in only partial structures. Orange scalebars represent 1.5 µm, white scalebars represent 600 nm and apply to all structures to their left and top unless indicated otherwise.

could be transferred to chips employing the parameters obtained in Chapter 3, 2 µm and 3 µm structures were not fully exposed, resulting in very low structure yield. Overall, hollow 1 µm structures were obtained in 63% of the cases, while 23% of the structures of this size were solid, 11% exhibit the artifact resulting from the outgrowth of the PMMA plug, and 3% of electrodes were missing structures altogether (n = 4 chips). For 5 µm structures, 89% were hollow, 5% solid, 3% exhibited the artifact, and 3% of electrodes were empty. In contrast, 75% of the 2 µm and 97% of the 3 µm structures were not fully exposed, thus forming incomplete circles. Attempts at removing the residual PMMA masking the underlying gold through an extended development or by application of oxygen plasma were not successful. For future experiments, the adaptation of the electron-beam lithography parameters employed for structures of 2 and 3 µm in diameter is thus a prerequisite for the successful fabrication of these designs.

In conclusion, well-controlled depositions could be achieved on MEAs exhibiting hollow and solid templates of 800 nm in diameter (MEA type A), with a clear, linear relationship between structure size and deposition time after correcting for variations in $t_{boundary}$. While the data basis is insufficient to report a reliable correlation for the development of the size for solid structures of 300 and 600 nm stalk width, the different structures could be produced with high fidelity. In contrast, the transfer of bigger hollow mushrooms to MEAs necessitates an adjustment of the electron-beam lithography parameters in future studies to enable not only the fabrication of 1 µm and 5 µm structures as presented here, but also the production of 2 µm and 3 µm 3D designs. Furthermore, the introduction of temperature control could improve the predictability of the 3D electrode size by preventing influences of the ambient temperature.

4.2.2 Electrophysiological investigation of HL-1 cells on 3D electrodes

To probe for the differences in recording capability resulting from the introduction of the various 3D structures, action potential (AP) recordings were performed using cardiomyocyte-like HL-1 cells as model system. HL-1 cells have multiple advantages over primary cardiac cells such as their availability independent from animal testing facilities and regulations, scalability of cell numbers due to the capability for cell division, easy maintenance, and stability with respect to the characteristics of the cells. For these reasons, they have been employed for numerous studies of the cell-device interface and coupling.[21,45,98,104] Prior to cell culture, the employed MEAs were thoroughly cleaned

and glass rings were glued onto the chips as medium reservoir. Two differently sized rings were employed to maintain a high ratio of medium versus cell count by seeding the cells into the smaller ring, waiting for cell attachment, and then adding sufficient medium to fill the larger ring. The chips were initially coated with 5 µg/ml fibronectin in a 0.02% solution of gelatin in water (FibGel) prior to cell seeding, as has been done in previous reports.[45,104] However, during these early experiments, poor cell adhesion was observed. While HL-1 cells in culture dishes usually show very good cell adhesion that is unperturbed by media changes and the resulting shear-stress, the cells plated on MEAs could easily be removed from the chips by gentle rinsing. Subsequently, the chips were coated with 2.5 µg/cm^2 fibronectin rather than FibGel to avoid the dissolution and detachment of gelatin residues as possible reason for poor cell adhesion. Nevertheless, cell adhesion remained a problem. A possible reason for this issue is the presence of PMMA residues (Figure 4.15), which could be observed on many of the employed MEAs despite repeated cleaning, resulting in water contact angles of around 70°. Since fibronectin adsorbs differently on hydrophilic and hydrophobic surfaces, this poses a problem. While higher fibronectin adsorption was shown to occur on hydrophobic surfaces, the biological activity was significantly reduced as compared to fibronectin on hydrophilic surfaces, which resulted in poor cell spreading on fibronectin-treated hydrophobic culture dishes in a study employing baby hamster kidney cells.[143] At higher concentrations of fibronectin employed for the coating procedure, the difference in cell spreading decreased, potentially meaning that fibronectin acquires a different conformation on hydrophobic surfaces as compared to hydrophilic ones, which can be prevented by close packing.[143] Nevertheless, this study suggests that the surface characteristics can have a notable impact on fibronectin adsorption and thus cell adhesion. Therefore, the MEAs were re-cleaned in AR 600-71, a dioxolan-based solvent that shows high capabilities at removing PMMA, followed by rinsing with acetone, isopropanol, and ultrapure water. In this manner, the contact angle could be reduced to 40-60° in most cases. For

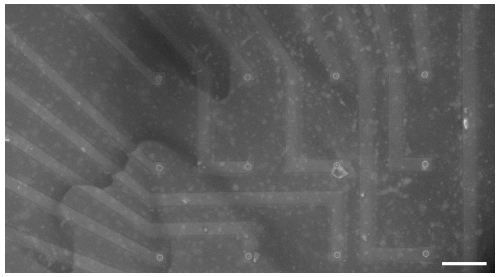

Figure 4.15: SEM image of pronounced PMMA residues on a MEA. While most chips exhibited significantly less residual PMMA, the full removal after electrodeposition proved to be challenging. Scalebar represents 100 µm.

chips that exhibited significant PMMA residues, oxygen plasma cleaning was performed. For future studies, the cleaning cascade after electrodeposition should be extended, ensuring removal of all PMMA residues prior to SEM analysis since removal of dried and electron-beam treated residues proved to be challenging. Another approach is the specific functionalization of the surface via silanization. Within this body of work, (3-aminopropyl)triethoxysilane (APTES) was employed to increase the hydrophilicity of MEAs in cases where no adequate cell adhesion could be achieved, followed by incubation with fibronectin. This approach improved the cell adhesion on MEAs that had previously shown very weak HL-1 attachment. However, more data is needed to draw reliable conclusions. In either case, the surface characteristics of the employed MEAs and the removal of PMMA were found to be a fundamental parameter for good cell adhesion. The establishment of a reproducible process is therefore essential for future studies.

All electrophysiological studies conducted within this body of work were performed on a 64 channel amplifier system developed in-house. Voltage recordings were performed on all 64 channels in parallel with a sampling rate of 10 kHz per channel and a total gain of 1010.[142] The effective bandwidth was limited with a high pass filter (AC coupling) and a low pass filter (high frequency cutoff) from 1 Hz to 3 kHz for all measurements. All data is reported as raw, unfiltered recordings. Figure 4.16 shows characteristic extracellularly recorded HL-1 signals. Regular mechanical

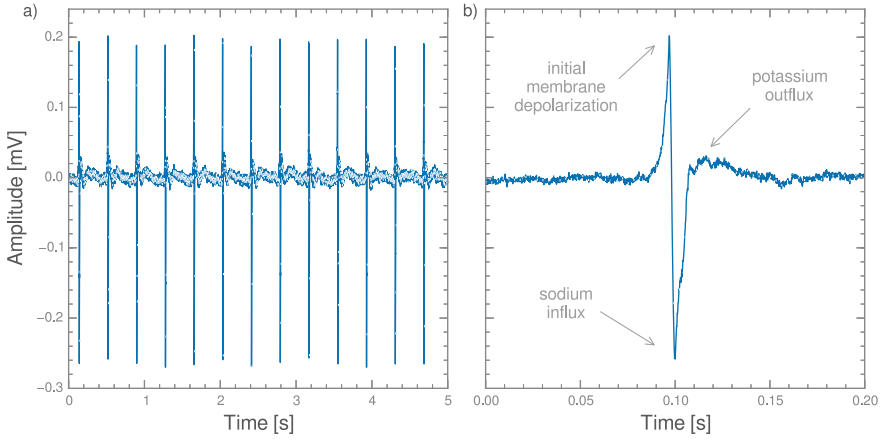

Figure 4.16: Characteristic extracellular signals recorded from HL-1 cells. During the measurement reported here, the cells exhibited rhythmic activity with a frequency of 2.6 Hz. (b) shows a negative triphasic AP signal enlarged from (a). After the initial membrane depolarization, the influx of sodium results in a fast negative peak. Potassium outflux yields a small positive overshoot during repolarization.

contractions could be observed during this measurement, which could be shown to occur with a frequency of 2.6 Hz as determined from the spiking pattern of the action potential recording. During extracellular recordings, negative spikes reflect inward currents while positive spikes are the result of outward currents.[90] While the initial positive deflection in Figure 4.16 is thought to be due to the membrane depolarization to threshold,[144] the negative spike results from the sodium influx during depolarization (Figure 2.11b, phase 0) and the final positive signal from the potassium outflux during repolarization (Figure 2.11b, phase 3).[43,145] Overall, various different spike shapes can be detected during MEA-based AP recordings since many factors influence the signal shape, such as *e.g.* the sealing resistance,[43] as well the characteristics of the device and amplification system.[144] Furthermore, the signal detected by an extracellular electrode is dependent on the rise and decay time of the action potential[89] as shown in Equation 2.28. Therefore, different shapes and amplitudes of the recorded APs can be observed for HL-1 cultures under the influence of multiple pacemakers as seen in Figure 4.17. This behavior results from the variations in cell adhesion

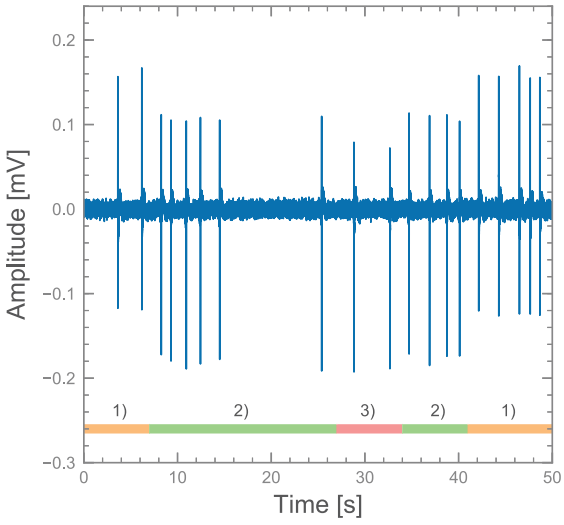

Figure 4.17: Arrhythmic HL-1 cells, with action potentials induced by different propagation waves, yielding three distinct spike clusters. Correlation of the signals on all 64 electrodes shows that the action potentials in 1) propagate from left to right, APs in 2) from bottom to top, and in 3) from right to left. Since the recorded signal depends on the rise and decay time of the signal,[89] action potentials induced by different pacemakers can exhibit different shapes and amplitudes.

and thus culture characteristics observed within this body of work. For a very active culture, most often one pacemaker dictates the propagation of action potentials since the refractory period after a depolarization and repolarization cycle, a time when no action potential can be triggered due to the inactivation of ion channels, prevents a second pacemaker operating at a different frequency from interfering. In cases where the cellular activity is low, though, and the time between action

potentials is thus longer, additional pacemakers can hijack the culture. In Figure 4.17, this results in the observation of three distinct clusters of different spike shape. When investigating all 64 electrodes, it can be found that action potentials in group 1) propagate from the left to the right side of the chip, while APs in group 2) propagate from bottom to top, and APs in group 3) from right to left.

For the analysis of the signals recorded with the MEAs developed as part of this body of work, the amplitudes recorded over a time of 60 s were averaged both for regularly as well as irregularly beating cultures. All signals below the threshold of 2.5 times the noise level N (N = 20 μV_{p2p}) were excluded from the analysis. Due to the correlated nature of the HL-1 signals, a threshold of 2.5xN is sufficient to distinguish between cellular signals and noise, since even arrhythmic HL-1 cultures can be grouped into correlated clusters and thus recognized as cellular signal. Figure 4.18 shows the results obtained for the various different 3D designs investigated. The box plots represent the recorded amplitudes from n electrodes, while the line plots show the percentage of electrodes that yielded signals above 50 µV (2.5xN) from the total number of electrodes exhibiting the respective structure employed for electrophysiological studies. A distinct difference in the recording yield can be observed with respect to chips employed during early experiments that were not subject to the improved cleaning cascade versus later experiments, with chips cleaned in either AR 600-71, oxygen plasma, or both. Experiments on hollow pillars and mushrooms were predominantly performed with early chips and thus insufficient PMMA removal. Since these chips also contained pillars and mushrooms of 800 nm in diameter, the recording yield of these structures is also very low when considering all employed chips. After omission of all recordings from earlier experiments, the recording yield of these structures increases drastically and becomes comparable to that of the 300 nm and 600 nm structures present on chips of the same, later batches. Since no structures of 800 nm in stalk width and cap diameter >2000 nm were present on later chips, no corrected yield can be reported. As with 800 nm structures, removing the results from earlier experiments greatly increases the yield of cauliflower-like structures. Furthermore, the yield of these structures is markedly higher than for any other structure on MEAs with 12 µm aperture. The recording yield of structures prepared on 24 µm MEAs is generally higher than that on 12 µm chips, which can be due to the larger area and thus higher probability of functional coupling. The recording yield for planar electrodes is of limited informative value since action potentials were recorded both on electrodes

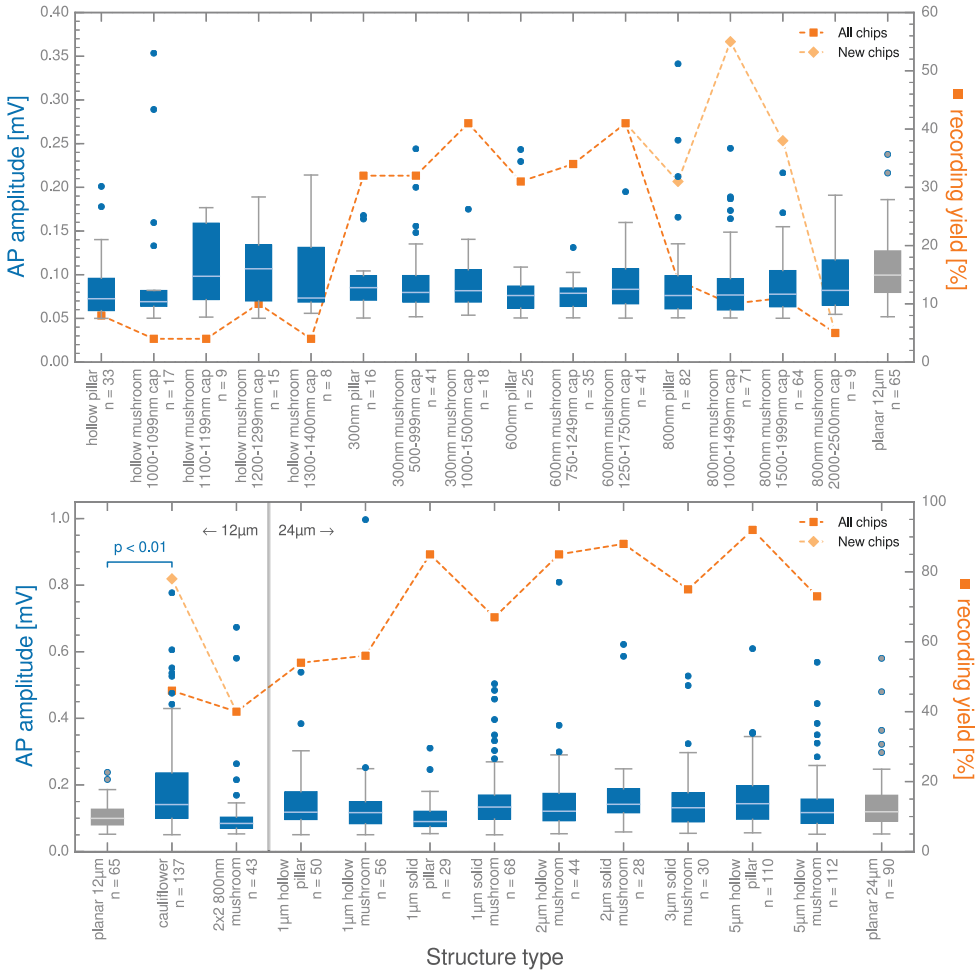

Figure 4.18: Results from the action potential (AP) recordings performed within this body of work. All recordings with amplitude lower than 2.5 times the noise level N (N = 20 μV_{p2p}) were excluded from the analysis. The box plot divides each data set into four equal groups by count of data points, with the box representing the data between the first (Q1) and third (Q3) quartile, or interquartile range (IQR). The median is marked with a light blue line. Data points above Q3+1.5 x IQR or below Q1-1.5 x IQR are considered as outliers and marked as solid blue circle. The whiskers mark the last data point that meets this requirement. In cases where no outliers are present, the whiskers mark the maximum and minimum of the data set. While many outliers with good signal amplitude can be observed on various structures, no significant increase in signal amplitude on electrodes exhibiting 3D structures as compared to their planar equivalent (gray boxes) can be observed, with the exception of cauliflower-like structures ($p<0.01$). For many structures, the number of recorded signals n is very low, despite a large number of performed recordings since the recording yield - the number of signals recorded above 50 µV (2.5xN) versus the number of available electrodes - is very low. All structures in the upper graph were prepared on MEAs exhibiting 12 µm apertures, as were the 2x2 and cauliflower-like structures. All larger structures were prepared on 24 µm MEAs. The recording yield data is connected with dotted lines for better visualization.

actively left without a structure as well as electrodes where the fabrication of 3D structures was not possible. Since APs could be measured on many of these, the problem seems to be a matter of electron-beam fabrication rather than inactive electrodes, however, residual passivation layers cannot be excluded, producing an unknown number of non-functional electrodes that could falsify the yield. Therefore, the respective data is not reported.

As can be seen from the amplitude data (Figure 4.18), the presence of 3D structures has no marked effect on the recording capabilities of the presented MEAs. The only structures yielding a significant improvement as compared to their planar equivalent are cauliflower-like structures with $p<0.01$ as determined via a two-sided Mann Whitney U test. However, while these structures seem to form a good contact to HL-1 cells, they are considerably too large to facilitate neuronal engulfment. As reported by Ojovan *et al.*,[56] the innate limit of mushroom-cap diameters still allowing for cellular engulfment is between 2 and 2.5 µm for rat hippocampal neurons, while the cauliflower-like structures presented here have diameters of around 8 µm. Therefore, no recording advantage can be expected with these structures for the investigation of neuronal networks. When considering all data reported in Figure 4.18, some high-amplitude signals could be recorded that came close to the expected maximum of extracellular signal recording on planar MEAs of around 1 mV.[5] However, no reproducible correlation between 3D design and incidental high-amplitude recordings could be found, suggesting that these outliers fall in the category of 'serendipitous surface adhesion',[62] rather than showing an actual influence of the recording capabilities of the 3D structure. Furthermore, the observed amplitudes are far below the results achieved with 3D structures in the literature, where *e.g.* Schmoel *et al.*[54] reported action potentials of up to 5 mV_{p2p} for embryonic rat hippocampal neurons on mushroom-shaped 3D electrodes. Employing the same system, Fendyur *et al.*[109] reported biphasic action potentials in the range of 500 μV_{p2p} from rat embryonic cardiac myocytes. While this is closer to the range of potentials measured here, the 3D electrodes developed as part of this body of work did not consistently yield recordings of this amplitude, despite their significantly higher surface area as compared to the isolated 3D structures employed by Fendyur *et al.* The same is valid for the report by Xie *et al.*,[98] who employed five 1.5 µm high Pt nanopillars of 150 nm in diameter to record action potentials from HL-1 cells with amplitudes of 100-200 μV_{p2p}, or the publication by Lin *et al.*,[50] who recorded APs of 300 μV_{p2p} employing an array of nine hollow iridium oxide pillars. Again, the available surface area of the electrodes

employed in this body of work is significantly larger than that of the 3D electrodes employed by both Xie and Lin, while the results obtained with the presented MEAs are comparable to or lower than what these groups reported. However, it has to be noted that in many publications, little information is given as to whether the reported amplitudes are the average or maximum values, which makes a comparison of the obtained data challenging. In the report by Shmoel *et al.*,[54] only 34.5% of the recorded amplitudes were in the range above 300 μV_{p2p}, showing the great variability of recorded signals. Only reporting the signals of maximum amplitude obtained in this study would result in the conclusion that 1 µm mushroom-shaped structures cause a clear improvement of the recording capabilities, yielding a maximum amplitude of 997 μV_{p2p} as compared to 580 μV_{p2p} on 24 µm planar electrodes. The second largest amplitude of 810 μV_{p2p} was recorded on 2 µm hollow mushrooms, followed by 780 μV_{p2p} on cauliflower-like structures, and 670 μV_{p2p} on a 2x2 arrangement of solid mushrooms with 800 nm stalk width. However, for an in-depth comparison of the influence of the different structures, a mere investigation of the signals of highest amplitude is not sufficient. Rather, the goal is to determine geometrical aspects that yield high-amplitude signals with good reproducibility. This raises question of why the observed signal amplitudes are generally low. Various influential factors can be identified with respect to this question. First and foremost, the poor cellular adhesion on the chips does not only influence the recording yield but will also have an effect on the cell-electrode distance, which directly influences the sealing resistance and thus recording efficiency. An additional problem inherent for the devices presented here is the ratio of structure size and passivation height. In contrast to the schematic representation in Figure 2.19, the thickness of the passivation is only marginally smaller than the structure height in most cases (Figure 4.19 a). Furthermore, on many of the employed MEAs, a misalignment of the aperture in the passivation with respect to the electron-beam defined 3D structure yields an off-center position of the 3D design, which results in a much smaller lateral distance between 3D electrode

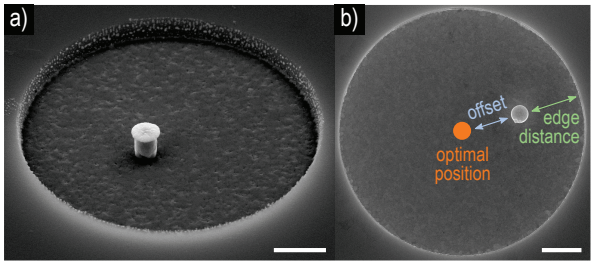

Figure 4.19: SEM images of problems occurring during the MEA fabrication. (a) Inherently, the 3D structure is in a recessed position with respect to the passivation surface. (b) Misalignment between 3D structure and aperture results in structures with small lateral distance to the edge of the passivation. Scalebars represent 2 µm.

and surrounding passivation (Figure 4.19 b). This is a significant problem, especially considering the low cellular capability with respect to the protrusion into openings as observed in Chapter 3 (see Figure 3.26). These issues result in multiple disadvantages for the cell-chip coupling. Due to the recessed position of the 3D structure, the cell must first protrude into the opening of the passivation before engulfment can occur (Figure 4.20 a). Furthermore, the misalignment between structure and aperture can result in the cell spanning over the distance between the top of the 3D structure and surrounding passivation (Figure 4.20 b). This results in a significantly smaller contact area between cell and electrode as compared to the case of a planar electrode (Figure 4.20 c) and thus in a reduced sealing resistance and coupling efficiency, assuming low sealing between

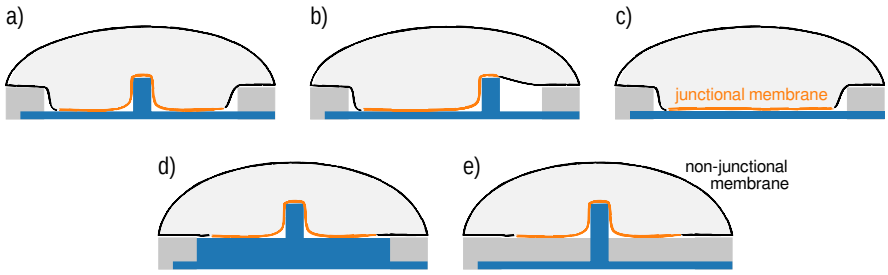

Figure 4.20: Problems and possible solutions for 3D electrodes on MEAs: In contrast to earlier schematics, the 3D structure is only slightly higher than the 800 nm of surrounding passivation. The cell must thus first protrude into the opening of the passivation before engulfment can occur (a). If the alignment of aperture and 3D structure is not ideal, the gap between 3D structure and the edge of the passivation becomes smaller, which influences the engulfment. If the cell spans the distance between 3D structure and surrounding passivation as in (b), the contact area and thus coupling are reduced as compared to a planar configuration (c), assuming low sealing between the cell and surrounding passivation. Possible solutions to this problem are the preparation of free-standing 3D structures, either by filling the aperture with metal prior to the preparation of 3D structures (d), or by electron-beam processing on fully passivated MEAs and subsequent removal of the passivation underneath the template (e).

the cell and surrounding passivation. In the pronounced case of poor engulfment as depicted in Figure 4.20 (b), the 3D structure essentially impairs the recording capabilities of the electrode as compared to that of planar electrodes. Apart from improvements to the alignment process during MEA fabrication, possible solutions for this problem are either filling up the opening in the passivation with electrode material prior to the electron-beam processing (Figure 4.20 d), or the omission of an aperture and selective removal of the passivation beneath the electron-beam-defined opening prior to the electrodeposition of the 3D structure (Figure 4.20 e). In both ways, free-standing 3D structures could be prepared that protrude from the passivation with their full height and thus

can be more easily engulfed by the cell. The fabrication of free-standing 3D structures is already well established in the literature. The approach in Figure 4.20 (e), for example, was employed by Lin *et al.* [50] for the preparation of iridium oxide nanohollows as well as gold nanopillars. The Spira group employs a different approach, first preparing the 3D structures, then covering the entire surface with a passivation layer, followed by wet-etching of the passivation on top of the mushrooms through apertures in a photoresist.[54,89,90] In addition to the expected improvement of the engulfment capabilities yielded by the fabrication of free-standing 3D structures, the elimination of an underlying planar electrode and low sealing in this area removes external influences and enables a direct investigation into the improvement in coupling efficiency yielded by the 3D design. However, due to the sensitivity of PMMA towards RIE processing and the challenges and poor mask stability encountered during the fabrication of hollow structures, no attempts at the preparation of free-standing designs were undertaken as part of this study.

An additional problem encountered during the reported electrophysiological studies was the poor stability of the employed passivation. In some cases, holes in the passivation (pinholes) could already be detected on the MEAs during the second cycle in cell culture, apparent by the presence of multi-peaks owing to the recording of one propagating action potential wave at different points along the feedline. Therefore, many measurements had to be discarded to prevent errors in the assignment of the recorded signal. Figure 4.21 shows macroscopic and microscopic images of the detachment of the silicon dioxide/silicon nitride layer. The low stability of the passivation

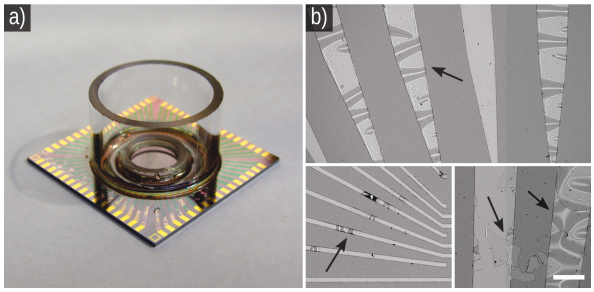

Figure 4.21: Macroscopic and microscopic images of the instability of the passivation. On some of the employed MEAs, the detachment was immediately visible due to pronounced passivation breakdown (a). Microscopic analysis could show the buckling and detachment of the silicon dioxide/silicon nitride layer on various MEAs (b). Scalebar represents 200 µm.

layer poses a significant problem for high impedance 3D nanoelectrode recordings. Defects such as cracks, pinholes, and delamination along the electrode feedline can lower the overall electrode impedance and shunt the electrode towards the surrounding electrolyte at ground potential. Even a few pinholes can effectively form low ohmic pathways to ground, which readily govern the overall

electrode impedance. Consequently, the signal amplitude of a 3D nanoelectrode can easily dissipate due to these parasitic elements. Figure 4.22 shows a schematic representation of the different influences on the signal amplitude V_{in} at the amplifier input. In the sensing area, the combined

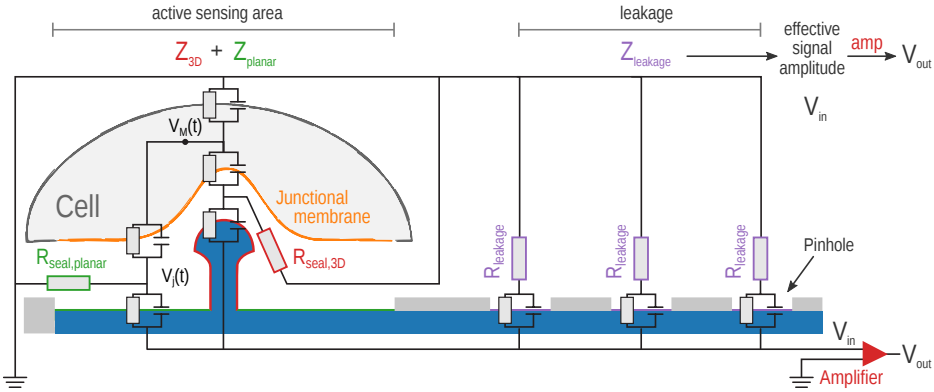

Figure 4.22: Schematic representation of the influences factoring into the signal amplitude V_{in} at the amplifier input. The potential at the cell-device interface V_j is determined through the combined local sealing both on the 3D electrode ($R_{seal,3D}$) and the planar area ($R_{seal,planar}$). If pinholes are present, the setup behaves like a voltage divider and V_{in} is dependent both on the impedance of the sensing area, as well as the impedance of the shunt ($Z_{leakage}$), resulting in a decrease in signal amplitude. $R_{seal,planar}$ pertains both to the planar area to the left and right of the 3D structure (green surface). The respective circuit components were omitted from the right planar sensing area for the sake of simplicity.

local sealing both on the 3D electrode ($R_{seal,3D}$) and the planar area ($R_{seal,planar}$) will determine the potential difference V_j against the bulk electrolyte (ground). In the ideal case, there is no further voltage drop between the signal at the cell-device interface V_j and the input of the amplifier and V_{in} is thus approximately equal to V_j.[144] However, many factors influence the ratio of V_j/V_{in}. The presence of pinholes in the passivation, for example, effectively forms a voltage divider and V_{in} will thus depend on the ratio of the impedance of both the sensing area and the shunt, which significantly reduces the signal amplitude and precludes the recording of high-amplitude signals. Therefore, the potentially high sealing achieved by introduction of the 3D electrode is negated if holes in the passivation are present. It is thus highly important to ensure a virtually leakage-free interface. This, however, is a considerable technological challenge. In addition to the attenuation of the signal amplitude, the problem of the low stability of the passivation limits the re-usability of the employed devices. This is particularly problematic for 3D MEAs since the processing time needed for the fabrication of the 3D structures considerably surpasses the processing time of planar

MEAs, making a good long-term stability a prerequisite for a sensible application of these devices. Moreover, for the investigation of neuronal networks and the long culturing time necessary for the establishment of network connectivity and electrophysiological activity, long-term stable devices are a fundamental requirement. For future studies into the influence of 3D electrodes on the recording capabilities of MEAs, several aspects are thus of utmost importance for a successful comparison. A more stable passivation is needed to enable high signal amplitudes as well as a better re-usability of the prepared MEAs, thereby facilitating a more in-depth study of the effect of 3D structures as well as the investigation of neuronal networks. Furthermore, investigations into the preparation of 'free-standing' structures should be conducted, which would reduce the analysis of the recording efficiency to the influence of the 3D design, facilitate a better engulfment by removing the necessity of cellular protrusion into the electrode aperture, and eliminate the contribution of the low sealing on the surrounding planar electrode. Finally, a more efficient cleaning protocol for the MEAs needs to be established to enable better cell adhesion. While cleaning with AR 600-71 and oxygen plasma improved the situation, more data is needed to draw reliable conclusions. In either case, good care has to be taken to remove all PMMA prior to SEM analysis.

Electroporation of HL-1 cells on 3D nanoelectrodes Despite the problems occurring during AP recordings, voltage pulses were applied as proof-of-principle study into the electroporation capabilities of the developed 3D structures. Electroporation aims to improve the coupling between cell and electrode via the reduction of the junctional membrane resistance. By application of a voltage pulse, pores are produced in the cellular membrane due to dielectric breakdown.[110] The protocol employed as part of this body of work was the application of 100 consecutive square biphasic pulses of 1 V in amplitude and period of 800 µs. Various different electroporation protocols have been reported in the literature. Xie *et al.*[98] employed 1.5 µm high Pt nanopillars of 150 nm in diameter to record action potentials from HL-1 cells with amplitudes of 100-200 μV_{p2p}. After application of 20 biphasic pulses of 2.5 V and 200 µs period, they were able to record APs of up to 11.8 mV_{p2p}. Resealing of the transient pores occurred within 10 min. Lin *et al.*[50] employed hollow IrOx pillars of 180 nm in outer diameter and 500 nm in height to record APs from HL-1 cells of 300 μV_{p2p}. They then applied a sequence of 100 consecutive square biphasic pulses of 400 µs period and 3.5 V amplitude, resulting in the detection of up to 15 mV_{p2p} signals that maintained their intracellular shape for up to an hour. The same electroporation protocol employed on gold

pillars resulted in much lower amplitude of 1.2 mV_{p2p}, which decayed to the extracellular signal within one minute. Fendyur *et al.*[109] investigated rat embryonic cardiomyocytes on mushroom-shaped 3D electrodes, recording signal amplitudes of around 500 μV_{p2p} prior to electroporation, and up to 6 mV_{p2p} after application of a single positive square pulse of 50 to 100 ms and 0.5 to 1 V amplitude. Resealing occurred within two to ten minutes. Hai *et al.*[112] applied alternating voltage pulses of 500 to 1000 mV and 10 ms period for 300 ms, resulting in an increase in signal amplitude from 200 μV_{p2p} before, to 6 mV_{p2p} after electroporation for *Aplysia* neurons cultured on mushroom-shaped structures. Recovery occurred within few minutes. The variations between electroporation protocols are thus significant. However, what they all have in common is the successful electroporation and resulting sharp increase in signal amplitude, as well as the decay of the amplitude back to the extracellular signal due to membrane resealing. Figure 4.23 shows an exemplary decay of the AP amplitude as observed during the first minute after application of an electroporation pulse via a 1 µm hollow mushroom. The amplitude of the signal prior to electroporation was 250 μV_{p2p}, which increased to 1.6 mV_{p2p} after electroporation, yielding a more than six fold increase in amplitude. Within the first 60 s, the amplitude decayed to 0.6 mV_{p2p}. In accordance with the data reported in the literature,[50,98,109] the signal shape of the action potential changes from a predominantly negative bi- or triphasic shape to positive biphasic after the application of the electroporation pulse, proving the intracellular access of the 3D electrode. With time,

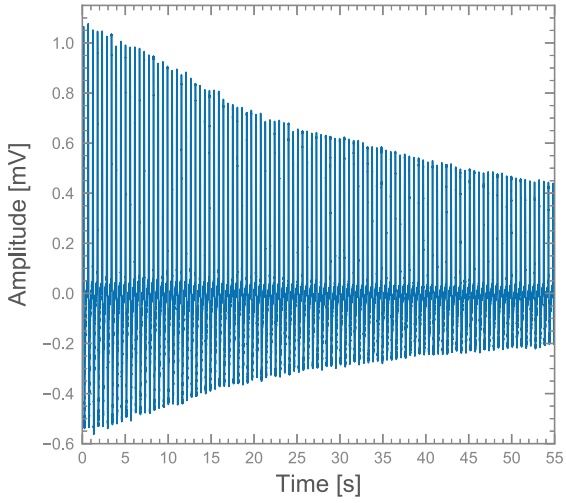

Figure 4.23: Exemplary amplitude decay after electroporation. While the initial amplitude prior to electroporation was 250 μV_{p2p}, the application of a voltage pulse results in a six fold increase in amplitude to 1.6 mV_{p2p} right after electroporation. Afterwards, the amplitude decays back to the extracellular level. This decay can last anywhere between one to tens of minutes.

the amplitude decays and the shape of the signal returns back to the extracellular shape (Figure 4.24). In many cases, however, the signal shape remained positive biphasic until it decayed to the

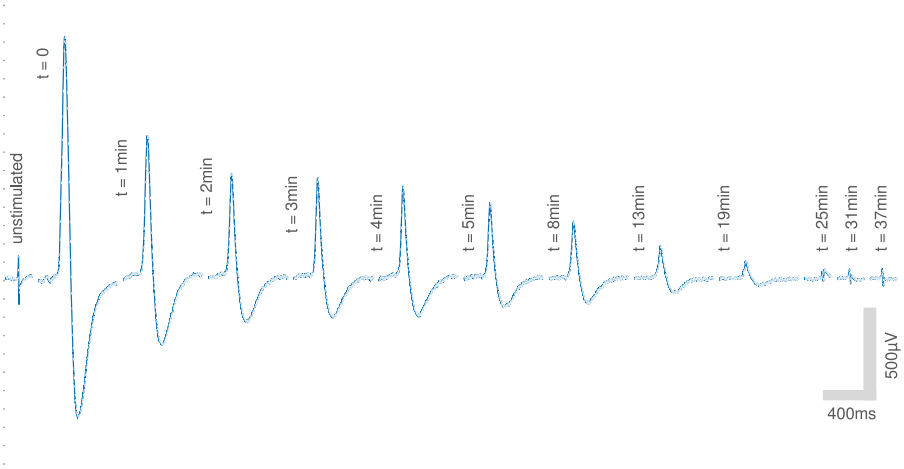

Figure 4.24: Exemplary amplitude development in the case of membrane resealing. Before electroporation, the recorded action potential has a low amplitude and is negative triphasic in shape. After electroporation, the shape changes to positive biphasic signals. The amplitude of the signal decays with time, followed by resealing of the membrane and return to the negative biphasic waveform observed prior to electroporation, which is in accordance with the results reported by Fendyur *et al.* [109] However, resealing does not occur in all cases.

noise level, suggesting that the cell was not able to reseal the pores and subsequently died. This effect is a deviation from the results reported in the literature, where the electroporation using 3D structures is described as a transient approach that does not result in detrimental effects for the cells. Potentially, this could mean that the amplitude of the applied pulse was too high. While Lin *et al.* [50] applied significantly larger pulses of 3.5 V in amplitude, they delivered the pulse solely via the 3D structure rather than via 3D structure and planar surrounding electrode. Furthermore, a direct comparison of the applied parameters is challenging since the effective potential at the cell-device interface will depend on the characteristics of both the device and the employed electronics. A different potential source of the problem could the more widespread electroporation resulting from the setting employed here. Since it was observed during this study that bare planar electrodes can also result in increased signal amplitudes after application of electroporation pulses, the resulting large-scale electroporation could be the cause for the observed behavior. In future studies, it would be interesting to investigate the cell viability after electroporation. Electroporation

in the presence of a membrane-impermeable fluorescent dye in conjunction with live-dead staining could provide valuable insight into the actual efficiency as well as harmfulness of the process.

In addition to the amplitude of the applied voltage pulse, the sealing between cell and electrode also has a strong influence on the effect of electroporation pulses since the electric field experienced by the cell will depend on R_{seal}. In order to investigate the influence of the cell-electrode contact on the efficiency of electroporation, the highest signal amplitudes obtained on each employed MEA after electroporation were compared with the amplitudes prior to the application of the electroporation pulse. Additionally, the highest amplitudes obtained prior to electroporation were compared with the amplitudes measured after the voltage pulse. Figure 4.25 shows the correlation between the electroporation-induced amplification and the unstimulated signals (a), as well as the occurrence of the different amplification factors (b). While high amplification factors of up to

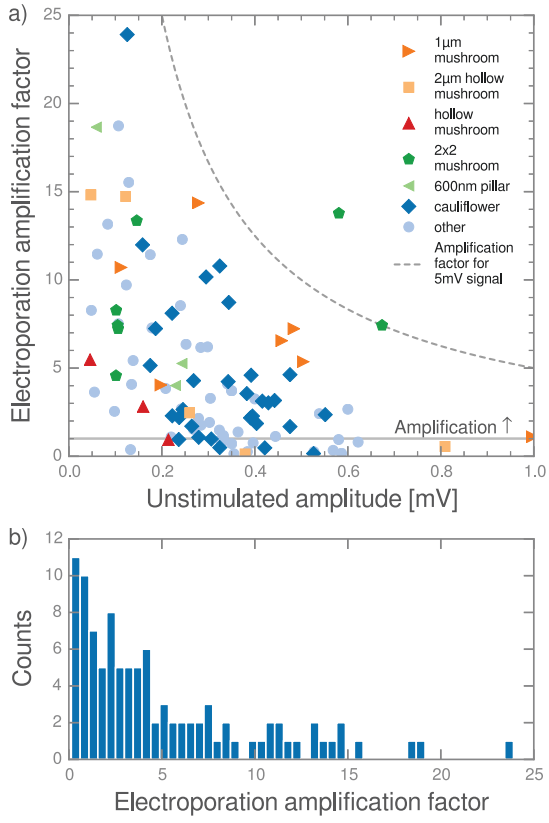

Figure 4.25: Effect of electroporation. (a) Depicts the correlation between the initial, unstimulated amplitude and resulting amplification. While high amplification factors of up to 23 times the initial amplitude could be observed for channels that exhibited a small unstimulated amplitude, electrodes exhibiting a high initial amplitude primarily resulted in signals that are smaller post-electroporation than they were before. The dotted line marks the amplification factor for each unstimulated amplitude needed to yield 5 mV signals after electroporation. (b) Histogram of the different amplification factors. While the amplification is in the range of two to eight times the initial signal amplitude in the majority of cases, up to a 23-fold increase in amplitude could be observed.

23 times the unstimulated amplitude were observed, these results still fall short of the 50 times amplification observed by Lin *et al.* on hollow IrOx nanopillars.[50] However, as with the unstimulated amplitudes, the reports in the literature often focus on the highest amplitude observed during the study, making a comparison of the different characteristics recorded within this body of work challenging. An expected effect is the decrease in amplification factor with increasing initial amplitude, since the amplitude that can theoretically be achieved is limited by the cellular signal. However, signals of higher initial amplitude primarily resulted in amplitudes that were lower post- than prior to the electroporation pulse for the data investigated here. This could be due to a better sealing between cell and electrode and thus greater and potentially irreversible effects of the applied electric field. Considering the small number of high-amplitude signals obtained during unstimulated recordings, however, this could also be a result of insufficient statistical power, which might also be a factor resulting in no determinable dependency of the electroporation-induced amplification on the employed 3D structure. While four solid mushrooms arranged in a 2x2 grid of 4 µm spacing resulted in the highest observed signals of 5 and 8 mV_{p2p}, which is equivalent to an amplification factor of 8 and 14, respectively, the data basis is insufficient to draw definite conclusions with respect to a potentially improved interaction employing this 3D structure arrangement.

4.3 Conclusion

Within this Chapter, the structures developed in Chapter 3 were transferred onto microelectrode arrays. It was shown that it is possible to achieve good control over the deposition of sets of eight nanoelectrodes, thereby facilitating the fabrication of various different 3D designs on a single chip. While the lack of temperature control results in slight variations in the development of the structure size between experiments conducted in summer and winter, the difference is small enough to employ the reported approach for real-time control of the structure size. Ultimately, this approach can even be used for a well-defined deposition of single nanoelectrodes, as was shown in a proof-of-principle study. In addition to MEAs containing hollow and solid structures of 800 nm stalk width, solid structures with diameters of 300 and 600 nm were prepared. While these nanoelectrodes could be prepared with high fidelity, more data is needed to enable a reliable correlation for the development of the size with t_{total} $t_{boundary}$ for these structures. The transfer of bigger hollow mushrooms to MEAs was successful only for 1 µm and 5 µm structures,

while adjustments of the electron-beam lithography parameters are needed to facilitate the production of 2 µm and 3 µm designs. Electrophysiological studies on HL-1 cells were conducted to investigate the influence of the different 3D structures on the recording capabilities of the devices. However, no notable increase in signal amplitude due to the introduction of 3D structures could be observed. The only 3D electrodes yielding a significantly higher signal amplitude as compared to their planar equivalent were cauliflower-like structures. However, their large size precludes their application for the investigation of neuronal networks due to the inherent limit of the engulfment capabilities of these cells.[56] Overall, several challenges were encountered during the reported study such as inconsistent cell adhesion, suboptimal 3D structure position with respect to the electrode opening, and low device stability owing to the degradation of the passivation. These factors preclude reliable conclusions with respect to the question of the increase in recording capability resulting from the presence of 3D structures. Improvements to the cleaning protocol for MEAs subject to electron-beam processing and thus PMMA residues as well as ideas circumventing the alignment problem were proposed. In this manner, it should be possible to determine the effect of the different 3D structures on electrophysiological recordings in future studies. Proof-of-principle experiments were performed to investigate whether electroporation and a subsequent increase in the signal amplitude are feasible with the system reported. While large amplification factors of up to 23 times the amplitude prior to the application of the voltage pulse were observed, no resealing of the formed pores could be detected in many cases, suggesting that the process induces cell death. Furthermore, electrodes yielding high-amplitude signals prior to electroporation often showed only an insignificant increase or even decrease in signal amplitude after the induction of pores in the membrane, suggesting that the sealing between cell and electrode greatly influences the electroporation efficiency as well harmfulness of the process. In future studies, investigations into the cell viability after application of electroporation pulses should be conducted, in conjunction with fluorescent labeling of electroporated cells with membrane-impermeable dyes.

Chapter 5

Modifications

As described in Chapter 2, the efficiency of MEA-based action potential recordings depends both on the sealing resistance between cell and electrode as well as the electrical properties of the device. Here, the electrode impedance plays a critical role, with a decrease in electrode size resulting in an increase in impedance and thus higher thermal noise during voltage-based action potential recordings.[18,146,147] This problem limits the spatial resolution of MEA-based devices since the downscaling needed for a higher electrode density and resulting single-cell resolution causes a significant decrease in signal-to-noise (S/N) ratio and thus applicability of the devices. Various approaches have been employed in the literature to increase the active surface area of planar microelectrodes while maintaining a small overall geometrical footprint. Thomas *et al.* already employed rough platinum surfaces (Pt black) in their first MEA publication in 1972,[4] effectively circumventing the problem of high impedance and recording high amplitude action potentials from embryonic chick cardiomyocytes. However, the low stability of platinum black renders these devices unfit for long-term usage. Since then, many different approaches have been employed to increase the surface area of MEA electrodes, ranging from improved fabrication approaches for Pt black,[24,26] micelle-templated porosity,[22] porous gold via silver-gold dealloying,[25,27] application of carbon nanotubes,[29,31,32] or conductive polymers. Since free-standing 3D structures on otherwise insulated MEAs as suggested in Chapter 4 exhibit a significantly lower surface area as compared to planar MEAs, decreasing the device impedance is critical for an adequate S/N ratio. This Chapter is thus concerned with the modification of 3D structures using a micelle templated approach for the introduction of porosity. Another method presented here is the modification of pillars and mushrooms by electrodeposition of PEDOT:PSS, a conductive polymer that can result

in a significant reduction in impedance. All data reported in this Chapter results from proof-of-principle investigations and is intended as impulse for future studies.

5.1 Experimental

5.1.1 Porous gold

All samples were prepared as described in Chapter 3 on page 40 using samples exhibiting 5 nm Ti and 50 nm Au on n-doped silicon. In addition to the Pur-A-Gold containing gold bath used in Chapters 3 and 4, two different additive-free gold bath compositions were prepared:

1. **Gold bath in ultrapure water:** 17.61 g/l $KAu(CN)_2$ (99.9% metal basis, Alfa Aesar, Karlsruhe, Germany), which is equivalent to 12 g/l Au. The pH of the solution was set to 7 using KOH and HCl

2. **Phosphate buffered gold bath:** 17.61 g/l $KAu(CN)_2$ (12 g/l Au), 40 g/l K_2HPO_4 (Sigma Aldrich, Steinheim, Germany), and 10 g/l KH_2PO_4 (Carl Roth GmbH + Co. KG, Karlsruhe, Germany) in ultrapure water

The solutions were used both as is, as well as supplemented with either polyethylene glycol p-(1,1,3,3-tetramethylbutyl)-phenyl ether (Triton X-100) (Sigma Aldrich, Steinheim, Germany) or polyoxyethylene (20) sorbitan monolaurate (Tween 20) (Sigma Aldrich, Steinheim, Germany). Dilutions were made at a ratio of 3 parts gold bath and 1 part surfactant in ultrapure water, yielding a $KAu(CN)_2$ concentration of 13.2 g/l and Au concentration of 9 g/l. Table 5.1 depicts the different combinations of gold bath and surfactant mixture investigated as part of this study, as well as the applied potential and final surfactant concentration. The electrodeposition was performed on a Biologic VSP-300 (Bio-Logic SAS, Claix, France) potentiostat using a three-electrode configuration with the sample as working, a Pt mesh as counter, and a Ag/AgCl pellet as reference electrode. The current was recorded with a 20 Hz sampling rate and a 50 kHz low-pass filter. After electrodeposition, the gold bath solution was removed, the samples washed with MilliQ water thrice and placed into acetone for PMMA removal. The acetone was exchanged twice to ensure full removal. The samples were dried in a stream of nitrogen and imaged at a LEO 1550 (Carl Zeiss AG, Oberkochen, Germany) scanning electron microscope at 20 kV acceleration voltage using inlens detection.

Table 5.1: Overview over different gold bath compositions investigated as part of this study.

Gold bath	Surfactant	Surfactant concentration	Gold concentration	Deposition potential
Pur-A-Gold 202B	Triton X-100	0.3 wt%	9 g/l	-1.15 V
	Triton X-100	0.5 wt%	9 g/l	-1.15 V
	Tween 20	5 wt%	9 g/l	-1.15 V
	Tween 20	7.5 wt%	9 g/l	-1.15 V
	Tween 20	10 wt%	9 g/l	-1.15 V
Ultrapure water	None	-	12 g/l	-1.10 V
	None	-	12 g/l	-1.25 V
	Triton X-100	0.3 wt%	9 g/l	-1.25 V
	Triton X-100	0.5 wt%	9 g/l	-1.25 V
	Triton X-100	2 wt%	9 g/l	-1.25 V
	Tween 20	5 wt%	9 g/l	-1.25 V
	Tween 20	7.5 wt%	9 g/l	-1.25 V
Phosphate buffered	None	-	12 g/l	-1.10 V
	None	-	12 g/l	-1.15 V
	None	-	12 g/l	-1.20 V
	None	-	12 g/l	-1.25 V
	Triton X-100	0.3 wt%	9 g/l	-1.25 V
	Triton X-100	0.5 wt%	9 g/l	-1.25 V
	Triton X-100	2 wt%	9 g/l	-1.25 V
	Tween 20	5 wt%	9 g/l	-1.25 V
	Tween 20	7.5 wt%	9 g/l	-1.25 V
	Tween 20	10 wt%	9 g/l	-1.25 V
	Tween 20	15 wt%	9 g/l	-1.25 V

5.1.2 Porous platinum

All samples were prepared with the solid template as introduced in Chapter 3 on page 40 using n-doped silicon substrates exhibiting 10 nm Ti and 100 nm Pt. A platinum plating solution was prepared consisting of a 60 mM H_2PtCl_6 (Hexachloroplatinic acid, MaTecK, Jülich, Germany) solution in ultrapure water and containing 0.1 wt% sodium dodecyl sulfate (SDS) (Sigma Aldrich, Steinheim, Germany). Additionally, solutions containing 45 mM H_2PtCl_6, 0.075 wt% SDS, and either 0.1, 0.5, or 1.0 wt% Triton X-100 (Sigma Aldrich, Steinheim, Germany) were employed. The electrodeposition was performed on a Biologic VSP-300 (Bio-Logic SAS, Claix, France) potentiostat using a three-electrode configuration with the sample as working, a Pt mesh as counter, and a Ag/AgCl pellet as reference electrode. Depositions were performed at -0.2 V against reference for various times, the

current was recorded with a 4 Hz sampling rate and a 5 Hz low-pass filter. After electrodeposition, the platinum bath solution was removed, the samples washed with MilliQ water thrice and placed into acetone for PMMA removal. The acetone was exchanged twice to ensure full removal. The samples were dried in a stream of nitrogen and imaged at a LEO 1550 (Carl Zeiss AG, Oberkochen, Germany) scanning electron microscope at 20 kV acceleration voltage using inlens detection.

5.1.3 PEDOT:PSS

PEDOT:PSS was electrochemically polymerized on solid pillars and mushrooms as prepared in Chapter 3 on page 40 at the Department of Bioelectronics (BEL) at MINES Saint-Étienne by David Ohayon and Sahika Inal. Briefly, a plating solution was prepared consisting of 0.1 M poly(sodium 4-styrenesulfonate) (PSSNa) and 0.01 M 3,4-ethylenedioxythiophene (EDOT). The electrodeposition was performed on an Autolab (Metrohm Autolab) potentiostat using a three-electrode configuration with the sample as working, a Pt electrode as counter, and a Ag/AgCl electrode as reference electrode. Depositions were performed at +1.0 V against reference for either 30 or 60 s. Electrochemical impedance spectroscopy (EIS) was conducted by David Ohayon and Sahika Inal both prior to and post deposition of PEDOT:PSS in phosphate buffered saline (PBS), employing a single sinusoidal excitation signal with an amplitude of 10 mV. All measurements were performed with 50 frequencies logarithmically spaced from 10 kHz to 0.1 Hz. The samples were cleaned with ultrapure water between each step. The resulting structures were investigated via scanning electron microscopy and energy-dispersive X-ray (EDX) spectroscopy at a Magellan 400 (FEI Deutschland GmbH, Frankfurt, Germany) SEM equipped with an X-Max 51 XMX0024 (Oxford Instruments GmbH, Wiesbaden, Germany) EDX detector.[117] SEM images were acquired at 3 kV acceleration voltage and a current of either 25 pA or 50 pA. EDX spectra were acquired at 5 kV acceleration voltage. Prior to cell culture, the samples were stored in ultrapure water for 3 h and then sterilized in 70% ethanol for 1 h. They were then transferred to a sterile workbench, placed into a 12-well dish containing ultrapure water, and rinsed with sterile water thrice. They were coated with 0.01 mg/ml poly-L-lysine hydrobromide (PLL) in 20 mM HEPES (pH 7.5) for 1 h at RT, rinsed with HEPES twice, and stored in HEPES at 4°C until just before cell seeding. Cortical neurons were prepared as described in Chapter 3 on page 44, 400 k cortical neurons were seeded onto each sample in 1.5 ml supplemented Neurobasal medium. The medium was exchanged against fresh, pre-warmed, supplemented Neurobasal medium in two steps of 750 µl each to prevent drying of the samples 1.5

hours after seeding. The cells were fixed after three days *in vitro* (DIV), followed by heavy-metal staining and resin embedding as described in Chapter 3 on page 46. Focused ion-beam sectioning was performed according to the parameters shown in Chapter 3 on page 47.

5.2 Results

5.2.1 Porous gold

The reduction of the electrode impedance has been the focus of numerous studies, with a variety of approaches being investigated such as the introduction of rough or porous metal surfaces,[4,20–28] carbon nanotubes,[29–32] to the application of conductive polymers.[33–36] Due to the small size of the 3D nanoelectrodes prepared within this body of work, increasing the surface area via porosity could help alleviate the problem of high impedance. For this study, preparing the 3D structures on planar MEAs of either 12 or 24 µm aperture size results in low impedance and thus noise during voltage-based action potential recordings. If the 3D structure is to be free-standing as single interaction point on an otherwise passivated MEA as suggested in Chapter 4, however, the electrode impedance can be expected to pose a significant problem. Thus, the introduction of a rough surface could be a prerequisite for the successful application of these devices. Inspired by the publication of Heim *et al.*,[22] surfactants were added to the electroplating solution in order to introduce porosity. If the surfactant is employed at concentrations above the critical micelle concentration (cmc), the resulting micelles can mask a volume where no metal deposition occurs during electroplating, thereby facilitating the formation of a porous metal structure (Figure 5.1). In this manner, the surface area can be increased while maintaining the same geometrical footprint. Applying this

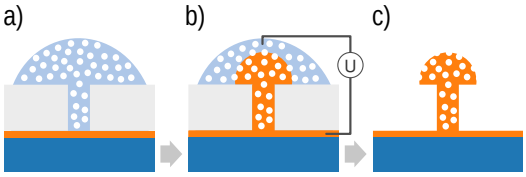

Figure 5.1: Schematic representation of the concept employed for the fabrication of porous 3D structures: The addition of surfactant at concentrations above the cmc (a) can result in the formation of porous structures during electrodeposition (b,c) due to the exclusion of the plating bath from the micelle volume.

approach to prepare porous Pt electrodes, Heim *et al.*[22] were able to decrease the impedance of 12 µm electrodes by up to an order of magnitude. Initially, deposition of porous gold was attempted by addition of either Triton X-100 or Tween 20 to the gold bath composition employed in

Chapters 3 and 4. Both Triton X-100 and Tween 20 are non-ionic surfactants, with a cmc of 0.08 to 0.24 mM[148–150] and 0.01 to 0.06 mM,[149,151] respectively. This is equivalent to approximately 0.005 to 0.016 wt% for Triton X-100 and 0.001 to 0.007 wt% for Tween 20. At 25°C, both surfactants form micelles with diameter in the range of around 5 to 8 nm.[150–154] An advantage of non-ionic surfactants for the application during electrodeposition experiments is the limited influence of the electrolyte on the physicochemical characteristics of the additive.[155] Both surfactants have been used in the literature to influence the characteristics of electrochemically deposited layers of various metals. During the electrodeposition of Zn on stainless steel, for example, Triton X-100 inhibits the adhesion of Zn, displaces the reduction potential to more negative values, and reduces the rate of mass transfer.[156] During the deposition of MnO_2, higher nucleation rates were achieved in Triton X-100 containing compositions, though the concentration of the surfactant had a critical influence in this case, with concentrations above 10 mM (0.67 wt%) resulting in a reduction in nucleation rate due to the increase in viscosity as expected for concentrations above the cmc.[155] Furthermore, the effect of the surfactant was found to depend on the nature of the employed metal ion, with Tween 20 retarding the deposition of tin but not influencing the deposition of manganese in experiments conducted by Chen *et al.*[157] For the study presented here, the surfactants were added to the gold bath at concentrations of either 0.3 wt% or 0.5 wt% for Triton X-100, while Tween 20 was investigated at concentrations of 5, 7.5, and 10 wt%. Figure 5.2 shows SEM top-view images of structures obtained by deposition from the Pur-A-Gold 202B gold bath with the two surfactants at -1.15 V. As can be seen, the utilization of Triton X-100 does not result in the formation

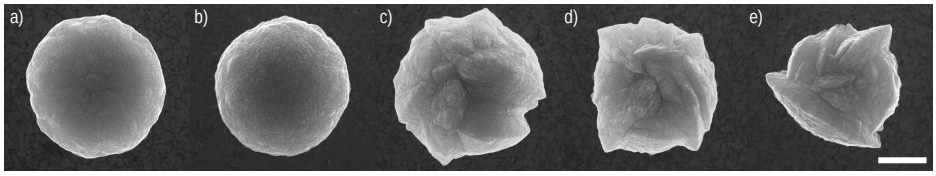

Figure 5.2: SEM top-view images for 3D structures deposited from Pur-A-Gold 202B supplemented with (a) 0.3 wt% Triton X-100, (b) 0.5 wt% Triton X-100, (c) 5 wt% Tween 20, (d) 7.5 wt% Tween 20, and (e) 10 wt% Tween 20. While Triton X-100 seems to have a smoothing effect, Tween 20 results in the formation of spiky deposits. Scalebar represents 500 nm.

of porous structures, but rather seems to cause a smoothing of the surface. For the most part, the addition of Tween 20 merely resulted in the formation of spiky deposits. While porosity could be observed for depositions from Tween 20 containing solutions in rare cases, the surfactant proved

to be instable in Pur-A-Gold 202B, precipitating and forming a thick layer on the gold surface and thus precluding reproducible results. In general, the additives contained in the Pur-A-Gold 202B composition make the addition of further surfactants challenging. SDS, for example, immediately precipitates when added to Pur-A-Gold 202B even at concentrations below the cmc. To circumvent the problems arising from the unknown composition of the proprietary Pur-A-Gold 202B solution, two additive-free gold baths were prepared, either containing solely $KAu(CN)_2$ in ultrapure water, or the gold salt in phosphate buffer, as suggested by Kohl.[69] Figure 5.3 shows the deposits obtained from these bath compositions without addition of surfactants for the deposition at different potentials. For both compositions, increasing the potential to more negative values results

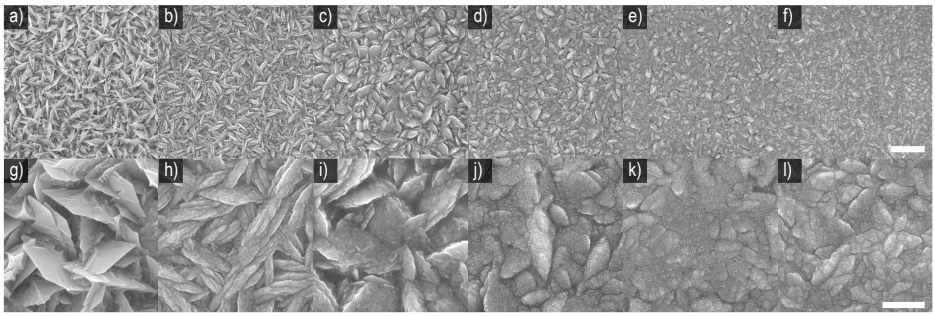

Figure 5.3: SEM images of the crystal structures obtained for Pur-A-Gold 202B free gold bath compositions at different potentials. (a,g) Ultrapure water, -1.10 V; (b,h) Ultrapure water, -1.25 V; (c,i) Phosphate buffered, -1.10 V; (d,j) Phosphate buffered, -1.15 V; (e,k) Phosphate buffered, -1.20 V; (f,l) Phosphate buffered, -1.25 V. For both bath compositions, higher potentials result in smoother surfaces, as expected from the literature.[78] Scalebar represents 2 µm (a-f) and 500 nm (g-l).

in smoother deposits. This is expected from the literature, where the application of low current densities and thus low overpotential was shown to result in a preferential growth at existing seeds and thus sharp, spiky deposits, while higher current densities result in the formation of more seeds and thus smoother surfaces.[78] However, at equal applied potential, the gold bath in ultrapure water forms much sharper, leaf-like crystals than the phosphate buffered composition. This could be due to the ohmic drop within the electrolyte. Since no supporting electrolyte is present in the ultrapure water bath, the ohmic resistance of the bath is expected to be significantly higher than for the phosphate buffered case. Thus, the increased voltage drop across the solution between reference and working electrode will result in a smaller effective potential and thus lower overpotential at the electrode surface in the case of the non-buffered gold bath.[70] Subsequently, the effect of

Triton X-100 and Tween 20 on the morphology of the deposits was investigated. Figures 5.4 and 5.5 show the results obtained for depositions with different concentrations of the two surfactants in ultrapure water and phosphate buffered gold bath, respectively. Since the deposition with these compositions were markedly slower than with Pur-A-Gold 202B, the potential was increased to -1.25 V for all of these experiments.

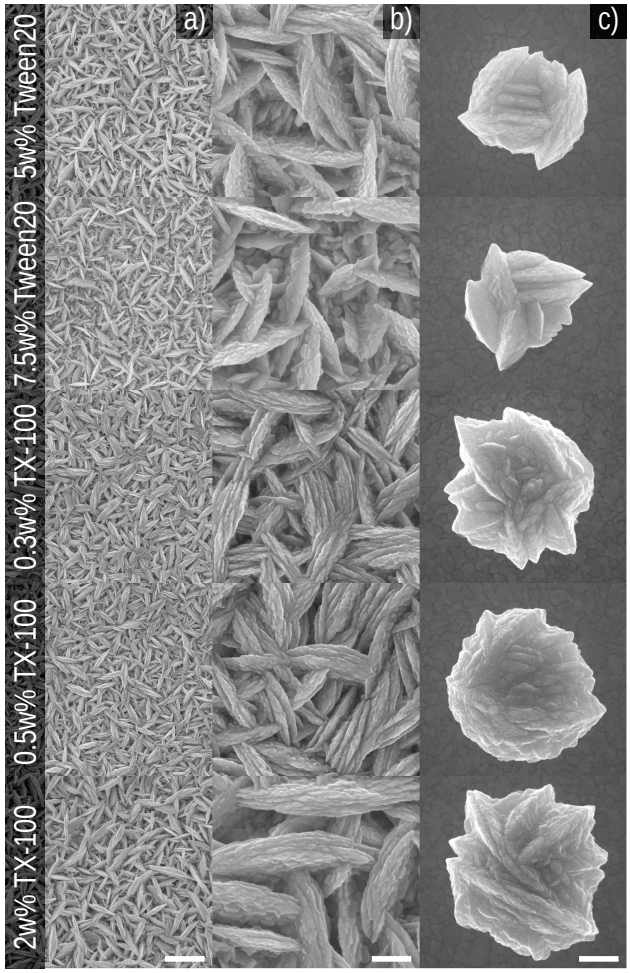

Figure 5.4: SEM images of structures obtained by addition of Triton X-100 and Tween 20 to the ultrapure water gold bath. (a) Crystal structure in area of laterally-unrestricted growth. (b) Higher magnification of (a). (c) Crystal structure on 3D structures. As compared to the deposition in the surfactant-free gold bath in ultrapure water, only a minor change in the crystal morphology can be observed, with leaf-like structures formed in the presence of Tween 20, and stacked leaf-like structures or slate-like structures formed upon addition of Triton X-100. All depositions were performed at -1.25 V against Ag/AgCl. Scalebar in (a) represents 2 µm, scalebar in (b) and (c) is 400 nm.

While the addition of surfactants only results in a minor change in crystal morphology in the case of the gold bath formulation in ultrapure water, with the addition of Tween 20 resulting in leaf-like

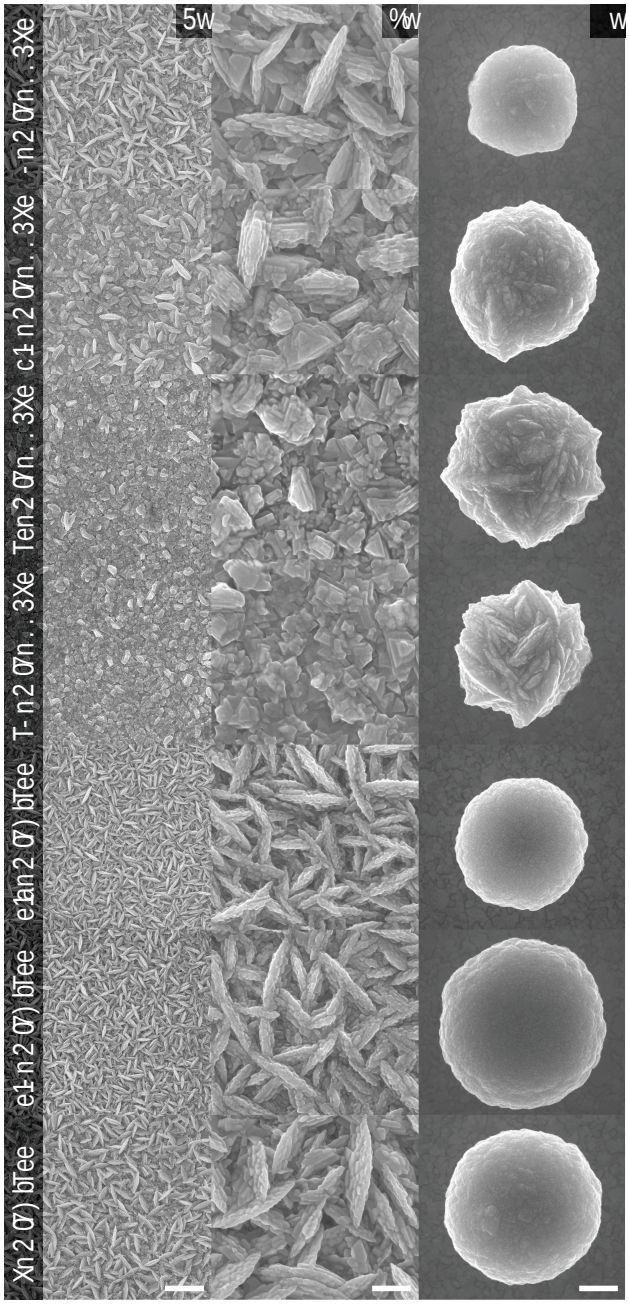

Figure 5.5: SEM images of structures obtained by addition of Triton X-100 and Tween 20 to the phosphate buffered gold bath. (a) Crystal structure in an area of laterally-unrestricted growth. (b) Higher magnification of (a). (c) Crystal structure on 3D structures. The crystal structure differs significantly between unobstructed and template-restricted areas. While the morphology changes from leaf-like to granular upon addition of Tween 20 in (a) and (b), the morphology of the 3D structures changes from smooth to leaf-like with increasing Tween 20 concentration. Triton X-100 results in leaf-like structures in (a) and (b) at all concentrations, while the 3D structures exhibit a smooth surface. All depositions were performed at -1.25 V against Ag/AgCl. Scalebar in (a) represents 2 µm, scalebar in (b) and (c) is 400 nm.

structures and addition of Triton X-100 yielding stacked leaf-like or slate layer-like deposits, the crystal morphology of deposits from phosphate buffered gold bath shows a strong dependency on the nature and concentration of the additives. Gradually increasing the concentration of Tween 20 from 5 wt% to 15 wt% resulted in the transition from leaf-like crystals to granular or pyramidal topographies in areas without restriction of lateral growth. In contrast, the 3D structures transition from smooth to spiky surface topographies upon increase in the Tween 20 concentration. The same discrepancy between unobstructed and template-constricted growth could be observed by addition of Triton X-100, where all 3D structures exhibited smooth surfaces, while leaf-like structures were observed in template-free areas. The addition of K_2HPO_4 and KH_2PO_4 thus seems to greatly influence the behavior of the surfactant during the electrodeposition. Since no porosity could be observed with any of the investigated gold bath/surfactant combinations employed here, no further studies into the reasons for the observed effects were conducted. However, while unsuitable for the introduction of porosity, both Triton X-100 and Tween 20 result in a variety of interesting surface topographies that could be employed for the preparation of microelectrode arrays with high surface area. While the effect is not sufficient for the necessary change in the impedance of free-standing 3D structures, the increase in surface area could be employed on planar MEAs as alternative to *e.g.* the more complicated introduction of surface roughness via electrodeposition into templates of nanoporous alumina.[21] In addition to the potential improvements for voltage-based action potential recordings, the high surface area produced in this manner could pose an advantage by introduction of a higher degree of surface-bound biochemical probes and resulting signal amplification for example during the detection of various targets on MEAs modified as electrochemical aptamer-based sensors.[158,159] Since the introduction of porosity via a template-assisted deposition seems to be challenging with gold, alternative approaches need to be considered such as the deposition of a gold and silver alloy, followed by dissolution of the silver as reported by Chapman *et al.*[25]

5.2.2 Porous platinum

As an alternative to porous gold, the fabrication of porous platinum was investigated, which has been shown to be feasible by addition of surfactants to the plating bath.[22,92] While Heim *et al.*[22] employed a mixture of 42 wt% octaethylene glycol monododecyl ether and 29 wt% hexachloroplatinic acid (H_2PtCl_6) hydrate in 29 wt% water, Park *et al.*[92] employed Triton X-100 (50 wt%) and

H_2PtCl_6 (5 wt%) in an aqueous solution containing 0.3 M NaCl (45 wt%). Both groups reported the formation of porous platinum for the bath compositions employed. Hexachloroplatinic acid is often used for the deposition of platinum black, highly porous platinum layers exhibiting significantly decreased impedance.[16,17] However, Pt black suffers from poor long-term stability. In contrast, the application of a micelle-templated approach yielded surfaces of low impedance and improved mechanical properties as compared to platinum black.[22,92] The deposition of Pt from H_2PtCl_6 occurs via a two step process[160]

$$\begin{aligned} PtCl_6^{2-} + 2e^- &\leftrightarrows PtCl_4^{2-} + 2Cl^- && E_0 = 0.77\,V\,[161] \\ PtCl_4^{2-} + 2e^- &\leftrightarrows Pt + 4Cl^- && E_0 = 0.75\,V\,[161] \\ \hline PtCl_6^{2-} + 4e^- &\leftrightarrows Pt + 6Cl^- && E_0 = 0.76\,V\,[161] \end{aligned} \tag{5.1}$$

with all potentials given with respect to the normal hydrogen electrode. Here, H_2PtCl_6 is used at a concentration of 45 mM in combination with 0.075 wt% SDS and either 0.1, 0.5, or 1.0 wt% Triton X-100. The resulting morphologies are compared with deposits from a solution of 60 mM H_2PtCl_6 and 0.1 wt% SDS in water. All depositions were conducted at a potential of -0.2 V against Ag/AgCl and employing solid templates prepared on platinum coated silicon as described in Chapter 3 on page 40. Figure 5.6 shows the 3D structures obtained for the different bath compositions. While the regular Pt bath results in very smooth deposits, the surface of 3D mushrooms deposited in the presence of 0.1 wt% Triton X-100 is notably rougher. Both 0.5 wt% and 1.0 wt% Triton X-100 result in the formation of highly granular surfaces, suggesting not only an influence of the formed micelles on the introduction of porosity, but also a shift to a high nucleation rate, which is in accordance with the results obtained by Devaraj *et al.* for the deposition of MnO_2.[155]

One problem occurring during these experiments was an insufficient exposure of the templates as can be seen in Figure 5.7. It seems that the parameters employed for PMMA on gold cannot be directly adopted for the fabrication of 3D structures on platinum. This problem also resulted in much fewer structures per sample, either due to insufficient stability of the structure/substrate contact resulting in the detachment of the 3D design, or underdeveloped templates that do not enable the contact between substrate and plating bath during the deposition. For future studies, the e-beam lithography parameters thus need to be adjusted to enable the fabrication of adequately exposed templates. Nevertheless, the obtained results with respect to the crystal morphology are

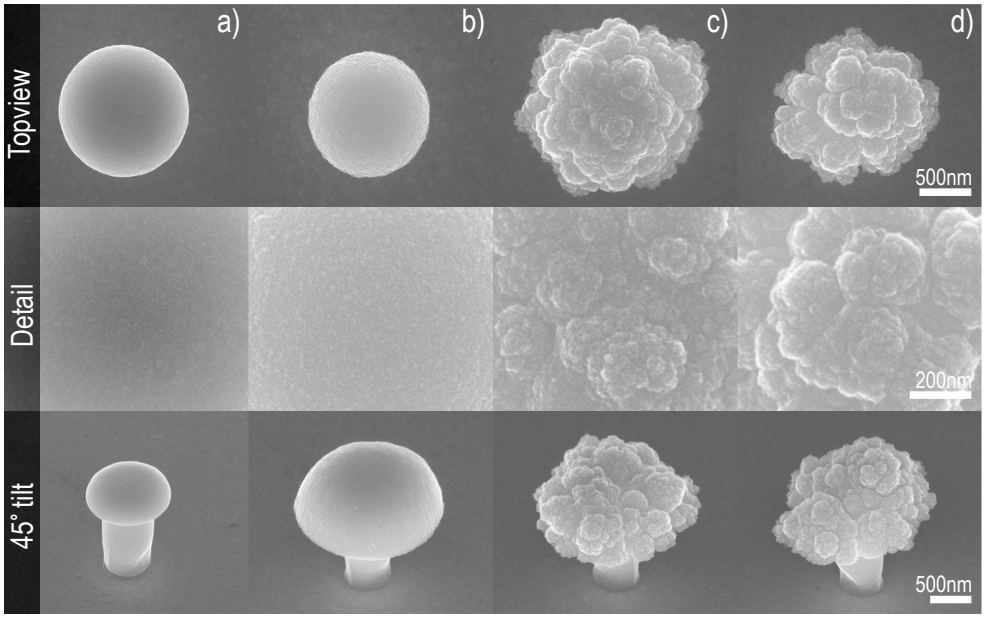

Figure 5.6: SEM images of three-dimensional Pt structures obtained from deposition using (a) the unsupplemented Pt bath, (b) Pt bath containing 0.1 wt% Triton X-100, (c) Pt bath containing 0.5 wt% Triton X-100, and (d) Pt bath containing 1.0 wt% Triton X-100. While the regular Pt bath yields smooth structures (a), the addition of 0.1 wt% Triton X-100 results in an increase in surface roughness, while both 0.5 wt% and 1.0 wt% Triton X-100 increase the surface roughness and change the crystal morphology.

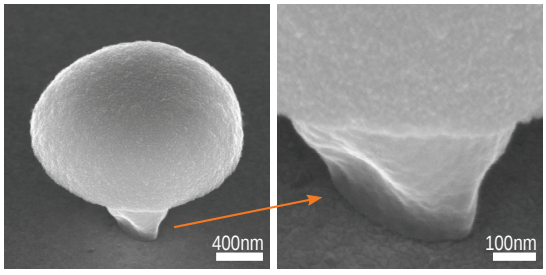

Figure 5.7: SEM images of mushroom-shaped Pt structures. The very narrow foot of the structure suggests that a higher dosis during electron-beam processing is needed to fully expose the structures on Pt substrates. Images acquired at 45° sample tilt.

promising. Further experiments have to be conducted to determine the change in impedance yielded with this approach. Additionally, investigations into the stability of the solution are essential since it could be shown in the literature that Triton X-100 can be oxidized in the presence of metals,[162,163] which could result in the precipitation of elemental platinum and thus insufficient long-term stability of the plating bath.

5.2.3 PEDOT:PSS

Another approach for the reduction of the device impedance employed as part of this Chapter is the application of poly(3,4-ethylenedioxythiophene):poly(4-styrenesulfonate) (PEDOT:PSS) (Figure 5.8). PEDOT:PSS is a conductive polymer exhibiting both electrical as well as ionic conduc-

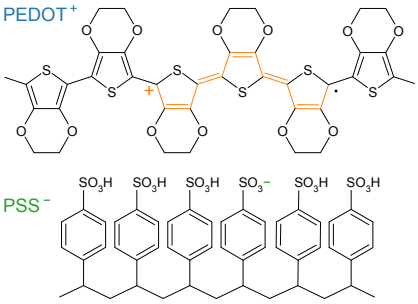

Figure 5.8: Chemical structure of PEDOT:PSS. The thiophene polymer is doped with poly(4-styrenesulfonate) to increase conductivity and enable electropolymerization from aqueous solution by increasing the solubility of the EDOT monomer. Figure from [164]

tance,[164] facilitating better transduction of the cellular signal by improving the transition between the biological and electrical conduction mechanism.[146] Furthermore, the rough polymer surface and penetration of ions into the layer result in a significant decrease in electrode impedance, with Cui *et al.*[33] reporting a decrease in impedance of up to two orders of magnitude at 1 kHz after PEDOT deposition. PEDOT can be electrodeposited from aqueous solution by addition of surfactants to counteract the poor solubility of the EDOT monomer in water.[35] Figure 5.9 depicts the envisioned fabrication scheme for the PEDOT deposition on mushroom-shaped 3D electrodes. EDOT molecules are electro-oxidized, followed by radical recombination and deprotonation. Multiple iterations of this process result in chain growth and thus the coverage of the 3D structure with a

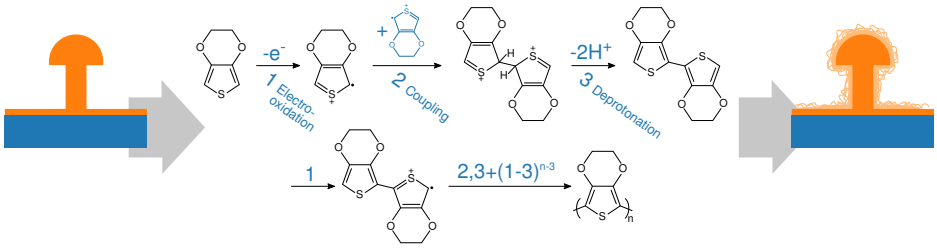

Figure 5.9: Mushroom-shaped 3D structures as prepared in Chapter 3 can be functionalized with PEDOT by electrodeposition. EDOT is first oxidized (1) followed by radical recombination (2) and deprotonation (3) to form an EDOT dimer. This process can be repeated to form longer polymer chains, covering the 3D structure. PSS is incorporated into the layer as counter ion (not shown). Polymerization adapted from [165,166]

polymeric layer. PSS is incorporated into the layer as counter ion.

3D gold structures were prepared as described in Chapter 3 and coated with PEDOT:PSS at the Department of Bioelectronics (BEL) at MINES Saint-Étienne by David Ohayon and Sahika Inal. Subsequently, the structures were analyzed via scanning electron microscopy (SEM) and energy-dispersive X-ray (EDX) spectroscopy to prove the presence of PEDOT. SEM images acquired after the electrodeposition of PEDOT:PSS show a rougher, more uneven surface as compared to the unmodified samples shown in Chapter 3, which is in accordance with the presence of a polymeric layer (Figure 5.10). However, significant differences in the surface characteristics could be observed.

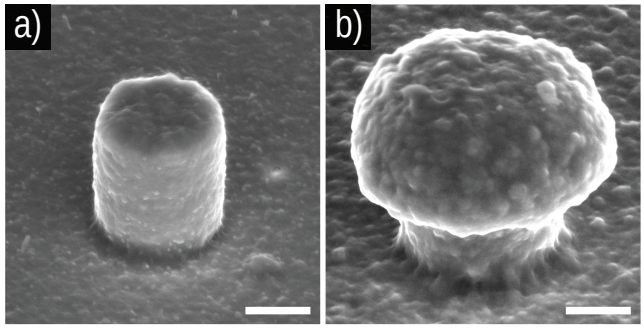

Figure 5.10: PEDOT:PSS covered pillar (a) and mushroom (b), both electrodeposited with PEDOT:PSS for 30 s. The well-preserved edges in (a) suggest a thinner PEDOT:PSS layer than in (b), where a granular PEDOT:PSS coating evens out the details of the 3D structure. Scale-bars represent 500 nm.

While the pillar in Figure 5.10 (a) exhibits well-preserved edges, suggesting a thin PEDOT:PSS layer, the structure in Figure 5.10 (b) is covered by a granular layer that markedly smooths the characteristics of the underlying mushroom-shaped structure. This indicates a thicker polymeric layer, despite both Figure 5.10 (a) and (b) being electrodeposited with the polymer for the same amount of time. Furthermore, while some of the samples were evenly covered with the PEDOT:PSS layer, other samples exhibit an uneven distribution, either with areas showing good coverage (Figure 5.11 a) while others are left bare (Figure 5.11 b), or with the formation of PEDOT:PSS islands (Figure 5.11 c). This could for example be due to a non-uniform wetting at the beginning of the deposition or the result of residual PMMA masking the surface and thus preventing the electro-oxidation of the EDOT monomer.

In order to prove the presence of PEDOT, the samples were investigated via EDX spectroscopy, where the sulfur atoms both in PEDOT and in PSS can be identified via their K_α line at 2.30 keV.[167] However, while this signal was distinct for thick polymeric layers (Figure 5.12, right), the underlying M-series gold signal is more pronounced than the sulfur signal for thinner layers of PEDOT:PSS

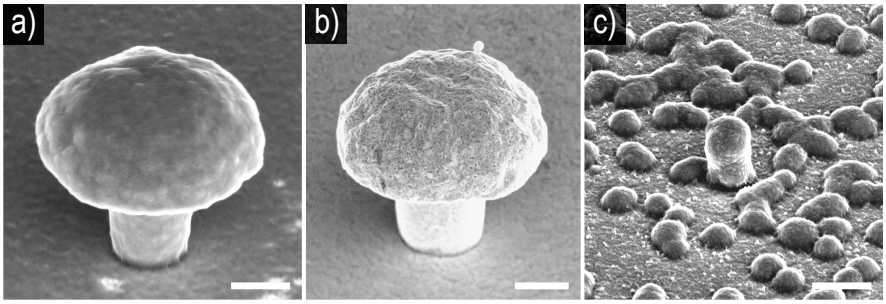

Figure 5.11: Problems encountered during PEDOT:PSS deposition: On some samples, significant differences in PEDOT coverage could be observed with some areas exhibiting good coverage (a) while others are left bare (b). On other samples, the deposition resulted in the formation of PEDOT:PSS islands (c). Scalebars in (a) and (b) represent 500 nm, scalebar in (c) represents 1 µm.

and sulfur can only be properly detected when investigating the edges of 3D structures (Figure 5.12, left). Nevertheless, the presence of sulfur could be proven in all areas covered with the polymeric layer. Furthermore, electrochemical impedance spectroscopy was performed prior to and after electrodeposition of PEDOT:PSS. Figure 5.13 shows an exemplary impedance trace for 3D

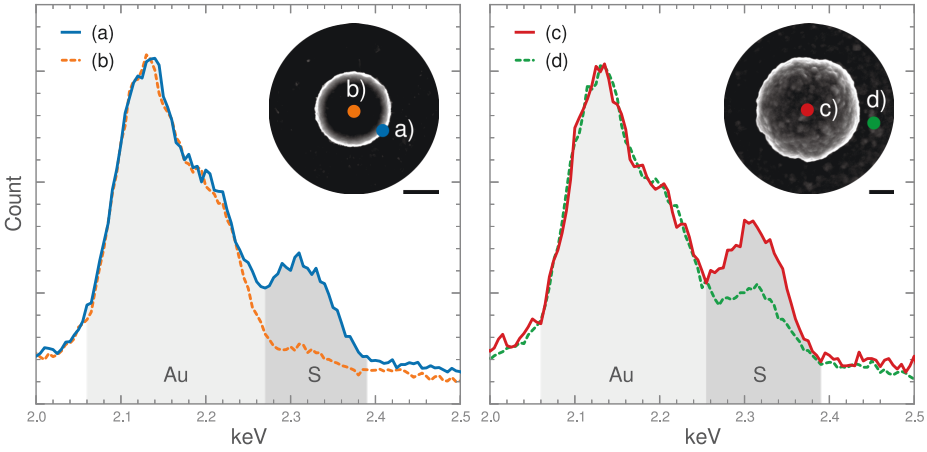

Figure 5.12: EDX spectra acquired at different positions for a PEDOT:PSS covered pillar (left) and mushroom (right) stemming from the samples in Figure 5.10. While the seemingly thinner coating of the pillar necessitates the detection of the sulfur groups at the edge of the structure (a) to prevent an overshadowing by the M-series signal of the underlying gold (b), the rough, seemingly thick PEDOT:PSS layer on the right yields enough sulfur signal to enable the detection despite the underlying gold, both on top of the structure (c) as well as the underlying substrate (d). Traces normalized to equal Au signal height for better comparability. Scalebars represent 500 nm.

mushrooms and 3D pillars before and after PEDOT:PSS deposition. While it has to be noted that this data was acquired from gold-on-silicon samples containing thousands of 3D structures and a poorly defined overall area, fitting of the impedance data in Figure 5.13 with a simplified Randles cell (R2+R1/C1) as equivalent circuit can nevertheless provide insight into the general influence of PEDOT:PSS. The pillars in Figure 5.13 yield 18 µF prior to and 880 µF after electrodeposition of PE-

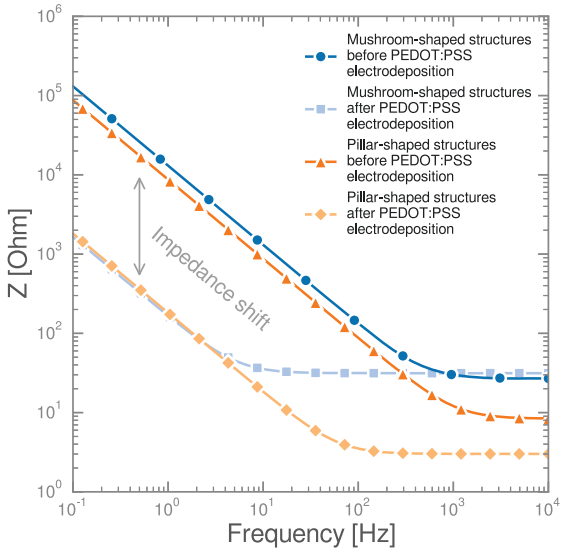

Figure 5.13: Impedance of pillars and mushrooms before and after PEDOT:PSS deposition. In the low frequency range, the impedance decreases by up to two orders of magnitude after the modification with PEDOT:PSS.

DOT:PSS, while the mushroom-shaped structures yield 12 µF before and 970 µF after PEDOT:PSS deposition. In both cases, the modification with PEDOT:PSS results in a significant increase in capacitance and thus decrease in impedance.

To investigate the biocompatibility of the PEDOT:PSS surfaces, embryonic rat cortical neurons were seeded on poly-L-lysine (PLL) coated PEDOT:PSS samples exhibiting mushroom-shaped 3D structures. The cells were fixed at 3 DIV, cellular membranes were stained with heavy metals to facilitate good contrast for electron microscopy, they were embedded in epoxy resin, and the interface was investigated via focused ion-beam sectioning. Overall, good cell adhesion and neurite outgrowth could be observed on the sample (Figure 5.14 a). While no full engulfment of the 3D structures could be discovered (Figure 5.14 b), the good contact on the planar surrounding PEDOT:PSS layer suggests that this is not due to the chemical influence of the polymer, but could result from the large cap size of 2 µm being above the inherent threshold of the engulfment capa-

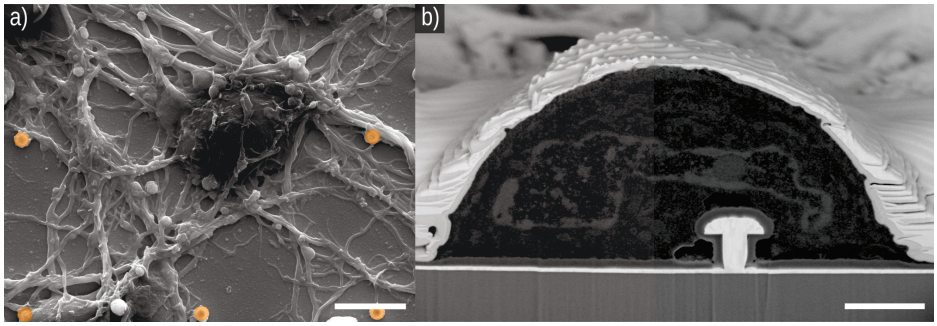

Figure 5.14: (a) SEM image of embryonic rat cortical neurons growing on PEDOT:PSS covered surfaces and showing good adhesion and neurite outgrowth after 3 DIV. The position of 3D structures is marked in orange. (b) Focused ion-beam section through a neuron on a PEDOT:PSS covered mushroom. While the cell does not fully engulf the structure, the good cellular adhesion on the planar surrounding sample suggests good biocompatibility. The thickness of the PEDOT:PSS layer in (b) is around 225 nm and results from the deposition at 1.0 V for 30 s. Scalebar in (a) represents 10 µm, scalebar in (b) is 2 µm.

bility of these cells. For the sample investigated here, the deposition of PEDOT:PSS at 1.0 V against reference for 30 s resulted in the formation of an approximately 225 nm thick polymeric layer that evenly covers both the planar surface as well as the 3D structures. It can thus be concluded that 3D electrodes can easily be coated with PEDOT:PSS via electropolymerization, yielding surfaces of reduced impedance and good biocompatibility. However, additional investigations into the deposition process have to be performed in order to receive reproducible results with respect to the PEDOT:PSS distribution on the surface. Furthermore, the long-term stability of the polymeric layer has to be studied since reports in the literature suggest that electrodeposited conductive polymers exhibit poor adhesion on metals,[78] potentially quickly resulting in delamination. Afterwards, the transfer to MEA electrodes and subsequent investigation into the impedance change has to be conducted. Finally, the PEDOT:PSS functionalized 3D electrodes can be employed for electrophysiological recordings to probe for the improvement yielded by the PEDOT:PSS coating.

5.3 Conclusion

This Chapter reports various proof-of-principle investigations into modifications of the 3D structures developed in Chapter 3, aiming at an increase in surface area and thus reduction of device impedance. Initially, surfactants were added to the commercial Pur-A-Gold 202B gold bath, aiming to introduce porosity via the formation of micelles and resulting excluded volume during the

electrodeposition. The poor solubility of various employed surfactants resulted in the development of two gold bath compositions not containing the Pur-A-Gold 202B supplement. However, while a variety of different surface morphologies were observed, no porosity could be achieved, neither with Triton X-100 nor Tween 20. In contrast, addition of Triton X-100 to a solution containing hexachloroplatinic acid resulted in a significant increase in roughness as compared to structures deposited from the unmodified platinum bath. As an alternative to the modification of the metal surface, the deposition of the conductive polymer PEDOT:PSS was investigated and found to result in a marked reduction in device impedance. Embryonic rat cortical neurons showed good adhesion and neurite outgrowth on the polymer-functionalized surfaces, proving the applicability of this approach for the modification of the cell-device interface.

Chapter 6

Conclusion and Outlook

Within this body of work, solid pillars and mushrooms as well as hollow pillars and mushrooms of various sizes were made available through a common fabrication scheme, thereby facilitating a parallel production of the different 3D designs. Through the downscaling of the deposition process, it became possible to monitor the nanoscale characteristics of the structures by observation of changes in the recorded galvanization current. Focused ion-beam sectioning showed good engulfment of the fabricated 3D structures both by HL-1 cells and embryonic rat cortical neurons. However, in contrast to the expectations resulting from a report of pronounced cellular protrusion into hollow structures,[50] only a slight bending into the opening could be observed for HL-1 cells on hollow pillars of 800 nm in diameter, while cortical neurons actively bend away from the opening. Even for large openings of several micrometers in diameter, cellular protrusion of HL-1 cells could not be observed with high fidelity. Nevertheless, the developed structures were transferred onto microelectrode arrays. Good real-time control over the structure characteristics of sets of eight nanoelectrodes was demonstrated through the establishment of a structure/size relationship. This approach facilitates the fabrication of various different 3D designs on a single chip, thus paving the way for a direct comparison of the different designs. While the lack of temperature control results in slight variations in the structure size between experiments conducted in summer and winter, the difference is small enough to employ the reported approach for real-time control of the structure size. Ultimately, this method can even be used for a well-defined deposition of single nanoelectrodes, as was shown in a proof-of-principle study.

Electrophysiological studies on HL-1 cells were conducted to investigate the influence of the different 3D structures on the recording capabilities of the devices. However, no notable increase

in signal amplitude due to the introduction of 3D structures could be observed. The only 3D electrodes yielding a significantly higher signal amplitude as compared to their planar equivalent were cauliflower-like structures. However, their large size precludes their application for the investigation of neuronal networks due to the inherent limit of the engulfment capabilities of these cells.[56] Overall, several challenges were encountered during the presented investigations such as inconsistent cell adhesion, suboptimal 3D structure position with respect to the electrode opening, and low device stability due to the degradation of the passivation. These issues preclude reliable conclusions with respect to the question of the increase in recording capability resulting from the presence of 3D structures. Proof-of-principle experiments were performed to investigate whether electroporation and a subsequent increase in the signal amplitude are feasible with the system reported. While large amplification factors of up to 23 times the amplitude prior to the application of the voltage pulse were observed, no re-sealing of the formed pores could be detected in many cases, suggesting that the process induced cell death. Furthermore, electrodes yielding high-amplitude signals prior to electroporation often showed only an insignificant increase or even decrease in signal amplitude after the induction of pores in the membrane, suggesting that the sealing between cell and electrode greatly influences the electroporation efficiency as well harmfulness of the process.

Finally, various proof-of-principle investigations into modifications of the 3D structures were reported, aiming at an increase in surface area and thus reduction of device impedance. Initially, surfactants were added to the commercial Pur-A-Gold 202B gold bath, aiming to introduce porosity via the formation of micelles and resulting excluded volume during the electrodeposition. The poor solubility of various employed surfactants resulted in the development of two gold-bath compositions not containing the Pur-A-Gold 202B supplement. However, while a variety of different surface morphologies were observed, no porosity could be achieved, neither with Triton™ X-100 nor Tween® 20. In contrast, addition of Triton™ X-100 to a solution containing hexachloroplatinic acid resulted in a significant increase in roughness as compared to structures deposited from the unmodified platinum bath. As an alternative to the modification of the metal surface, the deposition of the conductive polymer PEDOT:PSS was investigated and found to result in a marked reduction in device impedance. Embryonic rat cortical neurons showed good adhesion and neurite outgrowth on the polymer-functionalized surfaces, proving the applicability of this approach.

While significant progress could be reported, various challenges remain to be solved in order to achieve a reliable system. Differences in the characteristics of the received substrates resulted in discrepancies in the stability of the produced PMMA templates as well as the viability of cultured neurons. So far, the exact cause of poor cell viability on some of the sample batches could neither be determined nor circumvented, despite extensive studies into possible reasons and different potential coatings. Therefore, the gold evaporation process needs to be scrutinized since reproducible substrates are a prerequisite for a successful application of this system. The same point holds true for the stability of the employed passivation. Due to the early failure of the insulating layer, both the signal recorded during electrophysiological studies as well as the re-usability of the devices suffer significantly. The problem of poor coverage of edges, which often results in pinholes along the rim of the feedline, was circumvented via RIE etching prior to gold evaporation, yielding feedlines that are level with the surrounding silicon oxide. However, the instability observed here was not merely an edge effect, but rather the result of pronounced delamination. Therefore, solving the technological challenge of the preparation of stable passivation layers will have to be a central part of future studies. A possible solution could be the deposition of insulators via atomic layer deposition and thus more even coverage of the device, which also enables the fabrication of thinner passivation layers and thus lower influence on the engulfment of 3D structures. However, whether this approach solves the problem of poor adhesion is questionable. Alternatively, polymeric passivation layers can be employed, but their increased thickness as compared to the employed silicon oxide/nitride stack introduces a different set of problems. Since the layer thickness of the insulator considerably exceeds the height of the 3D structure, engulfment-like processes are expected to be hampered. Overall, the development of a fabrication approach for free-standing 3D structures would pose a significant advantage over the method reported here since it would solve three inherent problems: First, the preparation of free-standing structures that protrude from the passivation with their full height would remove the necessity of cellular protrusion into the electrode aperture prior to the engulfment of the 3D structure. This could result in an improved cell-chip contact and thus coupling. Second, this approach would prevent the problem of misalignments between the 3D structure and the aperture and thus off-center position of the 3D design, which also influences the engulfment. Finally, it would eliminate the contribution of the low sealing on the surrounding planar electrode on the total R_{seal} of the sensing area and can thus be expected to result in higher signal amplitudes. The fabrication of free-standing 3D

structures could for example be achieved by omission of an aperture and selective removal of the passivation beneath the electron-beam-defined opening prior to the electrodeposition of the 3D structure. An alternative approach is the preparation of the 3D designs prior to the deposition of the passivation, followed by selective removal of the passivation on top of the 3D design. Both approaches have advantages and limitations. The feasibility of the etching process through the electron-beam defined template is highly dependent on the relative stabilities of the employed PMMA resist and underlying passivation with respect to the etchant and can result in a reduced final structure height due to a reduction in PMMA height. Additionally, it can induce poor structural preservation, particularly for hollow templates, where the stability of the PMMA plug masking the center of the structure determines whether the fabrication of hollow structures is possible. In contrast, the structure fabrication is not affected by the approach of a selective retrospective removal of the insulator from the 3D structures on fully passivated MEAs. In this case, however, the removal depends on a photolithography step and is thus subject to misalignment problems. Furthermore, it cannot be guaranteed that the passivation is solely removed from the 3D structure. It can rather be expected that there is also removal of the insulator on the planar area around the stalk of the structure, thus again forming a surrounding planar electrode. Ultimately, employing the PMMA template as etch mask seems to be the more promising approach, despite the expected challenges during the establishment of suitable parameters.

The general process for the fabrication of hollow and solid pillars and mushrooms of 800 nm in diameter has been copiously studied and shown to facilitate real-time control over the structure size. An advantageous modification of the developed methodology would be the adjustment of the deposition setup to include the ability to control the temperature of the goldbath. In this way, variations due to differences in the ambient temperature would be reduced. More data is needed to enable a reliable correlation for the development of the diameter of both solid 300 and 600 nm structures with the corrected deposition time (t_{total} - $t_{boundary}$). After an adjustment of the electron-beam lithography parameters solving the problem of insufficient exposure, the production of 2 µm and 3 µm designs on MEAs should be feasible. Additionally, the modifications of the 3D structures reported in Chapter 5 have to be transferred to MEAs. Electrochemical impedance spectroscopy of the various surface morphologies should be performed to enable a comparison of the increase in surface area and resulting decrease in impedance yielded by the different approaches. Furthermore, the stability of the resulting structures needs to be investigated. Afterwards, the various

structure types, sizes, and surface morphologies can again be employed for electrophysiological studies. However, since cell adhesion on the developed MEAs was found to be poor in many cases, the surface characteristics of the devices need to be carefully controlled. The potential problem of residual PMMA needs to be addressed, with a more in-depth study of the PMMA removal after electrodeposition required to enable the development of a stable system. The application of AR 600-71 during the cleaning cascade is a possible solution to this problem. Once good cell adhesion can be achieved with high fidelity, further studies into the effect of the different 3D structures on electrophysiological recordings can be performed, with particular focus on the investigation of neuronal networks.

Only limited focus was allocated to electroporation experiments in this body of work. In future studies, an in-depth correlation between the electrical characteristics of the device, the cell device coupling, and the necessary stimulation amplitude are needed in order to develop a reproducible electroporation approach. Without knowledge about both the impedance of the electrode and the coupling efficiency between biology and electronics, the electric field experienced by the cell will differ significantly between one electrode and the next when applying a common electroporation pulse. Therefore, the investigation of the influence of the applied electric field and harmfulness of the process is not possible since various fundamental parameters are unknown. Investigations into the cell viability after application of electroporation pulses should be conducted, in conjunction with fluorescent labeling of electroporated cells with membrane-impermeable dyes. In this manner, the efficiency of the process and the effect on cell viability could be studied.

The question remains why the experimentally observed interaction of both HL-1 cells and rat cortical neurons deviates from the reports in the literature, with only limited protrusion into the opening of hollow structures. Due to these discrepancies, the development of a mathematical model and subsequent simulation of the system could help to shed light on this observation. Furthermore, the functionalization of the resulting 3D electrodes with fusogenic liposomes as employed by Csiszár *et al.* [138] and resulting improvement to the cell-electrode contact should be investigated. Finally, the introduction of membrane insertion rings on 3D mushrooms as employed on pillars by the Melosh group could be a valuable approach to enable high sealing resistances. Attempts at depositing alternating layers of gold and platinum via electrodeposition were not successful, both due to a poor adhesion between the different layers as well as the high potential needed for gold deposition and concomitant reduction of hydrogen on platinum impeding a stable galvanization.

Solving this problem could enable a tight and highly stable cell-device interface for long-term electrophysiological recordings.

Appendix

List of abbreviations

AC	Alternating current
ADC	Analog-to-digital converter
ALD	Atomic layer deposition
AP	Action potential
APTES	(3-aminopropyl)triethoxysilane
ATP	Adenosine triphosphate
A^{z-}	Anion
BEL	Department of Bioelectronics at MINES Saint-Étienne
CAM	Cell adhesion molecule
cmc	Critical micelle concentration
CMOS	Complementary metal oxide semiconductor
CPD	Critical point drying
CVD	Chemical vapor deposition
DIV	Days *in vitro*
DMP-30	2,4,6-tris(dimethylaminomethyl)phenol
EBID	Electron beam-induced deposition
EDX	Energy-dispersive X-ray
EDOT	3,4-ethylenedioxythiophene
EEG	Electroencephalography
EIS	Electrochemical impedance spectroscopy
EtOH	Ethanol
FBS	Fetal bovine serum
FET	Field-effect transistor
FIB	Focused ion-beam
FibGel	5 µg/ml fibronectin in a 0.02% solution of gelatin in water
GHK	Goldman-Hodgkin-Katz
HBSS	Hank's balanced salt solution
HEK 293	Human embryonic kidney cells 293
HEPES	N-2-hydroxyethyl piperazine-N'-2-ethane sulphonic acid
IBID	Ion-beam-induced deposition
IHP	Inner Helmholtz plane
IQR	Interquartile range
IrOx	Iridium oxide
M	Metal
MA	Metal salt
MEA	Microelectrode array
M^{z+}	Metal ion
MRI	Magnetic resonance imaging
MUD	11-mercapto-1-undecanol
OHP	Outer Helmholtz plane

PBS	Phosphate buffered saline
PDMS	Polydimethylsiloxane
PECVD	Plasma-enhanced chemical vapor deposition
PEDOT:PSS	Poly(3,4-ethylenedioxythiophene):poly(4-styrenesulfonate)
PET	Positron emission tomography
PLL	Poly-L-lysine hydrobromide
PMMA	Poly(methyl methacrylate)
PSSNa	Poly(sodium 4-styrenesulfonate)
PVD	Physical vapor deposition
p2p	Peak-to-peak
QCM-D	Quartz crystal microbalance with dissipation monitoring
rcf	Relative centrifugal force
RIE	Reactive ion etching
S	Substrate
SAM	Self-assembled monolayer
SDS	Sodium dodecyl sulfate
SEM	Scanning electron microscopy
SHE	Standard hydrogen electrode
SIMS	Secondary ion mass spectrometry
S/N	Signal-to-noise
Triton™ X-100	Polyethylene glycol p-(1,1,3,3-tetramethylbutyl)-phenyl ether
Tween® 20	Polyoxyethylene (20) sorbitan monolaurate
UPW	Ultrapure water
vol%	Volume percent
wt%	Weight percent

Variables and constants

α	Transfer coefficient
β	Stability constant
ΔD	Change in dissipation
ΔE	Potential difference
Δf	Change in resonance frequency
ΔG	Gibb's energy
Δm	Change in mass
ε	Dielectric constant of the electrolyte
ε_0	Dielectric constant of the vacuum
η	Overpotential
γ_m	Activity coefficient
κ	Bending rigidity
λ_D	Debye length
Ψ	Binding energy
$\phi(N)$	Surface energy term
Φ_S	Potential of the bulk solution
Φ_M	Potential at the metal surface

ρ	Resistivity
ω	Angular frequency
a	Activity
A	Area
c	Concentration
C	Capacitance
C_c	Coupling coefficient
C_{QCM-D}	Characteristic parameter of the QCM-D
d	Distance
e	Elementary charge, $e = 1.602 \cdot 10^{-19} C$
e	Euler's number
e^-	Electron
E_0	Standard potential
$E_{adhesion}$	Adhesion energy
$E_{bending}$	Deformation energy cost
E_m	Membrane potential
F	Faraday's constant, $F = 96485.33\ C\ mol^{-1}$
H	Mean curvature
i	Imaginary unit
i	Current
j	Current density
j_0	Exchange current density
k_B	Boltzmann constant, $k_B = 1.381 \cdot 10^{-23} JK^{-1}$
n	Number of samples
n_h	Harmonic number
N	Number of atoms
N_c	Critical cluster size
P_X	Permeability of ion X
Q1	First quartile
Q3	Third quartile
R	Universal gas constant, $R = 8.314\ J\ mol^{-1}\ K^{-1}$
R_{seal}	Sealing resistance
$S_{membrane}$	Membrane area
S_{ad}	Contact area
T	Temperature
$t_{boundary}$	Time at which the deposition proceeds past the boundary of the PMMA template
t_{total}	Total time of the deposition
v	Reaction rate
V_{in}	Potential at amplifier input
V_j	Potential at cell-electrode junction
V_M	Membrane potential
V_{out}	Potential at amplifier output
w	Adhesion strength
z	Valency of the ion
Z	Impedance

References

[1] F. A. C. Azevedo, L. R. B. Carvalho, *et al.* "Equal numbers of neuronal and nonneuronal cells make the human brain an isometrically scaled-up primate brain," *Journal of Comparative Neurology*, 513(5), 2009.

[2] D. A. Drachman. "Do we have brain to spare?," *Neurology*, 64(2), 2005.

[3] E. Neher, and B. Sakmann. "Single-channel currents recorded from membrane of denervated frog muscle fibres," *Nature*, 260, 1976.

[4] C. A. Thomas, P. A. Springer, *et al.* "A miniature microelectrode array to monitor the bioelectric activity of cultured cells," *Experimental Cell Research*, 74(1), 1972.

[5] M. E. Spira, and A. Hai. "Multi-electrode array technologies for neuroscience and cardiology," *Nature Nanotechnology*, 8(2), 2013.

[6] M. R. Angle, B. Cui, *et al.* "Nanotechnology and neurophysiology," *Current Opinion in Neurobiology*, 32, 2015.

[7] B. Tian, and C. M. Lieber. "Synthetic nanoelectronic probes for biological cells and tissues," *Annual review of analytical chemistry*, 6, 2013.

[8] B. Tian, T. Cohen-Karni, *et al.* "Three-dimensional, flexible nanoscale field-effect transistors as localized bioprobes," *Science*, 329, 2010.

[9] D. A. Israel, W. H. Barry, *et al.* "An array of microelectrodes to stimulate and record from cardiac cells in culture," *The American Journal of Physiology*, 247(4), 1984.

[10] P. Connolly, P. Clark, *et al.* "An extracellular microelectrode array for monitoring electrogenic cells in culture," *Biosensors & Bioelectronics*, 5(3), 1990.

[11] W. G. Regehr, J. Pine, *et al.* "A long-term in vitro silicon-based microelectrode-neuron connection," *IEEE Transactions on Biomedical Engineering*, 35(12), 1988.

[12] L. J. Breckenridge, R. J. A. Wilson, *et al.* "Advantages of using microfabricated extracellular electrodes for in vitro neuronal recording," *Journal of Neuroscience Research*, 42(2), 1995.

[13] J. Pine. "Recording action potentials from cultured neurons with extracellular microcircuit electrodes," *Journal of Neuroscience Methods*, 2(1), 1980.

[14] G. W. Gross, A. N. Williams, *et al.* "Recording of spontaneous activity with photoetched microelectrode surfaces from mouse spinal neurons in culture," *Journal of Neuroscience Methods*, 5(1-2), 1982.

[15] J. R. Naughton, T. Connolly, *et al.* "Shielded coaxial optrode arrays for neurophysiology," *Frontiers in Neuroscience*, 10, 2016.

[16] F. Heer, S. Hafizovic, *et al.* "CMOS microelectrode array for bidirectional interaction with neuronal networks," *IEEE Journal of Solid-State Circuits*, 41(7), 2006.

[17] D. J. Bakkum, U. Frey, *et al.* "Tracking axonal action potential propagation on a high-density microelectrode array across hundreds of sites," *Nature Communications*, 4, 2013.

[18] M. Heim, B. Yvert, *et al.* "Nanostructuration strategies to enhance microelectrode array (MEA) performance for neuronal recording and stimulation," *Journal of Physiology Paris*, 106(3-4), 2012.

[19] R. Kim, S. Joo, *et al.* "Recent trends in microelectrode array technology for in vitro neural interface platform," *Biomedical Engineering Letters*, 4(2), 2014.

[20] E. Seker, Y. Berdichevsky, *et al.* "The fabrication of low-impedance nanoporous gold multiple-electrode arrays for neural electrophysiology studies," *Nanotechnology*, 21(12), 2010.

[21] D. Brüggemann, B. Wolfrum, *et al.* "Nanostructured gold microelectrodes for extracellular recording from electrogenic cells," *Nanotechnology*, 22(26), 2011.

[22] M. Heim, L. Rousseau, *et al.* "Combined macro-/mesoporous microelectrode arrays for low-noise extracellular recording of neural networks," *Journal of Neurophysiology*, 108(6), 2012.

[23] M. Wesche, M. Hüske, *et al.* "A nanoporous alumina microelectrode array for functional cell-chip coupling," *Nanotechnology*, 23(49), 2012.

[24] R. Kim, and Y. Nam. "Novel platinum black electroplating technique improving mechanical stability," *Proceedings of the Annual International Conference of the IEEE Engineering in Medicine and Biology Society, EMBS*, 2013.

[25] C. A. R. Chapman, H. Chen, *et al.* "Nanoporous gold as a neural interface coating: Effects of topography, surface chemistry, and feature size," *ACS Applied Materials & Interfaces*, 7(13), 2015.

[26] R. Kim, and Y. Nam. "Electrochemical layer-by-layer approach to fabricate mechanically stable platinum black microelectrodes using a mussel-inspired polydopamine adhesive," *Journal of Neural Engineering*, 12(2), 2015.

[27] Y. H. Kim, G. H. Kim, *et al.* "In vitro extracellular recording and stimulation performance of nanoporous gold-modified multi-electrode arrays," *Journal of Neural Engineering*, 12(6), 2015.

[28] Y. H. Kim, A. Y. Kim, *et al.* "Electrochemical and in vitro neuronal recording characteristics of multi-electrode arrays surface-modified with electro-co-deposited gold-platinum nanoparticles," *Biomedical Microdevices*, 18(1), 2016.

[29] L. Bareket-Keren, and Y. Hanein. "Carbon nanotube-based multi electrode arrays for neuronal interfacing: progress and prospects," *Frontiers in Neural Circuits*, 6, 2013.

[30] R. Sorkin, A. Greenbaum, *et al.* "Process entanglement as a neuronal anchorage mechanism to rough surfaces," *Nanotechnology*, 20(1), 2009.

[31] M. Shein, A. Greenbaum, *et al.* "Engineered neuronal circuits shaped and interfaced with carbon nanotube microelectrode arrays," *Biomedical Microdevices*, 11(2), 2009.

[32] M. David-Pur, L. Bareket-Keren, *et al.* "All-carbon-nanotube flexible multi-electrode array for neuronal recording and stimulation," *Biomedical Microdevices*, 16(1), 2014.

[33] X. Cui, and D. C. Martin. "Electrochemical deposition and characterization of poly(3,4-ethylenedioxythiophene) on neural microelectrode arrays," *Sensors and Actuators, B: Chemical*, 89, 2003.

[34] M. R. Abidian, J. M. Corey, *et al.* "Conducting-polymer nanotubes improve electrical properties, mechanical adhesion, neural attachment and neurite outgrowth of neural electrodes," *Small*, 6(3), 2010.

[35] M. Asplund, T. Nyberg, *et al.* "Electroactive polymers for neural interfaces," *Polymer Chemistry*, 1(9), 2010.

[36] N. Sanetra, V. Feig, *et al.* "Low impedance surface coatings via nanopillars and conductive polymers," *Physica Status Solidi (A)*, 208(6), 2011.

[37] H. Sorribas, D. Braun, *et al.* "Adhesion proteins for a tight neuron-electrode contact," *Journal of Neuroscience Methods*, 104(2), 2001.

[38] G. Wrobel, M. Holler, *et al.* "Transmission electron microscopy study of the cell-sensor interface," *Journal of the Royal Society Interface*, 5(19), 2008.

[39] M. Jenkner, and P. Fromherz. "Bistability of membrane conductance in cell adhesion observed in a neuron transistor," *Physical Review Letters*, 79(23), 1997.

[40] A. Cohen, J. Shappir, *et al.* "Reversible transition of extracellular field potential recordings to intracellular recordings of action potentials generated by neurons grown on transistors," *Biosensors and Bioelectronics*, 23(6), 2008.

[41] P. Wijdenes, H. Ali, *et al.* "A novel bio-mimicking, planar nano-edge microelectrode enables enhanced long-term neural recording," *Scientific Reports*, 6, 2016.

[42] B. Hofmann, E. Kätelhön, *et al.* "Nanocavity electrode array for recording from electrogenic cells," *Lab on a Chip*, 11(6), 2011.

[43] M. Schottdorf, B. Hofmann, *et al.* "Frequency-dependent signal transfer at the interface between electrogenic cells and nanocavity electrodes," *Physical Review E*, 85(3), 2012.

[44] A. Czeschik, A. Offenhäusser, *et al.* "Fabrication of MEA-based nanocavity sensor arrays for extracellular recording of action potentials," *Physica Status Solidi (A)*, 211(6), 2014.

[45] A. Czeschik, P. Rinklin, *et al.* "Nanostructured cavity devices for extracellular stimulation of HL-1 cells," *Nanoscale*, 7(20), 2015.

[46] M. E. Spira, D. Kamber, *et al.* "Improved neuronal adhesion to the surface of electronic device by engulfment of protruding micro-nails fabricated on the chip surface," *TRANSDUCERS 2007 - 2007 International Solid-State Sensors, Actuators and Microsystems Conference*, 2007.

[47] A. Hai, A. Dormann, *et al.* "Spine-shaped gold protrusions improve the adherence and electrical coupling of neurons with the surface of micro-electronic devices," *Journal of the Royal Society*, 6(41), 2009.

[48] A. Hai, J. Shappir, *et al.* "In-cell recordings by extracellular microelectrodes," *Nature Methods*, 7(3), 2010.

[49] F. Santoro, S. Dasgupta, *et al.* "Interfacing electrogenic cells with 3D nanoelectrodes: Position, shape, and size matter," *ACS Nano*, 8(7), 2014.

[50] Z. C. Lin, C. Xie, *et al.* "Iridium oxide nanotube electrodes for sensitive and prolonged intracellular measurement of action potentials," *Nature Communications*, 5, 2014.

[51] J. J. VanDersarl, A. M. Xu, *et al.* "Nanostraws for direct fluidic intracellular access," *Nano Letters*, 12(8), 2012.

[52] X. Xie, A. M. Xu, *et al.* "Mechanical model of vertical nanowire cell penetration," *Nano Letters*, 13(12), 2013.

[53] J. T. Robinson, M. Jorgolli, *et al.* "Vertical nanowire electrode arrays as a scalable platform for intracellular interfacing to neuronal circuits," *Nature Nanotechnology*, 7(3), 2012.

[54] N. Shmoel, N. Rabieh, *et al.* "Multisite electrophysiological recordings by self-assembled loose-patch-like junctions between cultured hippocampal neurons and mushroom-shaped microelectrodes," *Scientific Reports*, 6, 2016.

[55] A. Hai, J. Shappir, *et al.* "Long-term, multisite, parallel, in-cell recording and stimulation by an array of extracellular microelectrodes," *Journal of Neurophysiology*, 104(1), 2010.

[56] S. M. Ojovan, N. Rabieh, *et al.* "A feasibility study of multi-site, intracellular recordings from mammalian neurons by extracellular gold mushroom-shaped microelectrodes," *Scientific Reports*, 5, 2015.

[57] A. Aalipour, A. M. Xu, *et al.* "Plasma membrane and actin cytoskeleton as synergistic barriers to nanowire cell penetration," *Langmuir*, 30(41), 2014.

[58] R. Liu, R. Chen, *et al.* "High density individually addressable nanowire arrays record intracellular activity from primary rodent and human stem cell derived neurons," *Nano Letters*, 17(5), 2017.

[59] J. J. VanDersarl, and P. Renaud. "Biomimetic surface patterning for long-term transmembrane access," *Scientific Reports*, 6, 2016.

[60] I. Y. Wong, B. D. Almquist, *et al.* "Dynamic actuation using nano-bio interfaces," *Materials Today*, 13(6), 2010.

[61] B. D. Almquist, and N. A. Melosh. "Fusion of biomimetic stealth probes into lipid bilayer cores," *Proceedings of the National Academy of Sciences of the United States of America*, 107(13), 2010.

[62] P. Verma, and N. A. Melosh. "Gigaohm resistance membrane seals with stealth probe electrodes," *Applied Physics Letters*, 97(3), 2010.

[63] M. Paunovic, and M. Schlesinger, *Fundamentals of electrochemical deposition*. WILEY-VCH Verlag, 2006.

[64] F. Scholz, *Electroanalytical Methods - guide to experiments and applications*. Springer, 2002.

[65] C. H. Hamann, A. Hamnett, *et al.*, *Electrochemistry*. WILEY-VCH Verlag, 1998.

[66] L. Almonte, E. Lopez-Elvira, *et al.* "Surface-charge differentiation of streptavidin and avidin by atomic force microscopy-force spectroscopy," *ChemPhysChem*, 15(13), 2014.

[67] C. E. Mortimer, and U. Müller, *Das Basiswissen der Chemie*. Georg Thieme Verlag, 8th Edition, 2003.

[68] A. Vicenzo, and P. L. Cavallotti, "Gold Electroplating," in *Gold Science and Application* (A. Vicenzo, and P. L. Cavallotti, Editors), ch. 11, CRC Press, 2010.

[69] P. A. Kohl, "Electrodeposition of Gold," in *Modern Electroplating* (M. Schlesinger, and M. Paunovic, Editors), ch. 4, pp. 115–130, John Wiley & Sons, Inc., 5th Edition, 2010.

[70] A. J. Bard, and L. R. Faulkner, *Electrochemical Methods, Fundamentals and Applications*. John Wiley & Sons, Inc., 2nd Edition, 2001.

[71] P. W. Atkins, and J. de Paula, *Physikalische Chemie*. WILEY-VCH Verlag, 4th Edition, 2006.

[72] P. Wilkinson. "Understanding gold plating," *Gold Bulletin*, 19(3), 1986.

[73] E. Budevski, G. Staikov, *et al.* "Electrocrystallization nucleation and growth phenomena," *Electrochimica Acta*, 45(15-16), 2000.

[74] E. B. Budevski, G. T. Staikov, *et al.*, *Electrochemical phase formation and growth: An introduction to the initial stages of metal deposition*. VCH Verlagsgemeinschaft mbH, 1996.

[75] Y. D. Gamburg, and G. Zangari, *Theory and practice of metal electrodeposition*. Springer, 2011.

[76] T. A. Green. "Gold electrodeposition for microelectronic, optoelectronic and microsystem applications," *Gold Bulletin*, 40(2), 2007.

[77] B. Bozzini, C. Mele, *et al.* "Time-dependent in situ SERS study of CN− adsorbed on gold," *Journal of Electroanalytical Chemistry*, 592(1), 2006.

[78] X. Cui, and D. C. Martin. "Fuzzy gold electrodes for lowering impedance and improving adhesion with electrodeposited conducting polymer films," *Sensors and Actuators A: Physical*, 103(3), 2003.

[79] H. Willing, and R. Freudenberger. "Galvanische Abscheidung von Gold - Eine Übersicht (Teil 6)," *Galvanotechnik*, 11, 2012.

[80] A. L. Hodgkin, and A. F. Huxley. "A quantitative description of membrane current and its application to conduction and excitation in nerve," *Bulletin of Mathematical Biology*, 117(1-2), 1952.

[81] E. R. Kandel, J. H. Schwartz, *et al.*, *Principles of neural science*. McGraw-Hill New York, 4th Edition, 2000.

[82] J. V. Raimondo, R. J. Burman, *et al.* "Ion dynamics during seizures," *Frontiers in Cellular Neuroscience*, 9, 2015.

[83] D. C. Sterratt, *Goldman-Hodgkin-Katz Equations*, pp. 1–3. New York, NY: Springer New York, 2013.

[84] B. P. Bean. "The action potential in mammalian central neurons," *Nature Reviews Neuroscience*, 8(6), 2007.

[85] M. Baruscotti, A. Bucchi, *et al.* "Physiology and pharmacology of the cardiac pacemaker ('funny') current," *Pharmacology & Therapeutics*, 107, 2005.

[86] H. T. Shih. "Anatomy of the action potential in the heart," *Texas Heart Institute Journal*, 21, 1994.

[87] S. Nattel, and L. Carlsson. "Innovative approaches to anti-arrhythmic drug therapy," *Nature Reviews. Drug Discovery*, 5(12), 2006.

[88] O. P. Hamill, A. Marty, *et al.* "Improved patch-clamp techniques for high-resolution current recording from cells and cell-free membrane patches," *European Journal of Physiology*, 391, 1981.

[89] N. Rabieh, S. M. Ojovan, *et al.* "On-chip, multisite extracellular and intracellular recordings from primary cultured skeletal myotubes," *Scientific Reports*, 6, 2016.

[90] A. Fendyur, N. Mazurski, *et al.* "Formation of essential ultrastructural interface between cultured hippocampal cells and gold mushroom-shaped MEA - Toward IN-CELL recordings from vertebrate neurons," *Frontiers in Neuroengineering*, 4, 2011.

[91] P. Fromherz, A. Offenhäusser, *et al.* "A neuron-silicon junction: a Retzius cell of the leech on an insulated-gate field-effect transistor," *Science*, 252(5010), 1991.

[92] S. Park, Y. J. Song, *et al.* "Nanoporous Pt microelectrode for neural stimulation and recording: In vitro characterization," *The Journal of Physical Chemistry C*, 114(19), 2010.

[93] M. E. J. Obien, K. Deligkaris, *et al.* "Revealing neuronal function through microelectrode array recordings," *Frontiers in Neuroscience*, 8, 2015.

[94] K. Toma, H. Kano, *et al.* "Label-free measurement of cell-electrode cleft gap distance with high spatial resolution surface plasmon microscopy," *ACS Nano*, 8(12), 2014.

[95] P. Fromherz, "Neuroelectronic interfacing: semiconductor chips with ion channels, nerve cells, and brain," in *Nanoelectronics and Information Technology* (R. Waser, Editor), pp. 781–810, WILEY-VCH Verlag, 2003.

[96] N. Joye, A. Schmid, *et al.* "An electrical model of the cell-electrode interface for high-density microelectrode arrays," *30th Annual International Conference of the IEEE Engineering in Medicine and Biology Society Conference*, 2008.

[97] N. Joye, A. Schmid, *et al.* "Electrical modeling of the cell-electrode interface for recording neural activity from high-density microelectrode arrays," *Neurocomputing*, 73(1-3), 2009.

[98] C. Xie, Z. Lin, *et al.* "Intracellular recording of action potentials by nanopillar electroporation," *Nature Nanotechnology*, 7(3), 2012.

[99] B. C. Wheeler, Y. Nam, *et al.* "In vitro microelectrode array technology and neural recordings," *Critical Reviews in Biomedical Engineering*, 39(1), 2011.

[100] L. Hanson, Z. C. Lin, *et al.* "Characterization of the cell-nanopillar interface by transmission electron microscopy," *Nano Letters*, 12(11), 2012.

[101] A. Hai, D. Kamber, *et al.* "Changing gears from chemical adhesion of cells to flat substrata toward engulfment of micro-protrusions by active mechanisms," *Journal of Neural Engineering*, 6(6), 2009.

[102] G. C. Brown, and J. J. Neher. "Microglial phagocytosis of live neurons," *Nature Reviews Neuroscience*, 15(4), 2014.

[103] S. Bowen, D. D. Ateh, *et al.* "The phagocytic capacity of neurones," *European Journal of Neuroscience*, 25(10), 2007.

[104] F. Santoro, J. Schnitker, *et al.* "On chip guidance and recording of cardiomyocytes with 3D mushroom-shaped electrodes," *Nano Letters*, 13(11), 2013.

[105] A. M. Xu, A. Aalipour, *et al.* "Quantification of nanowire penetration into living cells," *Nature Communications*, 5, 2014.

[106] M. Dipalo, G. C. Messina, *et al.* "Multifunctional biosensing with three-dimensional plasmonic nanoantennas," *Proc. SPIE 9518, Bio-MEMS and Medical Microdevices II*, 9518, 2015.

[107] G. Bugnicourt, J. Brocard, *et al.* "Nanoscale surface topography reshapes neuronal growth in culture," *Langmuir*, 30(15), 2014.

[108] H. Persson, C. Køhler, *et al.* "Fibroblasts cultured on nanowires exhibit low motility, impaired cell division, and DNA damage," *Small*, 9(23), 2013.

[109] A. Fendyur, and M. E. Spira. "Toward on-chip, in-cell recordings from cultured cardiomyocytes by arrays of gold mushroom-shaped microelectrodes," *Frontiers in Neuroengineering*, 5, 2012.

[110] J. Gehl. "Electroporation: Theory and methods, perspectives for drug delivery, gene therapy and research," *Acta Physiologica Scandinavica*, 177(4), 2003.

[111] K. Riaz, S.-F. Leung, *et al.* "Electric field enhanced 3D scalable low-voltage nano-spike electroporation system," *Sensors and Actuators A: Physical*, 255, 2017.

[112] A. Hai, and M. E. Spira. "On-chip electroporation, membrane repair dynamics and transient in-cell recordings by arrays of gold mushroom-shaped microelectrodes," *Lab on a Chip*, 12(16), 2012.

[113] B. D. Almquist, and N. A. Melosh. "Molecular structure influences the stability of membrane penetrating biointerfaces," *Nano Letters*, 11(5), 2011.

[114] F. De Angelis, M. Malerba, *et al.* "3D hollow nanostructures as building blocks for multifunctional plasmonics," *Nano Letters*, 13(8), 2013.

[115] M. Dipalo, G. C. Messina, *et al.* "3D plasmonic nanoantennas integrated with MEA biosensors," *Nanoscale*, 7(8), 2015.

[116] S. Weidlich, K. J. Krause, *et al.* "MEAs and 3D nanoelectrodes: electrodeposition as tool for a precisely controlled nanofabrication," *Nanotechnology*, 28(9), 2017.

[117] Forschungszentrum Jülich GmbH. "HNF - Helmholtz Nano Facility," *Journal of large-scale research facilities*, 3, 2017.

[118] F. Zhang, J. Liu, *et al.* "Reference and counter electrode positions affect electrochemical characterization of bioanodes in different bioelectrochemical systems," *Biotechnology and Bioengineering*, 111(10), 2014.

[119] G. Panaitov, S. Thiery, *et al.* "Fabrication of gold micro-spine structures for improvement of cell/device adhesion," *Microelectronic Engineering*, 88(8), 2011.

[120] Z. Jahed, P. Lin, *et al.* "Responses of Staphylococcus aureus bacterial cells to nanocrystalline nickel nanostructures," *Biomaterials*, 35(14), 2014.

[121] W. C. Claycomb, N. A. Lanson, *et al.* "HL-1 cells: a cardiac muscle cell line that contracts and retains phenotypic characteristics of the adult cardiomyocyte," *Proceedings of the National Academy of Sciences of the United States of America*, 95(6), 1998.

[122] J. A. Kiernan. "Formaldehyde, formalin, paraformaldehyde and glutaraldehyde: What they are and what they do," *Microscopy Today*, (1), 2000.

[123] J. J. Bozzola, and L. D. Russell, *Electron Microscopy Principles and Techniques for Biologists*. Jones and Bartlett Publishers, 1999.

[124] A. Belu, J. Schnitker, *et al.* "Ultra-thin resin embedding method for scanning electron microscopy of individual cells on high and low aspect ratio 3D nanostructures," *Journal of Microscopy*, 263(1), 2016.

[125] F. Di Scipio, S. Raimondo, *et al.* "A simple protocol for paraffin-embedded myelin sheath staining with osmium tetroxide for light microscope observation," *Microscopy Research and Technique*, 71(7), 2008.

[126] E. Spedden, J. D. White, *et al.* "Elasticity maps of living neurons measured by combined fluorescence and atomic force microscopy," *Biophysical Journal*, 103(5), 2012.

[127] F. Kossivas, M. Michaelides, *et al.* "Elasticity measurements from left bentricular murine HL-1 cardiomyocytes using atomic force microscopy," *The FASEB Journal*, 29(1 Supplement), 2015.

[128] S. Fedoroff, and A. Richardson, *Protocols for neuronal cell culture*. Humana Press, 3rd Edition, 2001.

[129] M. C. Dixon. "Quartz crystal microbalance with dissipation monitoring: Enabling real-time characterization of biological materials and their interactions," *Journal of Biomolecular Techniques*, 19(3), 2008.

[130] W. T. Shier, D. J. Dubourdieu, *et al.* "Polycations as prostaglandin synthesis inducers. Stimulation of arachidonic acid release and prostaglandin synthesis in cultured fibroblasts by poly(L-lysine) and other synthetic polycations," *Biochimica et Biophysica Acta*, 193(2), 1984.

[131] B. Kotecha, and G. P. Richardson. "Ototoxicity in vitro: effects of neomycin, gentamicin, dihydrostreptomycin, amikacin, spectinomycin, neamine, spermine and poly-L-lysine," *Hearing Research*, 73(2), 1994.

[132] P. Symonds, J. C. Murray, *et al.* "Low and high molecular weight poly(L-lysine)s/poly(L-lysine)-DNA complexes initiate mitochondrial-mediated apoptosis differently," *FEBS Letters*, 579(27), 2005.

[133] L. J. Arnold, A. Dagan, *et al.* "Antineoplastic activity of poly(L-lysine) with some ascites tumor cells," *Proceedings of the National Academy of Sciences of the United States of America*, 76(7), 1979.

[134] K. E. Michael, E. Bockelman, *et al.*, "A little positivity goes a long way: Optimal surface charge density supports neuronal adhesion and polarization," in *ENGINEERING CELL BIOLOGY III: Engineering conferences International, Santa Cruz, California, USA*, 2009.

[135] R. C. Schmidt, and K. E. Healy. "Effect of avidin-like proteins and biotin modification on mesenchymal stem cell adhesion," *Biomaterials*, 34(15), 2013.

[136] J.-F. Pan, N.-H. Liu, *et al.* "Application of avidin-biotin technology to improve cell adhesion on nanofibrous matrices," *Journal of Nanobiotechnology*, 13, 2015.

[137] S. F. Fenz, R. Merkel, *et al.* "Diffusion and intermembrane distance: Case study of avidin and E-cadherin mediated adhesion," *Langmuir*, 25(2), 2009.

[138] A. Csiszár, N. Hersch, *et al.* "Novel fusogenic liposomes for fluorescent cell labeling and membrane modification," *Bioconjugate Chemistry*, 21(3), 2010.

[139] T. Auth, "Particles at Interfaces and Membranes," in *46th IFF Spring School - Book of Manuscripts*, pp. D1.1–D1.28, 2015.

[140] S. Dasgupta, T. Auth, *et al.* "Shape and orientation matter for cellular uptake of non-spherical nanoparticles," *Nano Letters*, 14, 2014.

[141] A. Offenhäusser, J. Albers, *et al.*, "Micro- & Nanotechnologies for Neuroscience," in *46th IFF Spring School - Book of Manuscripts*, 2015.

[142] V. Maybeck, J. Schnitker, *et al.* "An evaluation of extracellular MEA versus optogenetic stimulation of cortical neurons," *Biomedical Physics & Engineering Express*, 2(5), 2016.

[143] F. Grinnell, and M. K. Feld. "Adsorption characteristics of plasma fibronectin in relationship to biological activity," *Journal of Biomedical Materials Research*, 15(3), 1981.

[144] G. Wrobel, Y. Zhang, *et al.* "Influence of the first amplifier stage in MEA systems on extracellular signal shapes," *Biosensors and Bioelectronics*, 22(6), 2007.

[145] C. Gold, D. A. Henze, *et al.* "On the origin of the extracellular action potential waveform: A modeling study," *Journal of Neurophysiology*, 95, 2006.

[146] Y. Y. Fang, X. Li, *et al.* "Organic bioelectronics for neural interfaces," *Journal of Materials Chemistry C*, 3(25), 2015.

[147] S. F. Lempka, M. D. Johnson, *et al.* "Optimization of microelectrode design for cortical recording based on thermal noise considerations," *Annual International Conference of the IEEE Engineering in Medicine and Biology - Proceedings*, 2006.

[148] G. E. Tiller, T. J. Mueller, *et al.* "Hydrogenation of Triton X-100 eliminates its fluorescence and ultraviolet light absorption while preserving its detergent properties," *Analytical Biochemistry*, 141(1), 1984.

[149] A. Patist, S. S. Bhagwat, *et al.* "On the measurement of critical micelle concentrations of pure and technical-grade nonionic surfactants," *Journal of Surfactants and Detergents*, 3(1), 2000.

[150] C. Carnero Ruiz, J. A. Molina-Bolívar, *et al.* "Thermodynamic and structural studies of Triton X-100 micelles in ethylene glycol-water mixed solvents," *Langmuir*, 17(22), 2001.

[151] C. Carnero Ruiz, J. Molina-Bolívar, *et al.* "Effect of ethylene glycol on the thermodynamic and micellar properties of Tween 20," *Colloid and Polymer Science*, 281(6), 2003.

[152] R. Robson, and E. Dennis. "The size, shape, and hydration of nonionic surfactant micelles. Triton X-100," *The Journal of Physical Chemistry*, 81(11), 1977.

[153] A. B. Mandal, S. Ray, *et al.* "Physicochemical studies on the characterization of Triton X 100 micelles in an aqueous environment and in the presence of additives," *The Journal of Physical Chemistry*, 84(8), 1980.

[154] H. H. Paradies. "Shape and size of a nonionic surfactant micelle. Triton X-100 in aqueous solution," *Journal of Physical Chemistry*, 84, 1980.

[155] S. Devaraj, and N. Munichandraiah. "The effect of nonionic surfactant Triton X-100 during electrochemical deposition of MnO2 on its capacitance properties," *Journal of The Electrochemical Society*, 154(10), 2007.

[156] A. Gomes, and M. I. da Silva Pereira. "Zn electrodeposition in the presence of surfactants. Part I. Voltammetric and structural studies," *Electrochimica Acta*, 52(3), 2006.

[157] K. Chen, and G. D. Wilcox. "Tin–manganese alloy electrodeposits," *Journal of the Electrochemical Society*, 155(2), 2008.

[158] L. Feng, A. Sivanesan, *et al.* "Electrochemical current rectification-a novel signal amplification strategy for highly sensitive and selective aptamer-based biosensor," *Biosensors and Bioelectronics*, 66, 2015.

[159] L. Feng, Z. Lyu, *et al.* "Electrochemically triggered aptamer immobilization via click reaction for vascular endothelial growth factor detection," *Engineering in Life Sciences*, 16(6), 2016.

[160] A. M. Feltham, and M. Spiro. "Platinized platinum electrodes," *Chemical Reviews*, 71(2), 1971.

[161] R. N. Goldberg, and L. G. Hepler. "Thermochemistry and oxidation potentials of the platinum group metals and their compounds," *Chemical Reviews*, 68(2), 1968.

[162] M. S. Manhas, P. Kumar, *et al.* "Oxidative degradation of non-ionic surfactant (TritonX-100) by chromium(VI)," *Colloids and Surfaces A: Physicochemical and Engineering Aspects*, 320(1-3), 2008.

[163] P. Shukla, and S. K. Upadhyay. "Kinetics of oxidation of non-ionic surfactants (Triton X-100 and Brij-35) by KMnO4 in H2SO4 medium," *Indian Journal of Chemistry*, 47, 2008.

[164] J. Rivnay, S. Inal, *et al.* "Structural control of mixed ionic and electronic transport in conducting polymers," *Nature Communications*, 7, 2016.

[165] B. Lu, L. Qin, *et al.* "Electropolymerization of 3,4-ethylenedithiathiophene in the green binary solvent system of water and ethanol," *International Journal of Electrochemical Science*, 9, 2014.

[166] N. H. Nabilah Azman, H. N. Lim, *et al.* "Effect of electropolymerization potential on the preparation of PEDOT/graphene oxide hybrid material for supercapacitor application," *Electrochimica Acta*, 188, 2016.

[167] J. A. Bearden. "X-ray wavelengths," *Reviews of Modern Physics*, 39(1), 1967.

Band / Volume 143
Etablierung eines Systems aus Cysteinmutanten der Phosphoglycerat-Kinase für Entfaltungsstudien mit Einzelmolekül-FRET
A. Schöne (2017), 137 pp
ISBN: 978-3-95806-237-5

Band / Volume 144
Structural and electronic characterization of hetero-organic NTCDA-CuPc adsorbate systems on Ag(111)
S. Schröder (2017), vi, 154 pp
ISBN: 978-3-95806-239-9

Band / Volume 145
Tailoring Molecular Magnetism
T. Esat (2017), viii, 163 pp
ISBN: 978-3-95806-240-5

Band / Volume 146
Spin-wave excitations and electron-magnon scattering in elementary ferromagnets from *ab initio* many-body perturbation theory
M. C. T. D. Müller (2017), vi, 174 pp
ISBN: 978-3-95806-242-9

Band / Volume 147
Neutron Scattering
Lectures of the JCNS Laboratory Course held at Forschungszentrum Jülich and at the Heinz-Maier-Leibnitz Zentrum Garching
edited by T. Brückel, S. Förster, G. Roth, and R. Zorn (Eds.) (2017),
ca 400 pp
ISBN: 978-3-95806-243-6

Band / Volume 148
Neutron scattering
Experimental Manuals of the JCNS Laboratory Course held at Forschungszentrum Jülich and at the Heinz-Maier-Leibnitz Zentrum Garching
edited by T. Brückel, S. Förster, G. Roth, and R. Zorn (Eds.) (2017),
ca 200 pp
ISBN: 978-3-95806-244-3

Band / Volume 149
Kinetic and thermodynamic considerations on the formation of heteromolecular layers on metal surfaces
C. Henneke (2017), vii, 157, XIV pp
ISBN: 978-3-95806-245-0

Band / Volume 150
Spectroscopic characterization of local valence change processes in resistively switching complex oxides
C. Bäumer (2017), x, 206 pp
ISBN: 978-3-95806-246-7

Band / Volume 151
Magnetic structure in relation to the magnetic field induced ferroelectricity in Y-type hexaferrite $Ba_{2-x}Sr_xZn_2Fe_{12}O_{22}$
P. Thakuria (2017), 17, 180 pp
ISBN: 978-3-95806-250-4

Band / Volume 152
Statistical analysis tools for assessing the functional relevance of higher-order correlations in massively parallel spike trains
V. Rostami (2017), x, 176 pp
ISBN: 978-3-95806-251-1

Band / Volume 153
The influence of the substrate on the structure and electronic properties of carbon-based 2D materials
J. Sforzini (2017), XIII, 145 pp
ISBN: 978-3-95806-255-9

Band / Volume 154
Gate-All-Around Silicon Nanowire Tunnel FETs for Low Power Applications
G. V. Luong (2017), ii, 136 pp
ISBN: 978-3-95806-259-7

Band / Volume 155
Graphene Devices for Extracellular Measurements
D. Kireev (2017), ix, 169 pp
ISBN: 978-3-95806-265-8

Band / Volume 156
Nanoscale 3D structures towards improved cell-chip coupling on microelectrode arrays
S. D. Weidlich (2017), II, 154 pp
ISBN: 978-3-95806-278-8

Weitere ***Schriften des Verlags im Forschungszentrum Jülich*** unter
http://wwwzb1.fz-juelich.de/verlagextern1/index.asp

Schlüsseltechnologien /
Key Technologies
Band / Volume 156
ISBN 978-3-95806-278-8